

MICROSTRUCTURE MECHANICAL PROPERTIES AND WEAR BEHAVIOR OF
SINTERED Fe-Mo-Mn-Si-C SELF-LUBRICATING COMPOSITES



A THESIS REPORT SUBMITTED IN PARTIAL FULFILLMENT
OF THE REQUIREMENTS FOR THE DEGREE OF
MASTER OF ENGINEERING IN AUTOMOTIVE ENGINEERING
SCHOOL OF ENGINEERING
KING MONGKUT'S INSTITUTE OF TECHNOLOGY LADKRABANG
2021
KMITL-2021-EN-M-037-077

This material is reserved for educational use only, not allowed for commercial use.

Forbidden to modify the content, and cite the document when use.



COPYRIGHT 2021

SCHOOL OF ENGINEERING

KING MONGKUT'S INSTITUTE OF TECHNOLOGY LADKRABANG

This material is reserved for educational use only, not allowed for commercial use.

Forbidden to modify the content, and cite the document when use.

THESIS TITLE	Microstructure Mechanical properties and Wear behavior of Sintered Fe-Mo-Mn-Si-C Self-Lubricating Composites
STUDENT	Ms. Thunyamon Nithimetthakul
STUDENT ID	62601146
DEGREE	Master of Engineering
YEAR	2021
PROGRAM	Automotive Engineering (International Program)
ADVISOR	Assoc. Prof. Dr. Preechar Karin
CO-ADVISOR	Dr. Ruangdaj Tongsri
CO-ADVISOR	Prof. Dr. Naoto Ohtake

ABSTRACT

In recent year, powder metallurgy (PM) has been widely used for producing aerospace, marine and automotive composite parts due to versatile ability of PM process to combine various types of reinforcements and matrices. One promising sintered composite type is a self-lubricating material, with a high mechanical strength and wear properties of low friction coefficient and wear rate. A sintered self-lubricating composite has high potential for tribological applications because it has solid lubricant particles embedded in a matrix. In this work, self-lubricating composites, metal matrix composites embedded with in-situ generated solid lubricant particles, were prepared from different iron and iron alloy powders, such as Fe, Fe-0.50Mo-0.15Mn, Fe-0.85Mo-0.15Mn and Fe-1.50Mo-0.15Mn powder, mixed with fixed 4 wt. % silicon carbide powder. All experimental sintered composites were processed by using uniaxial die pressing and sintering method. It was revealed that the common microstructural feature of the sintered Fe-Si-C composite consisted of a black particle enveloped with ferrite and pearlite. For Mo-containing sintered composites, they showed different matrices. With 0.5 wt.% Mo, the sintered composite had the same microstructural feature as the sintered Fe-Si-C composite. With 0.85 and 1.50 wt.% Mo, the sintered composite matrices showed ausferrite (bainitic ferrite + austenite) coexisting with pearlite. The fraction of ausferrite increased with increasing

Mo content. The refinement of pearlite interlamellar spacing had strong influence on hardness of sintered composites. The increase fraction of pearlite + ausferrite led to the increase of tensile strength. It was revealed that friction coefficient and wear rate of sintered composites decreased with increasing fractions of black particles and increasing mechanical strength and hardness.

Keywords: sintering, Fe-Mo-Mn-Si-C, self-lubricating composite, mechanical properties, tribological properties



ACKNOWLEDGEMENT

The first I would like to express my very great appreciation to the scholarship from Thailand Advanced Institute of Science and Technology, and Tokyo Institute of Technology (TAIST-Tokyo Tech) which is a collaborative program between National Science and Technology Development Agency (NSTDA, Thailand) and Tokyo Institute of Technology (Tokyo-Tech, Japan).

I wish to acknowledge the help provided by my thesis advisor Dr. Ruangdaj Tongstri for his constructive and valuable suggestions during the planning and development of this research work. His willingness to give his time so generously has been very much appreciated, co-advisor Assoc. Prof. Dr. Preechar Karin of International College at King Mongkut's Institute of Technology Ladkrabang for his kind guidance and supervision through all obstacles and challenges during this work, and Prof. Dr. Naoto Ohtake of the Departments of Mechanical Engineering, Tokyo Institute of Technology, Japan for his useful recommendations on this work.

I would like to thank for financial supported by National Science and Technology Development Agency (NSTDA) under the 'Design and manufacturing of replacement parts for railway applications (P1951261)' project and materials supported, ATMET4001, 4401 and 4901 powders by P.S. Steel Co., Ltd., the metal powder distributor of Rio Tinto Metal Powders of Canada.

My special thanks are extended to the Powder Metallurgy Research staff and Powder Metallurgy Research and Development Unit of National Metal and Materials Technology Center (MTEC), Materials Technology Center (MTEC) for devices, guidance, and technical supports.

Finally, I wish to thank to all lecturers and all my colleagues for guidance support me. Moreover, my family who always be there to support, motivate and encouragement me throughout my study. Without supports and inspirations of many people, this thesis would not have been possible.

Thunyamon Nitimethakul

TABLE OF CONTENTS

CHAPTER	PAGE
ABSTRACT.....	I
ACKNOWLEDGEMENT	III
TABLE OF CONTENTS	IV
LIST OF TABLES	VIII
LIST OF FIGURES.....	IX
LIST OF SYMBOLS.....	XIII
LIST OF DEFINITIONS	XIV
CHAPTER 1 INTRODUCTION	1
1.1. Research Background.....	1
1.2. Objective.....	2
1.3. Scopes	3
1.4. Expected Benefits.....	3
CHAPTER 2 LITERATURE REVIEW.....	4
2.1. Powder metallurgy (PM).....	4
2.1.1. Powder characteristic	5
2.1.2. Powder mixing.....	6
2.1.3. Compaction	6
2.1.4. Sintering.....	7
2.1.5. Sintering atmosphere	8
2.2. Alloying Element.....	8
2.2.1. Effects of alloying element on transformation diagrams.....	9
2.2.2. Effect of alloying element on ferrite hardness.....	10
2.2.3. Effect of alloying element on the formation of alloy carbides (Secondary hardening).....	10
2.3. Self-lubricant material	11

2.3.1 Graphite	12
2.4. Microstructure.....	13
2.4.1. Ferrite microstructure.....	14
2.4.2. Pearlite microstructure.....	14
2.4.3. Martensite microstructure	16
2.4.4. Bainite microstructure	17
2.5. Porosity.....	18
2.6. Density.....	22
2.6.1. Effect of SiC on sintered density	23
2.7. Wear testing.....	24
2.7.1. The pin on disc wear tester.....	25
2.7.2. The friction coefficient.....	26
2.7.3. Wear rate.....	27
2.7.4. Mass loss	27
2.7.5. Volume loss.....	27
2.8. Wear mechanism	27
2.8.1. Adhesive wear	28
2.8.2. Abrasive wear	29
2.8.3. Fatigue/ Delamination wear.....	30
2.8.4. Corrosive/ Oxidative wear	32
CHAPTER 3 RESEARCH METHODOLOGY.....	34
3.1. Materials.....	34
3.1.1. Iron base particle powder	34
3.1.2. Pre-alloyed Fe-Mo-Mn powders	35
3.1.3. Silicon carbide.....	35
3.1.4. Zinc stearate.....	37
3.1.5. Argon gas	37
3.1.6. Nital etchant.....	38

3.2. Experimental Equipment	39
3.2.1. Digital balance.....	39
3.2.2. Analytical balance.....	39
3.2.3. Powder blender	40
3.2.4. Hydraulic pressing machine	40
3.2.5. High vacuum sintering furnace.....	41
3.2.6. High precision cutting machine.....	42
3.2.7. Hot mounting press	42
3.2.8. Metallurgical Grinding Polishing Machine	43
3.2.9. Silicon Carbide paper	43
3.2.10. Polishing cloth	44
3.2.11. Diamond suspension size 6, 3 and 1 μm	45
3.3. Characterization instruments	45
3.3.1. Digital vernier.....	45
3.3.2. Macro hardness testing machine.....	46
3.3.3. Universal testing machine (Instron 8801).....	47
3.3.4. Optical Microscope	47
3.3.5. Scanning Electron Microscope	48
3.3.6. X-Ray Diffraction Analysis	49
3.3.7. Pin-on-disc testing machine.....	50
3.4 Experimental procedure	50
3.4.1. Mixing powder.....	50
3.4.2. Compaction	51
3.4.3. Sintering	52
3.4.4. Mechanical test.....	53
3.4.5. Wear test	54
3.4.6. Microstructure Analysis	55
3.4.7. X-Ray Diffraction Analysis	55

CHAPTER 4 RESULTS AND DISCUSSIONS	56
4.1. Density	56
4.2. Fracture Surfaces Analysis	57
4.3. Microstructure	61
4.3.1. The optical micrographs	61
4.3.2. SEM micrographs	63
4.4. XRD analysis	66
4.5. Mechanical properties	68
4.5.1 Hardness	68
4.5.2 Tensile properties	69
4.6. Friction coefficient	71
4.7. Wear rates	74
4.8. Worn surfaces and wear debris	76
4.8.1. Worn surfaces of all sintered composite at normal load 15N	76
4.8.2. Wear debris of all sintered composite at normal load 15N	77
4.8.3. EDS analysis of wear debris at normal load 15N	78
4.8.1. Worn surfaces and wear debris of sintered Fe-Si-C composite	80
4.8.2. Worn surfaces and wear debris of sintered 0.50 Mo composites	83
4.8.3. Worn surfaces and wear debris of sintered 0.85 Mo composites	85
4.8.4. Worn surfaces and wear debris of sintered 1.50 Mo composites	87
4.9. Counter ball surfaces	89
CHAPTER 5 CONCLUSIONS AND RECOMMENDATIONS	90
REFERENCES	91
APPENDIX A	100
APPENDIX B	108
APPENDIX C	112
AUTHOR BIOGRAPHY	120

LIST OF TABLES

Table	Page
Table 2.1 Porosity, hardness, and porosity for large pores.....	19
Table 2.2 Relative importance of the forms of wear.....	28
Table 3.1 The chemical composition of mixed powder.....	51
Table 4.1 Total area of each phase of sintered materials	62
Table 4.2 Friction coefficient of sintered Fe-Mo-Mn-Si-C composite and sintered Fe-Si-C composite under difference Molybdenum content.	74
Table 4.3 Wear rate of sintered Fe-Mo-Mn-Si-C composite and sintered Fe-Si-C composite under difference Molybdenum content	75



LIST OF FIGURES

Figure	Page
Figure 2.1 Powder metallurgy application areas in automotive [3].....	4
Figure 2.2 Powder metallurgy process [5].....	5
Figure 2.3 Schematic of tool set for compaction [6].	6
Figure 2.4 Schematic diagram of sintering process.....	8
Figure 2.5 Isothermal transformation diagrams. (a) Carbon steel and steel alloyed with no carbide forming (b) carbon steel and steel alloyed with carbide forming [7].....	9
Figure 2.6 Effect of alloying element additions on ferrite hardness [5].....	10
Figure 2.7 The effect of molybdenum on the tempering of quenched 0.1 wt% C steels	11
Figure 2.8 Crystal structure of graphite	12
Figure 2.9 Hardness of various microstructure of steels containing up to 1.2wt.% C [10]	13
Figure 2.10 The micrograph of ferrite microstructure of low carbon steel.	14
Figure 2.11 The micrograph of pearlite microstructure of low carbon steel.	15
Figure 2.12 An orientation image of pearlite colonies.....	15
Figure 2.13 Body-centered tetragonal crystal structure of martensite.....	16
Figure 2.14 Micrograph of martensite microstructure (1220x)	17
Figure 2.15 Micrograph of bainite microstructure.	17
Figure 2.16 The optical micrograph of various particle size (a) SP (b) MP (c) MLP (d) LP..	18
Figure 2.17 Pores size distribution of all PM samples	19
Figure 2.18 Normalized wear scar depth of all samples under dry sliding condition	20
Figure 2.19 SEM micrograph of LP sample after 200 m under dry sliding condition.....	21
Figure 2.20 COF of all sintered samples under dry sliding condition.....	21
Figure 2.21 The particles bonding at difference temperature.....	22
Figure 2.22 Relative densities and open porosities of the Fe-Mn-Si compacts sintered at 1200 °C as a function of the isothermal holding time.	23
Figure 2.23 The sintered density of various SiC particle.	24

Figure 2.24 The schematic of pin on disc wear tester.....	25
Figure 2.25 The typical curve of friction coefficient and time.....	26
Figure 2.26 Schematic of adhesive wear mechanism.....	28
Figure 2.27 Schematic of two body abrasive wear mechanism.....	29
Figure 2.28 Schematic of three body abrasive wear mechanism.....	30
Figure 2.29 SEM micrograph of severe delamination wear.	31
Figure 2.30 SEM micrograph of mild delamination wear.	31
Figure 2.31 Schematic of oxidative wear mechanism.....	32
Figure 2.32 SEM micrograph of oxidative wear.....	33
Figure 3.1 Iron base particle powder	34
Figure 3.2 Pre-alloyed Fe-Mo-Mn powders.....	35
Figure 3.3 SiC powder.....	36
Figure 3.4 SiC powder in SEM.....	36
Figure 3.5 Zinc stearate powder.....	37
Figure 3.6 Argon gas cylinders.....	38
Figure 3.7 Nital etchant	38
Figure 3.8 The Digital balance (3-digit).....	39
Figure 3.9 The Analytical balance (4-digit).....	39
Figure 3.10 Powder blender.....	40
Figure 3.11 Hydraulic pressing machine	41
Figure 3.12 High vacuum sintering furnace SCHMETZ D59708 MENDEN	41
Figure 3.13 High precision cutting machine.....	42
Figure 3.14 Hot mounting press	42
Figure 3.15 Metallographic grinding/polishing machine.....	43
Figure 3.16 Silicon carbide paper.....	44
Figure 3.17 Micron polishing cloth.....	44
Figure 3.18 Diamond suspension size 6, 3 and 1 μm	45
Figure 3.19 Digital vernier.....	45

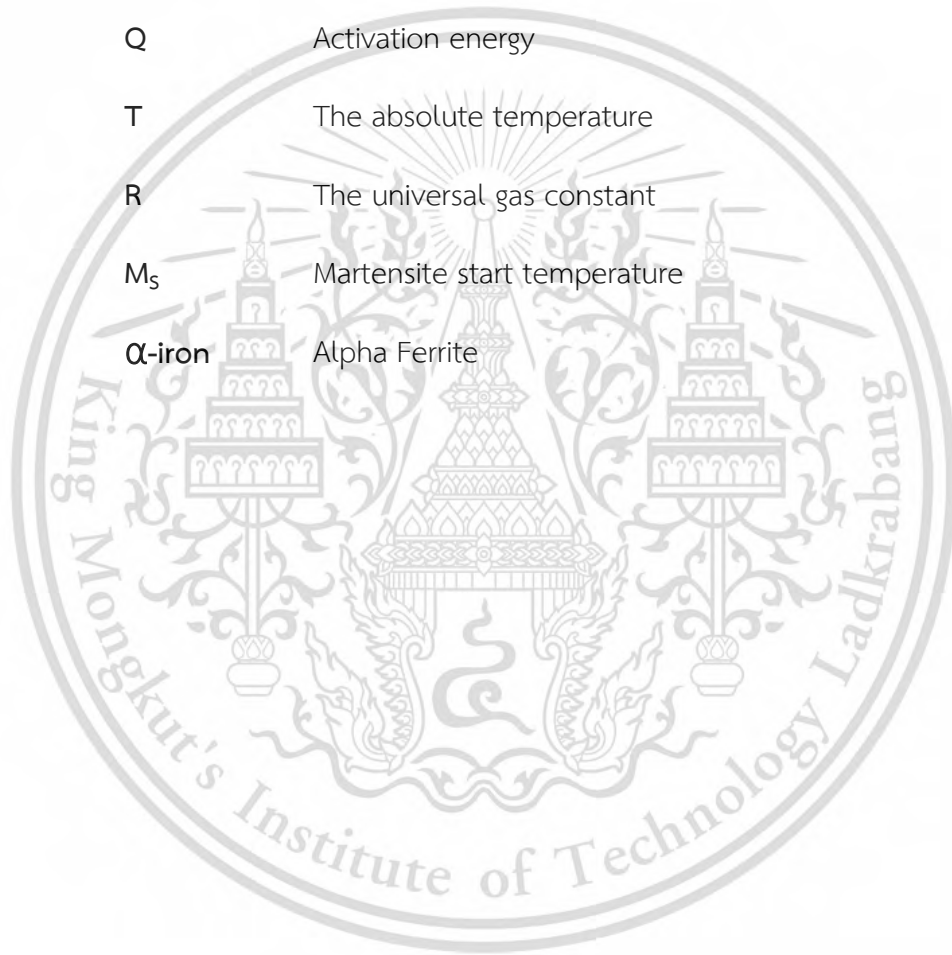
Figure 3.20 Instron-930 Macro hardness testing machine.....	46
Figure 3.21 Instron 8801 Universal Instrument.....	47
Figure 3.22 Optical microscope by Olympus STM7, Japan	48
Figure 3.23 Scanning electron microscope by Hitachi SU8230, Japan.....	49
Figure 3.24 X-Ray Diffraction Analysis	49
Figure 3.25 Pin-on-disc testing machine (ASTM G99)	50
Figure 3.26 The sketch of standard tensile test bar.....	51
Figure 3.27 Green disk dimensions.	52
Figure 3.28 The sintering profile.....	53
Figure 3.29 The schematic of ball-on-disc wear test set up.....	55
Figure 4.1 The average sintered density of sintered composites tensile test bars.	56
Figure 4.2 The average sintered density of sintered composite disks.....	57
Figure 4.3 SEM fracture micrographs of sintered composites (a, b) sintered 000Mo composite, (c) sintered 050Mo composite, (d) sintered 085Mo composite, (e) sintered 150Mo composite.....	59
Figure 4.4 EDS mapping of a sintered composite fracture surface.....	60
Figure 4.8 The X-ray diffraction patterns of the sintered composites.....	67
Figure 4.9 The hardness values of the sintered Fe-Mo-Mn-Si-C composites.....	69
Figure 4.10 The tensile properties of sintered composites.....	70
Figure 4.11 Friction coefficients of sintered composites tested at load of 5 N.	72
Figure 4.12 Friction coefficients of sintered composites tested at load of 10 N.....	73
Figure 4.13 Friction coefficients of sintered composites tested at load of 15 N.....	73
Figure 4.14 Plot of wear rate against normal load for different sintered composites.....	75
Figure 4.15 SEM micrograph of worn surface of sintered composite at load of 15N.....	76
Figure 4.16 SEM micrograph of wear debris of sintered composite at load of 15N.....	78
Figure 4.17 EDS spectrum of wear debris from sintered 000Mo composite.....	78
Figure 4.18 EDS spectrum of wear debris from sintered 050Mo composite.....	79
Figure 4.19 EDS spectrum of wear debris of sintered 085Mo composite.....	79

Figure 4.20 EDS spectrum of wear debris from sintered 150Mo composite.....	80
Figure 4.21 SEM images of worn surfaces of sintered 000Mo composite.....	81
Figure 4.22 SEM images of wear debris of sintered 000Mo composite.....	82
Figure 4.23 SEM images of worn surfaces on sintered 050Mo composite.....	83
Figure 4.24 SEM micrograph of wear debris of sintered 050Mo composite.....	84
Figure 4.25 SEM images of worn surfaces of sintered 085Mo composite.....	85
Figure 4.26 SEM images of wear debris of sintered 085Mo composite.....	86
Figure 4.27 SEM images of worn surfaces of sintered 150Mo composite.....	87
Figure 4.28 SEM micrograph of wear debris of sintered 150Mo composite.....	88
Figure 4.29 SEM images of counter ball surfaces test at load of 15N.....	89



LIST OF SYMBOLS

D_o	The degree of densification
ρ_a	The apparent density
ρ_s	The density of the fully consolidated metal
Q	Activation energy
T	The absolute temperature
R	The universal gas constant
M_s	Martensite start temperature
α -iron	Alpha Ferrite



LIST OF DEFINITIONS

PM Powder Metallurgy

H₂ Hydrogen

CO Carbon Monoxide

CO₂ Carbon Dioxide

N₂ Nitrogen

Fe Iron

Ni Nickel

Mn Manganese

Si Silicon

Cr Chromium

W Tungsten

V Vanadium

Mo Molybdenum

C Carbon

Al Aluminum

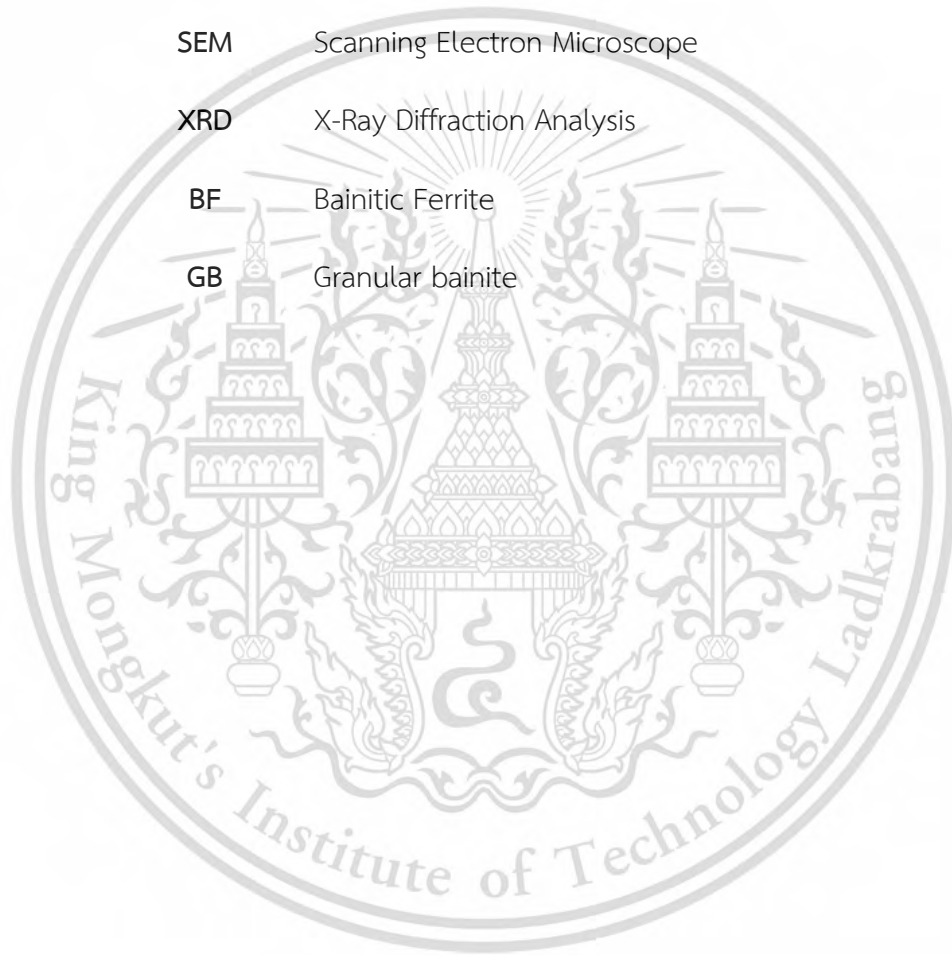
SiC Silicon Carbide

MoS₂ Molybdenum Disulfide

BN Boron Nitride

Fe₃C Cementite

IT	Isothermal transformation diagrams
BCC	Body centered cubic
BCT	Body-centered tetragonal
M-A	Martensite-Austenite
OM	Optical Microscope
SEM	Scanning Electron Microscope
XRD	X-Ray Diffraction Analysis
BF	Bainitic Ferrite
GB	Granular bainite



CHAPTER 1

INTRODUCTION

1.1. Research Background

In recent year, utilization of powder metallurgy has been rapidly increasing in the aerospace, marine and automotive component in order to fulfil the requirements of suitable mechanical and physical properties. However, these materials limit their application usage due to the tribological properties [1]. Tribology involves the friction, adhesion, wear, and lubrication of solids in contact. Friction and wear are importance when considering the efficiency or operating lifetime of a product because wear often a major factor in limiting the suitable lifetime of a component. Wear is a materials removal from the contact surface between two surfaces in relative motion. The wear behavior of wrought materials is totally different from the powder metallurgy (PM) materials due to the pores in the PM materials. The wear rate of alloys is directly proportional to the amount of porosity. Because of alloys formed through PM route are typically porous. The presence of pores in the sintered PM materials acts as main source for crack initiation, and wear follows crack propagation which further leads to weakness [2].

Thus, lubricants are applied for extend service lives and reduce maintenance operation of moving components because it reduces heat between contacting surfaces in relative motion and tends to improve wear properties. A solid lubricant is suitable for applying in the asperity's regions, where a liquid lubricant is uncomfortably refilled during maintenance. Such as lubrication under extreme environment, where tribological contact surfaces still need to be efficiently, solid lubricants are needed. One simple way to apply a solid lubricant is to impregnate in a metal matrix of a moving part. Sintering a mixture of metal powder and solid lubricant is a traditional method for processing a self-lubricating composite.

A self-lubricating composite material with high mechanical strength, great wear resistance and low friction coefficient are recommended for improve the tribological properties of sintered composite materials. Self-lubricating composite materials are produced by adding solid lubricants in the matrix phase. The addition of solid lubricants in the matrix phase as reinforcing elements create a new material for reducing friction. These solid lubricants form a tribofilms during the in-service wear of the component which will help to reduce the friction of the components.

Among various types of solid lubricants, sintered Fe-Mo-Mn-Si-C composites were selected for study in this work because it commonly applied as train brake linings. These sintered composites showed promising mechanical properties and had graphite-containing particles embedded in iron base matrices, act as solid lubricant, which are the important role on braking performance.

This present work is focused on the influence of molybdenum content in pre-alloyed powders, used for making composite matrices, on microstructure, mechanical properties and tribological properties of sintered composites. Pure iron powder with 4% SiC was also used for producing a sintered composite as the reference material.

1.2. Objective

- 1) To produce sintered Fe-Mo-Mn-Si-C composite and sintered Fe-Si-C composite as self-lubricating materials.
- 2) To investigate the effects of Molybdenum on microstructure and mechanical properties of sintered Fe-Mo-Mn-Si-C composite and sintered Fe-Si-C composite.
- 3) To investigate the effects of Molybdenum on tribological properties and wear behavior of sintered Fe-Mo-Mn-Si-C composite and sintered Fe-Si-C composite.

1.3. Scopes

- 1) Mixing Fe-Mo-Mn powder which have varies Molybdenum content 0.50, 0.85, 1.50 wt.% and Fe-Si-C powder with 4 wt.% SiC.
- 2) Compacting the mixed powder and sintering at 1250°C for 45 minutes under vacuum and slowly cooled in the furnace.
- 3) Characterization microstructure and phase analysis of sintered Fe-Si-C composite and sintered Fe-Mo-Mn-Si-C composite specimens by optical microscope (OM), scanning electron microscope (SEM) and X-Ray Diffraction (XRD)
- 4) Mechanical properties investigation of sintered Fe-Si-C composite and sintered Fe-Mo-Mn-Si-C composite by Rockwell hardness test and tensile test.
- 5) Tribological analysis of sintered Fe-Si-C composite and sintered Fe-Mo-Mn-Si-C composite by pin on disc test.
- 6) Characterization of worn surfaces and wear debris of sintered Fe-Si-C composite and sintered Fe-Mo-Mn-Si-C composite by SEM and EDS.

1.4. Expected Benefits

The sintered Fe-Mo-Mn-Si-C composite and sintered Fe-Si-C composite for applying in train brake lining of high-speed train with great mechanical properties and excellent tribological properties for long life cycle time.

CHAPTER 2

LITERATURE REVIEW

2.1. Powder metallurgy (PM)

Powder metallurgy is a metal forming process that widely used in many applications including automotive part [3] as show in Figure 2.1. Because PM is a sustainable technology, cost and energy saving, reliable precision parts consistently which offer a high performance and greater flexibility of designing, and parts can be produced with complex shapes and functions compared with traditional manufacturing methods such as extrusion, casting, stamping, forging, and machining. The one of main advantage of PM is the wide variety of materials used which can be mix the different metal powders together. This leads to the possibility to create new composite materials with special physical and mechanical properties in a component [4].

The process of powder metallurgy is shown in Figure 2.2. The first step starts from powder selection by the requirements of the part to be produced and mixing powder together. The mixed powders are pressed into the desired shape by high pressure pressing machine, then heating the compressed or green material in a controlled atmosphere for bonding the powder particles.

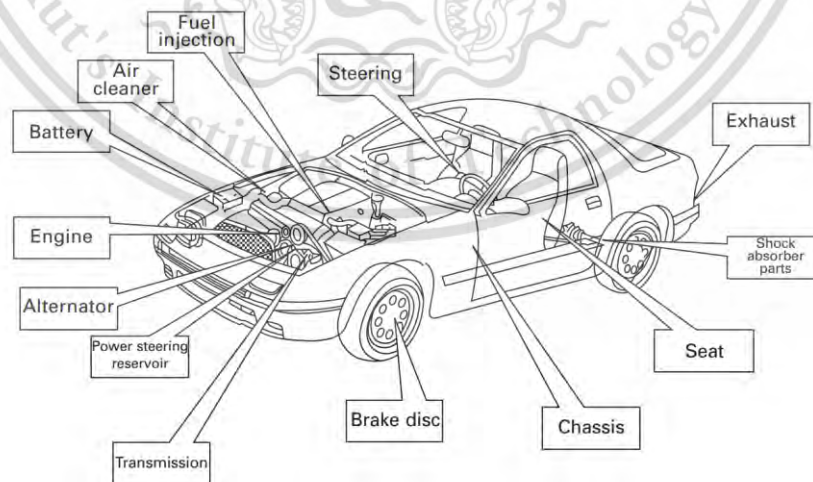


Figure 2.1 Powder metallurgy application areas in automotive [3].

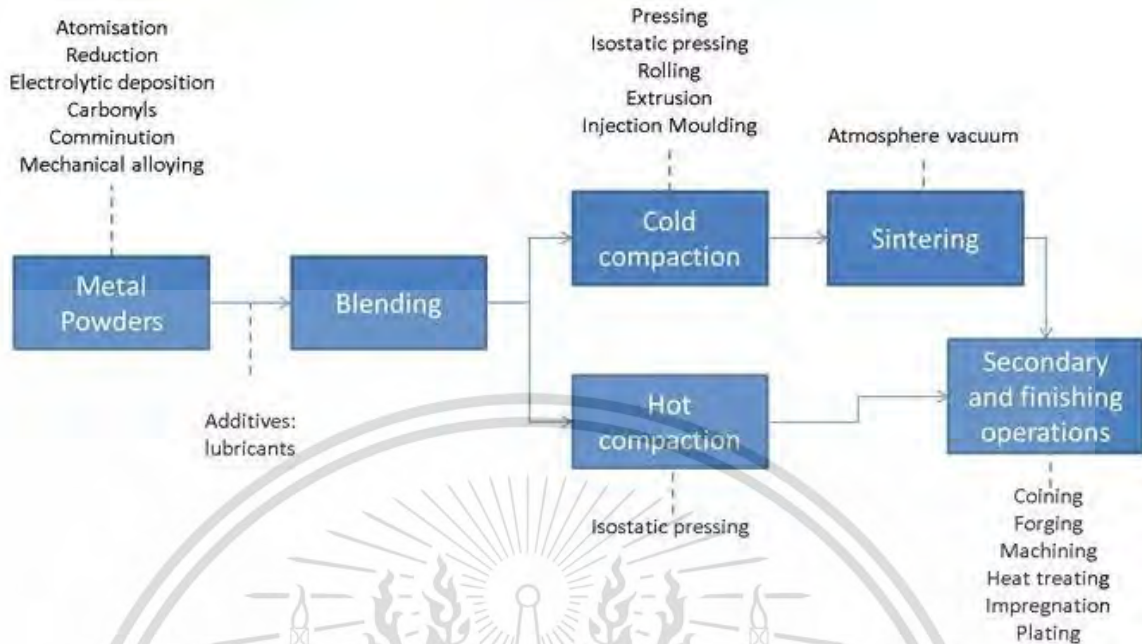


Figure 2.2 Powder metallurgy process [5].

2.1.1. Powder characteristic

The characteristics of metal powders and alloy chemistry depend on the manufacturing processes used for their production. Powders can be characterized by several parameters such as particle size and shape, distribution of particle, surface area, and ability of powder to flow which influences it fills a die cavity [6]. All of powder parameters influence are important for the powder density which referred to the mechanical properties of PM materials. The degree of densification (D_o) is a useful quantity that indicate the consolidation of powders which can defined as Equation 2.1. Where the ρ_a express the apparent density, and ρ_s is the density of the fully consolidated metal.

$$D_o = \frac{\rho_a}{\rho_s} \times 100 \quad \text{(Equation 2.1)}$$

2.1.2. Powder mixing

The powder mixing process employed to mix the raw powder with some alloy elements and by adding lubricant or some special additives to achieve the desired properties of the materials [5]. Powders with desired amounts are mixed until a homogeneous mixture is obtained in a suitable mixing machine for a proper time.

2.1.3. Compaction

The aim of compaction step is obtained mixed powder into mold and die, and compact to maintain required shape and size. Compacting is carried out with sufficient strength and density with hydraulic pressures. The compaction operation must ensure that the green density is as uniform as possible, to achieve the maximum final product mechanical quality. The improvement of uniformity of the green density is apply the pressure from both ends [6]. Figure 2.3 show the schematic of tool set for compaction, it consists of upper punch, lower punch and die for pressing the powder to green specimen.

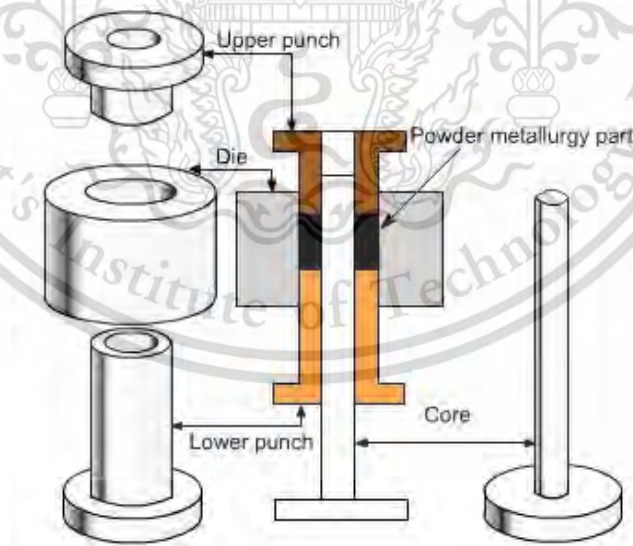


Figure 2.3 Schematic of tool set for compaction [6].

2.1.4. Sintering

The sintering process refers to the application of heat to the green compact for increasing of strength and structural integrity by the powder particles bonding. The driving force for increasing the density and particle contact area during sintering is the reduction of the surface energy of the powder particles by a decrease in the total surface area of the compact, due to the closure of pores between powder particles. Not only the reduction of the surface energy is the driving force, but also diffusion mechanism is leads to the increase in density. The diffusion mechanism can define as Equation 2.2, where D_0 is the frequency factor, Q is an activation energy, T is the absolute temperature, and R is the universal gas constant. For each material, the activation energy and frequency factor are characteristic thermal constants. Therefore, increasing the sintering temperature significantly increases the rate at which a powder compact density [6].

The sintering process are dividing into three stages. The initial stage is heating the specimen to evaporated or decompose the wax lubricant or binder that added to the powder for the easier in compaction process. The intermediate stage is sintering stage, the sinter neck formation and merge between particle result in increasing of density and strength and progressed through atomic and particles diffuse as Figure 2.4. In this stage, the grain size is increase while the pore size is shrinkage led to volume decreasing. The last is cooling stage, the cooling rate is depended on the final structure and mechanical properties needed.

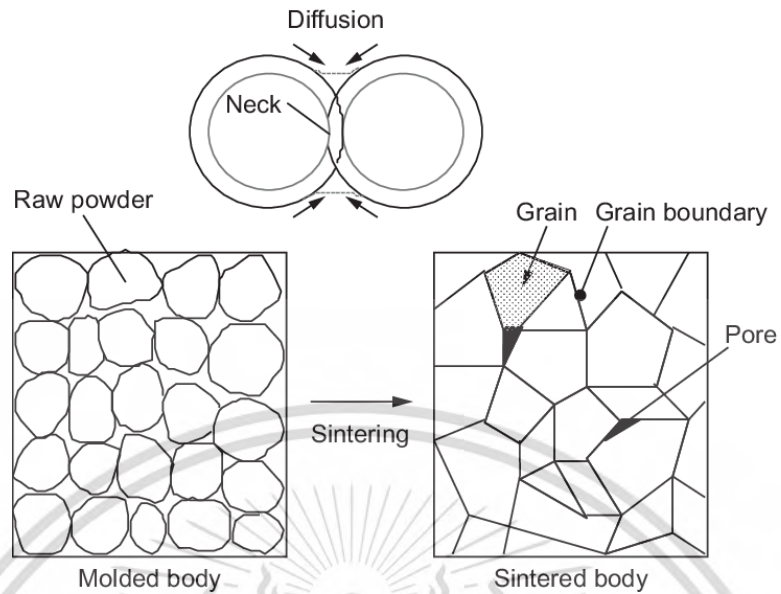


Figure 2.4 Schematic diagram of sintering process

2.1.5. Sintering atmosphere

The sintering process should conduct under good protective or vacuum atmosphere to prevent excessive oxidation of the powder surfaces. The heat for sintering is produced by hydrogen (H_2), CO, and CO_2 which can prevent of the powder surfaces during sintering. Alternatively, nitrogen (N_2) mixed with hydrogen atmospheres can be used.

2.2. Alloying Element

Alloying element were added in base metals for changing the chemical composition with purpose to improve or adjust its material properties. While there are many alloying elements used to achieve various enhanced properties. Each alloying elements have their own effect on the properties of materials.

2.2.1. Effects of alloying element on transformation diagrams

The alloying element that influent on transformation diagram of austenite, pearlite, bainite and martensite can divide into two types. The first type is alloying elements that dissolve only in ferrite and cementite without the formation of carbide such as Ni, Mn, Si. Figure 2.5a show the transformation diagrams of carbon steel and steel alloyed with no carbide forming elements. The results show that these steels alloyed slow down the transformation time (shifting of start curves to longer times). The second type is carbide-forming elements such as Cr, W, V, and Mo. Figure 2.5b show the transformation diagrams of carbon steel and steel alloyed with carbide forming elements. Its changing in the kinetics of isothermal transformations differently at different temperatures. Therefore, this type of steel alloyed have different transformation rate separated by a region of relative stability undercooled austenite [7]. However, the presence of alloying element reduces the critical cooling rate and shifts the transformation start curves on isothermal transformation diagrams (IT) to longer times which lead to hardenability improvement [8].

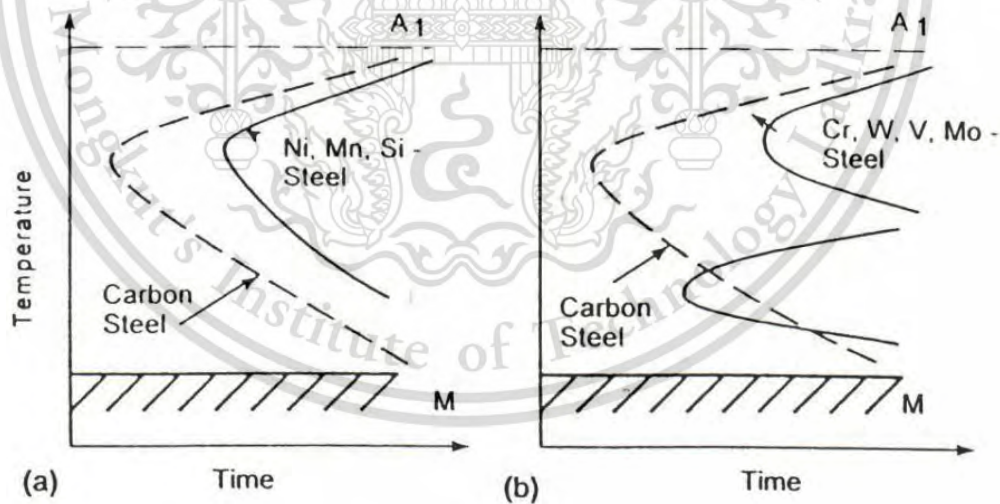


Figure 2.5 Isothermal transformation diagrams. (a) Carbon steel and steel alloyed with no carbide forming (b) carbon steel and steel alloyed with carbide forming [7].

2.2.2. Effect of alloying element on ferrite hardness

The hardness value of ferrite is also affected by formation of solid solution. The solid solution produced by additional alloying element in base metal. Figure 2.6 show the effect of substitutional alloying element additions on hardness of ferrite. The results show that hardness increase caused by substitutional solution. Si and Mn element gives high hardness increase, on the other hand, Cr show the smallest relatively effect on hardness of ferrite [7].

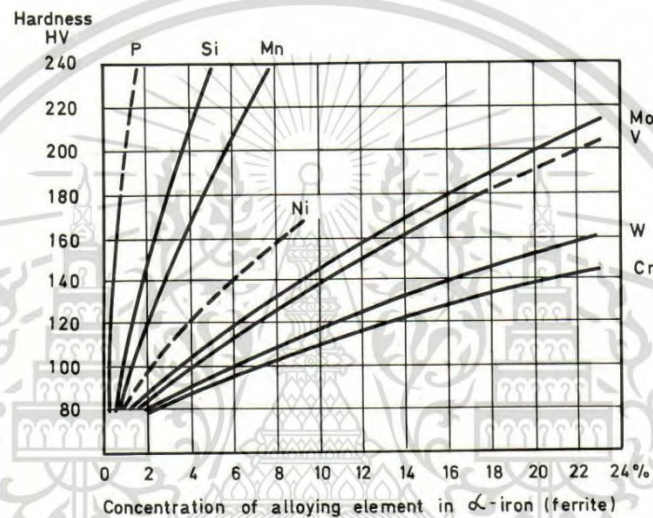


Figure 2.6 Effect of alloying element additions on ferrite hardness [5]

2.2.3. Effect of alloying element on the formation of alloy carbides (Secondary hardening)

In the secondary hardening process of material which add the alloying element such as Cr, Mo, V, and W, the carbides in coarse cementite dispersion are replaced by a new and finer alloy carbide dispersion, results in higher hardness. Figure 2.7 show the effect of molybdenum on hardness of secondary hardening. The results show higher hardness value while increase percent of molybdenum [7].

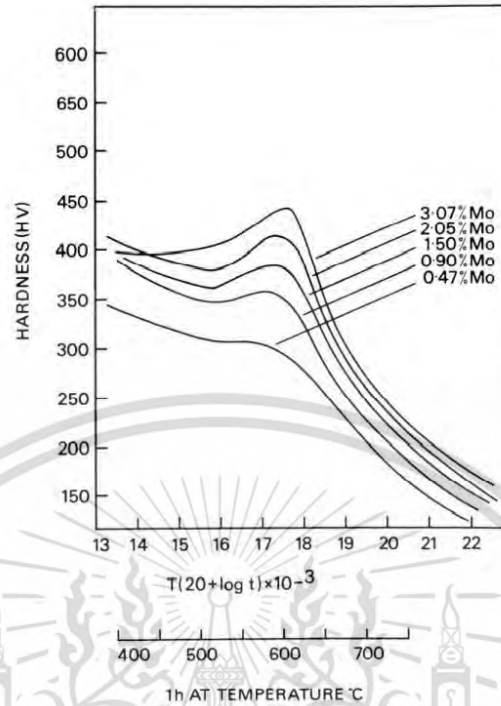


Figure 2.7 The effect of molybdenum on the tempering of quenched 0.1 wt% C steels

2.3. Self-lubricant material

Self-lubricant material is one type of solid lubricant which is suitable for the applications in the asperity regions. While liquid lubricant is uncomfortably to be refilled during maintenance. Because liquid lubricant can oxidize and decompose when performed at high temperature, leading to a decrease in its efficiency and performance. On the other hand, self-lubricant or solid lubricant can utilize lubrication at various conditions such as high temperature, strong radioactivity, high-pressure, corrosive environments, and vacuum atmosphere. While two components move sliding each other, a self-lubricant material will create a lubricant film on the surface by releasing a solid lubricant to prevent the direct contact between their surfaces, resulting in the reduction of friction and mechanical interactions between surfaces in relative motion. There are various types of solid lubricants such as graphite, molybdenum disulfide (MoS_2), and boron nitride (BN) [9].

2.3.1 Graphite

Graphite is a solid lubricant which has a hexagonal crystal structure. The crystal structure of graphite consists of thin parallel planes (graphene) which bonded by weak Van der Waals forces to each other as Figure 2.8. Each carbon atoms of graphene are bonded by strong covalent bond to three other atoms with angle 120° . The weak bond between the graphenes cause easily shearing of the planes toward the direction of the force. The graphene that released from graphite crystals by lamellar displacement create graphite films on surfaces results in lower coefficient of friction. However, application of graphite in practical is limited at high temperature because of oxidation. But additives composed of inorganic compounds can added to enable use.

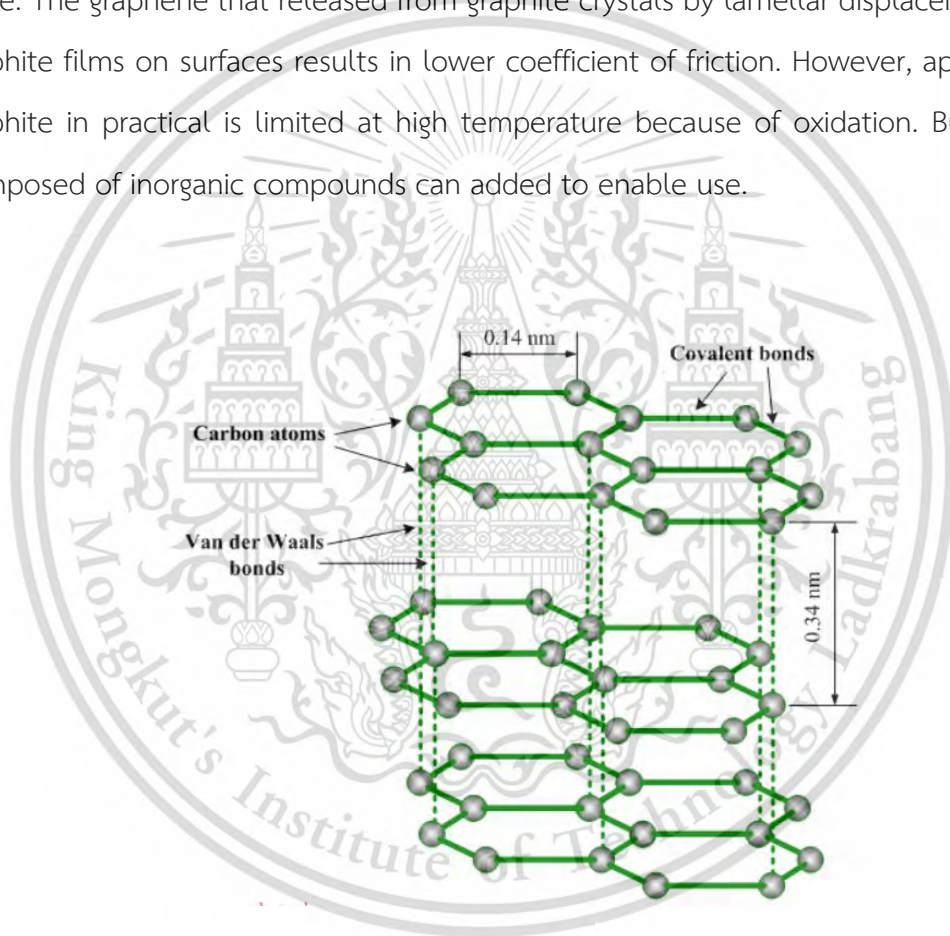


Figure 2.8 Crystal structure of graphite

2.4. Microstructure

The microstructure used to describe the structure of material such as phase, arrangement of phases and defects of material in a microscopic scale, which can be observed by microscopic techniques. The microstructure of material depends on many factors such as chemical composition, homogeneity, processing, and section size. Moreover, it can strongly influence to properties of material such as strength, ductility, toughness, hardness, corrosion and wear resistance, and temperature behavior, which depend on phase structure of it. Figure 2.9 shows hardness of various microstructure of steels containing up to about 1.2wt.% carbon. Martensite demonstrates the highest hardness, while hardness of tempered martensite and bainite have slightly lower. However, pearlite and ferrite show significantly lower hardness, whereas ferrite and spheroidized carbide indicated the lowest hardness compare with others.

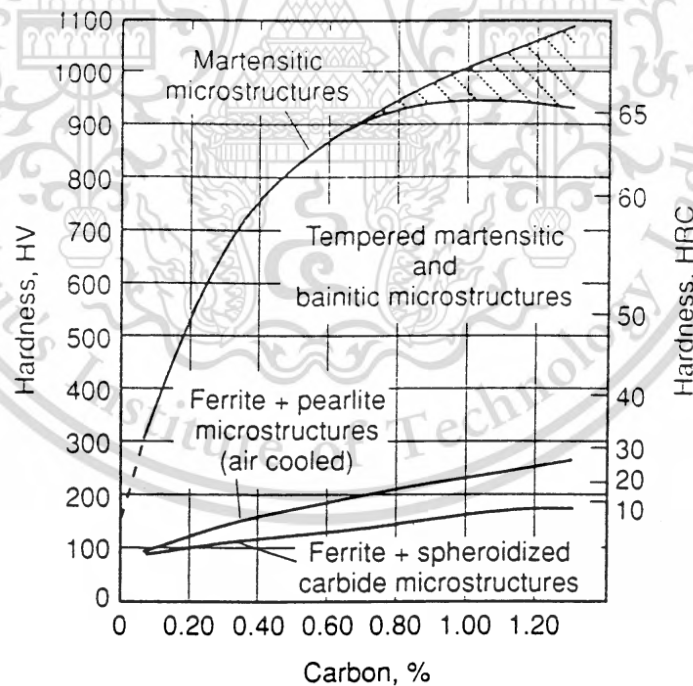


Figure 2.9 Hardness of various microstructure of steels containing up to 1.2wt.% C [10]

2.4.1. Ferrite microstructure

Ferrite microstructure presented in body centered cubic (BCC) crystal structure which stable at the temperature under 912°C. The solubility of carbon atom in ferrite phase is very low, maximum soluble is 0.022% at 727°C and 0.008% at room temperature. This phase has low dislocation motion resistance due to its crystal structure, which effect to low in its strength. Figure 2.10 illustrates the micrograph of ferrite microstructure.

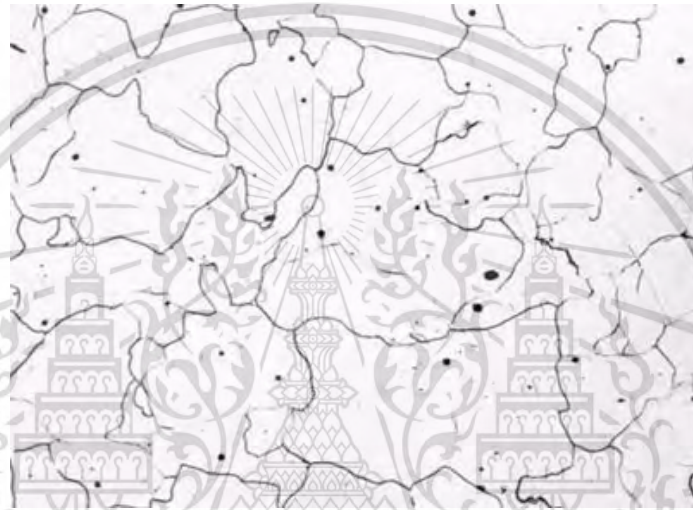


Figure 2.10 The micrograph of ferrite microstructure of low carbon steel.

2.4.2. Pearlite microstructure

Pearlite microstructure is a metastable lamellar that mixed of two phases, ferrite, and cementite (Fe_3C) which forms at temperatures below the lower critical temperature. Cementite is a metastable phase which has compound of carbon and iron with the orthorhombic crystal structure. Under proper temperature, cementite can transform to graphite. The distance layer between ferrite and cementite is known as the interlamellar spacing [11]. The mechanical properties such as hardness of a fully pearlitic steel are varying with the interlamellar spacing. The small interlamellar spacing is known as fine pearlite, while large interlamellar spacing known as coarse pearlite which has lower hardness. The pearlite can made finer by heat treatment process. Figure 2.11 and Figure

2.12 illustrates the micrograph and crystallographic orientation image of pearlite microstructure. The orientation image indicate that the crystallographic orientation is homogeneous within a pearlite colony.

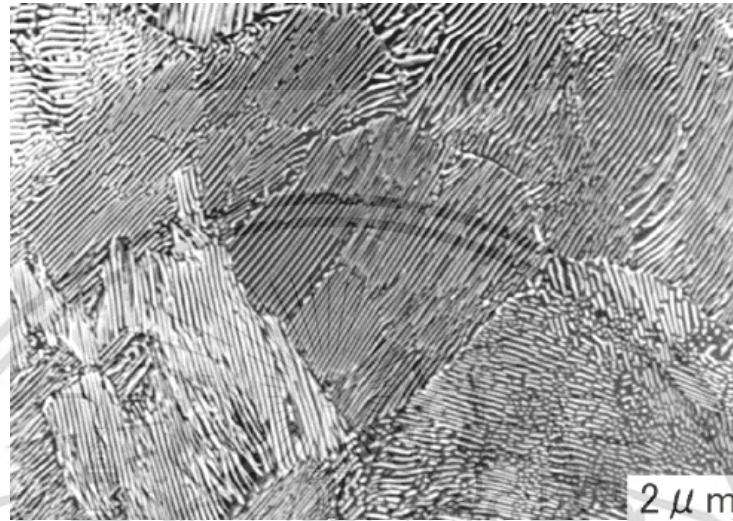


Figure 2.11 The micrograph of pearlite microstructure of low carbon steel.

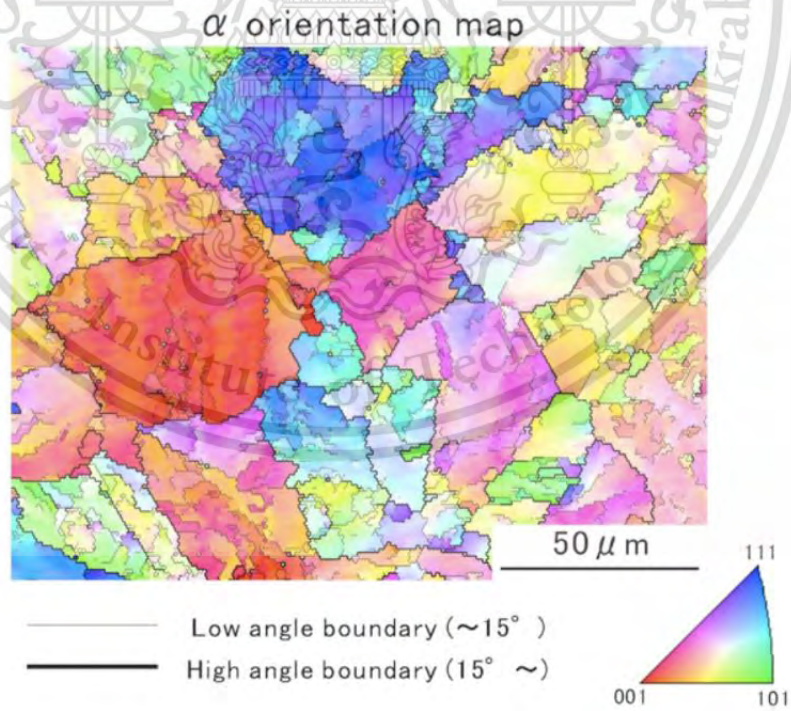


Figure 2.12 An orientation image of pearlite colonies.

2.4.3. Martensite microstructure

Martensite microstructure presented in body-centered tetragonal (BCT) crystal structure which formed by rapidly cool of austenite to below martensite start temperature (M_s) results in diffusionless transformation of carbon atom [11]. Because of high cooling rate, carbon atoms do not have enough time to diffuse completely into cementite phase. Figure 2.13 illustrate BCT structure of martensite, where circles are presented of iron atoms and x are presented of carbon atoms. Figure 2.14 shows micrograph of martensite with magnification of 1220x. The hardness and strength of martensite varies relational with carbon in austenite up to about 0.5% C. For carbon more than 0.5% in the austenite increases, the hardness and strength go down due to the austenite unable to convert to fully martensite (retained austenite becomes increasing).

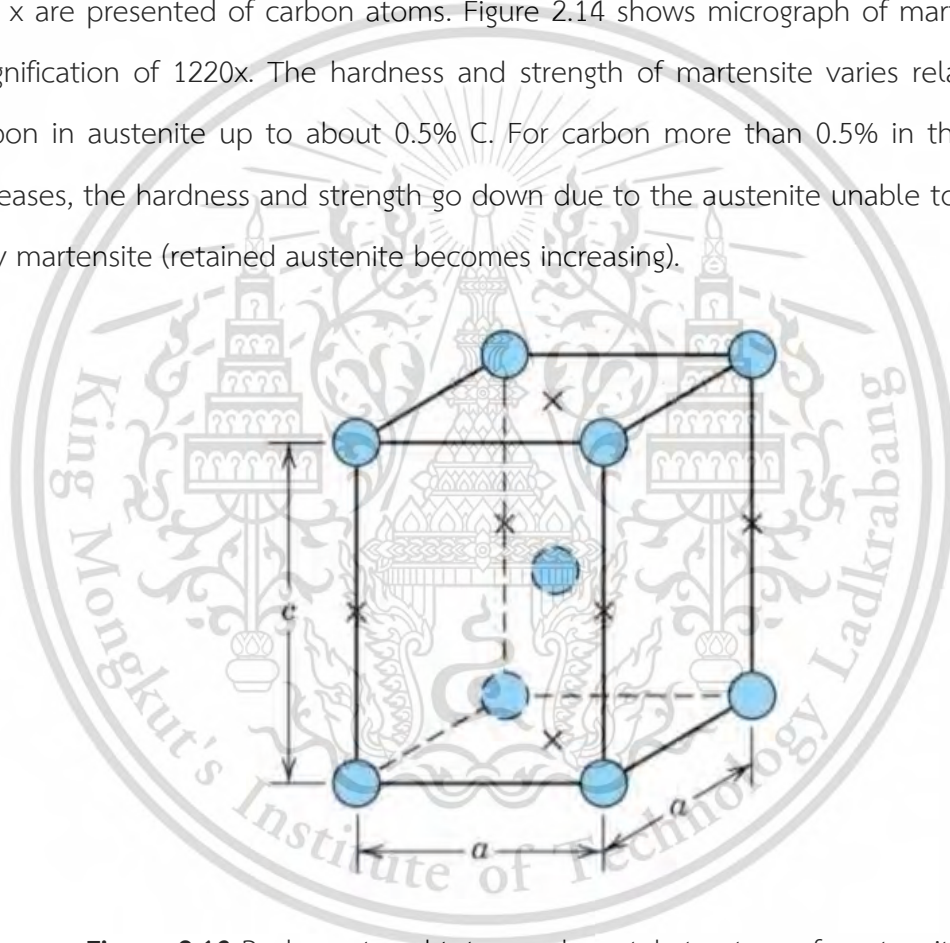


Figure 2.13 Body-centered tetragonal crystal structure of martensite



Figure 2.14 Micrograph of martensite microstructure (1220x)

2.4.4. Bainite microstructure

Bainite is microstructure that consist of ferrite phase and finely dispersed cementite as Figure 2.15 which formed by decomposition of austenite at above martensite start temperature and under pearlite finish temperature in time-temperature-transformation diagram. Bainite can exist without presence of cementite, where martensite-austenite (M-A) constituent would be found instead.

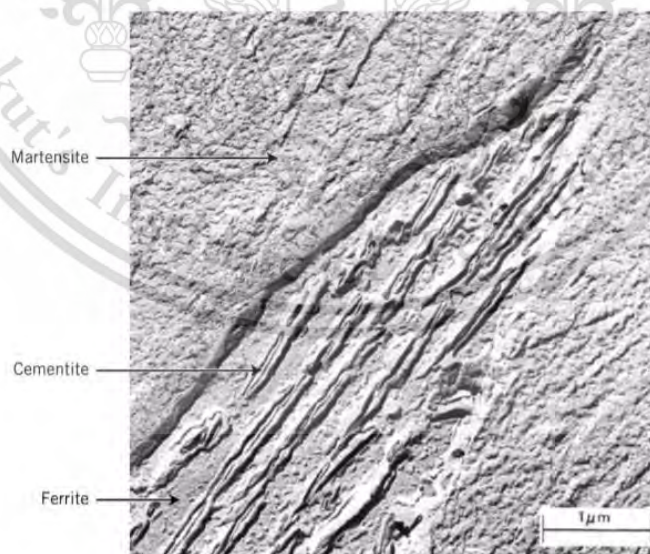


Figure 2.15 Micrograph of bainite microstructure.

2.5. Porosity

Figure 2.16 show the optical micrograph of various particle size, the evident show that small particle (SP) size gives the lowest porosity, while the large particle size (LP) shows the highest porosity. Moreover, the mixture of medium and large powders size (MLP) showed an increase in porosity, when compare with medium particle size (MP). Porosity, hardness, and porosity for large pores are shown in Table 2.1. It can be concluded that this sequential order for porosity is from SP to MP, MLP and LP with increasing in porosity. Pore size distribution is shown in figure 2.17, to study that both total porosity and the size of the pores have an influence on the tribological behavior [12].

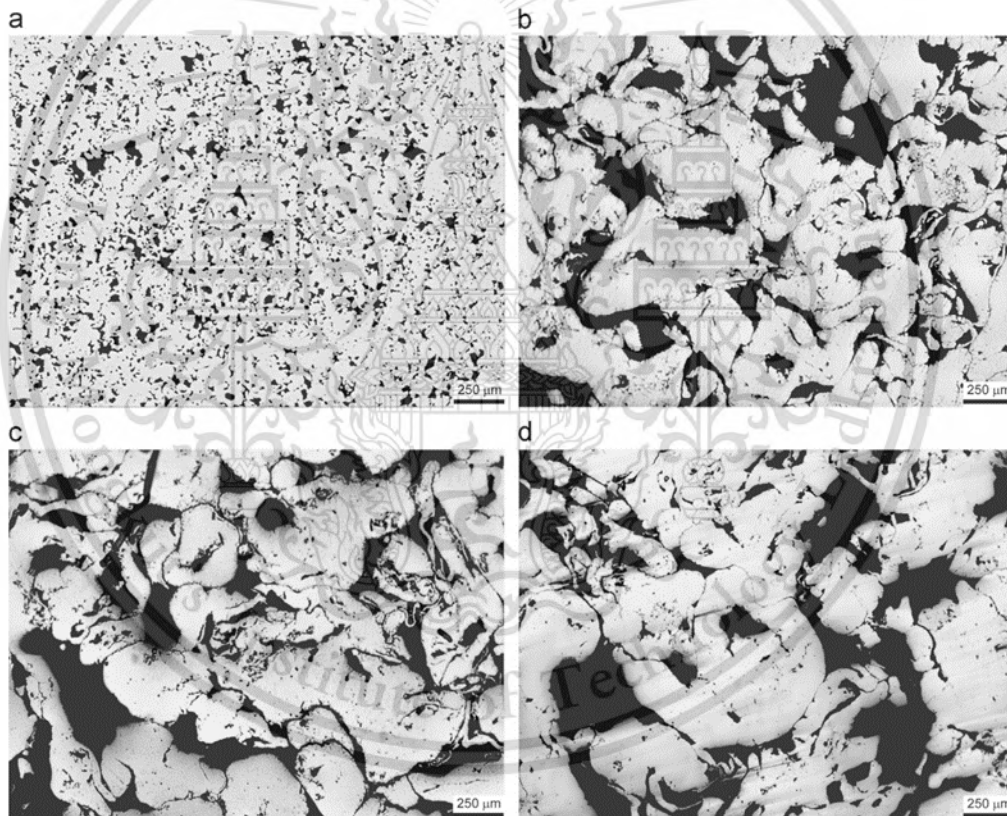


Figure 2.16 The optical micrograph of various particle size (a) SP (b) MP (c) MLP (d) LP

Table 2.1 Porosity, hardness, and porosity for large pores

Sample	Porosity (%)	Vickers Hardness, 30 HV	Porosity for large pores (%)
SP	7.6	123	0
MLP	22.2	101	14.3
MP	24.4	72	17.0
LP	28.8	69	21.4

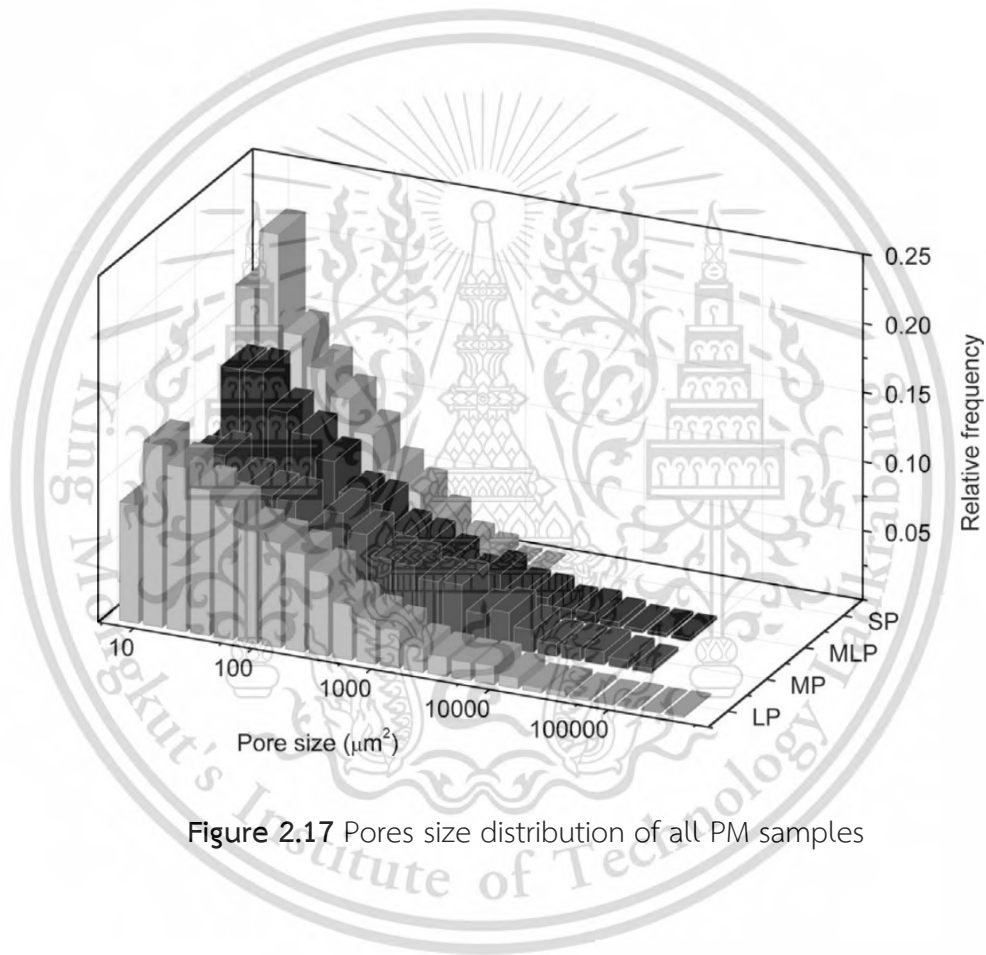


Figure 2.17 Pores size distribution of all PM samples

Figure 2.18 shows normalized wear scar depth of all sintered samples under dry sliding condition, respectively. It is evident that the total wear scar depth increasing depends on decreasing porosity. It shows that LP which has the highest porosity, has the lowest wear scar depth compared with others. It can be concluded that the amount of material removed is lower when the pores are present, because of the increasing of porosity. However, after the pores are closed (at after 200 m), all the samples demonstrate the same wearing process as they are the same material. Figure 2.19 presents SEM micrograph of LP sample after 200 m of dry wear, the pores are closed with flake-like shape. The same result is found in the other samples. This is because the plastically deformed material around the pores and elongates in the sliding direction at the surface and sub-surface, then the propagation of elongated pores near the surface forms flake-like debris during repeated revolutions. Figure 2.20 shows the coefficient of friction of all sintered samples under dry sliding condition. At the first few meters of sliding of COF, the result shows the influence of pores on the COF at this initial transient. After the pores are closed, the COF are constant at values around 0.70–0.75. As a conclusion, pores can be affecting the wear properties of the material until they close [12].

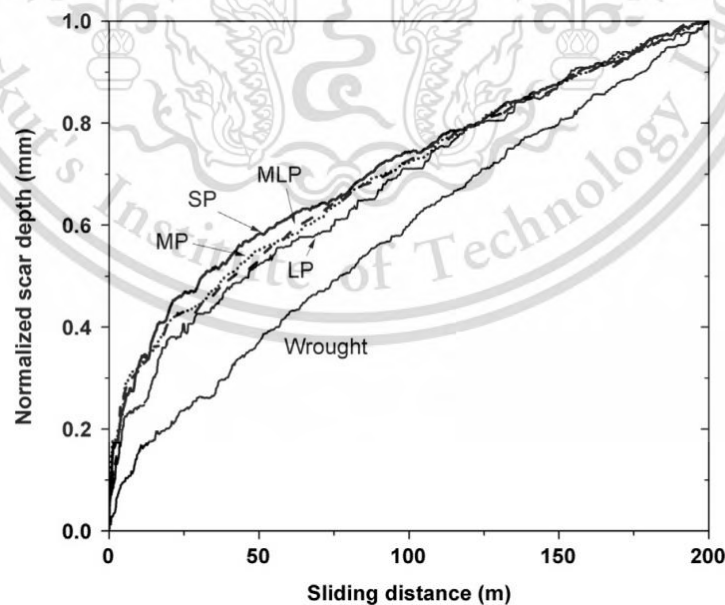


Figure 2.18 Normalized wear scar depth of all samples under dry sliding condition

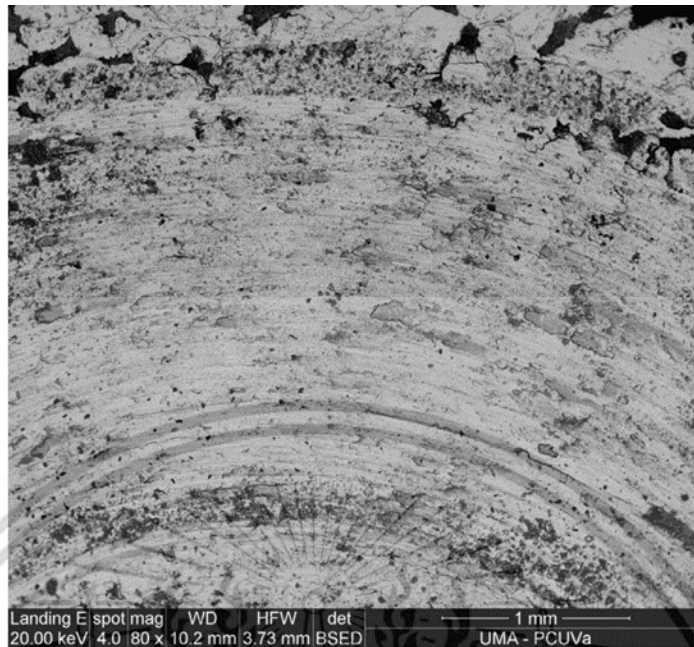


Figure 2.19 SEM micrograph of LP sample after 200 m under dry sliding condition

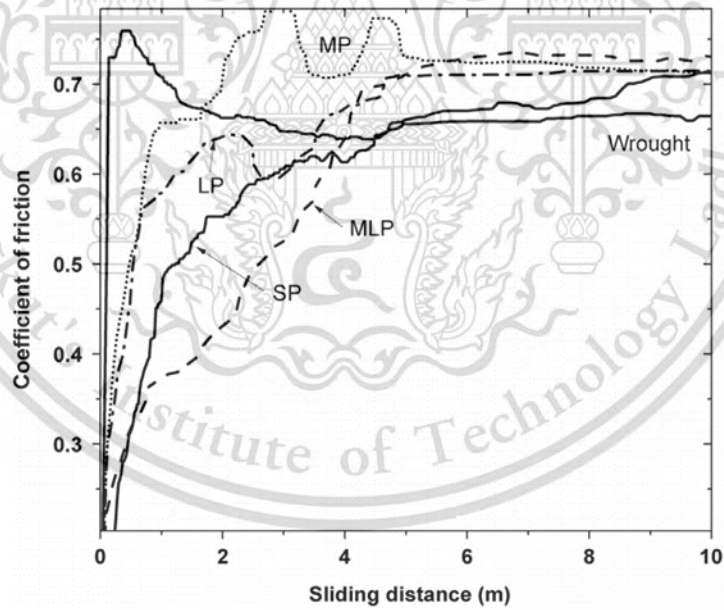


Figure 2.20 COF of all sintered samples under dry sliding condition.

2.6. Density

In sintered composite materials, the green densities were lower than sintered densities because of densification of particle bonding. Green density is the ratio of external and metal powder volumes before being sintered which indicates that how the powder particles are packed together. Powder compact of high green density helps accomplish densification during sintering. Improvements in green density may also be affected by employing smooth and regularly shaped annealed particles with high particle densities.

During the sintering process, powder particles bond to each other. The particles do not actually reach melting temperature during sintering, but rather neck is formed on the contacting areas at elevated temperatures. Due to sintered neck growth, the pores were filled, cause densification and shrinkage of the component, then the void spaces between the powder particles were removed [13], [14]. Sintered density increased with increasing sintering temperatures (Figure 2.21) and the amount of time spent at temperature as in Figure 2.22. In general, the open porosities of all the sintered alloys decrease with the increase of the isothermal holding time. However, further increasing the isothermal holding time has a limited effect on eliminating the open porosities [15], [16]. While the part was heated, the size of the part is reduced along with the porosity size. Hence, higher temperatures and longer sintering will form the particle better bonds.

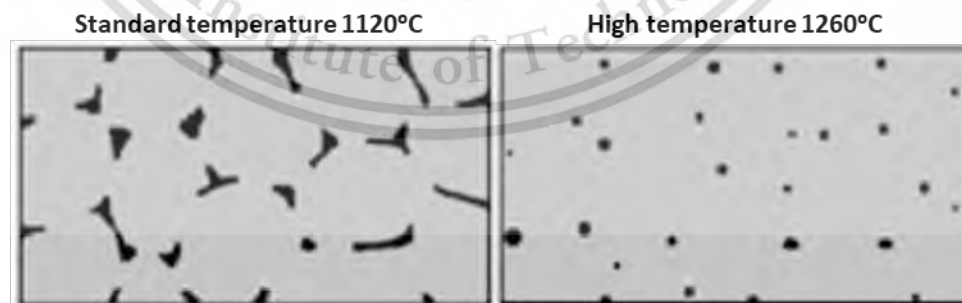


Figure 2.21 The particles bonding at difference temperature.

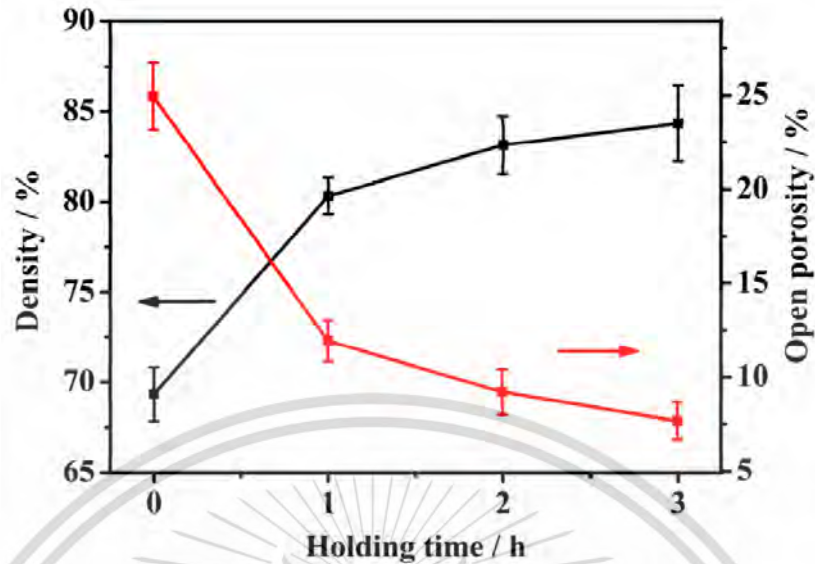


Figure 2.22 Relative densities and open porosities of the Fe-Mn-Si compacts sintered at 1200 °C as a function of the isothermal holding time.

2.6.1. Effect of SiC on sintered density

The sintered density of various SiC particle is presented in Figure 2.23. The theoretical density illustrates maximum densification in theoretical state. Because this state can ascribe as no void in density of composite, which is higher compared to experimental density. The electric resistance setup (ERS) shows better density than conventional sintering (CS) because ERS contribute an improved consolidation, grain refinement, and particle surface heating, which all result in higher densification. Moreover, the graph indicates that the addition of SiC increases the density of composites, as SiC particles provide higher density compared to the matrix material.

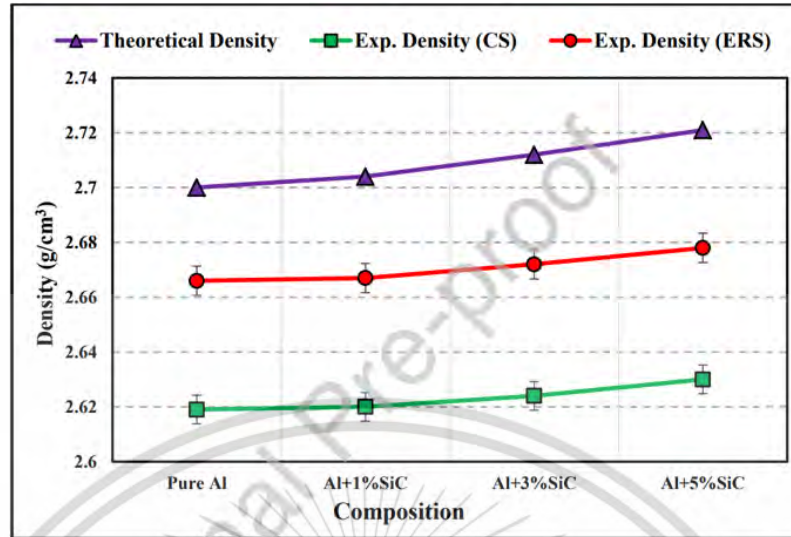


Figure 2.23 The sintered density of various SiC particle.

2.7. Wear testing

Wear testing is carried out to determine the amount of materials removed, to predict the wear performance and to investigate the wear mechanism of a component after service for a period of time. The wear properties can be expressed by various way such as mass loss, volume loss, the geometry and size of wear debris, the character of worn surface, and type of wear. Wear measurement can be done in a common technique using precision digital balance to measure the mass loss. The microscope also used for measuring the wear depth and cross section area of a wear track to define the wear volume loss. The wear testing is performed to evaluate the wear properties to determine whether material is appropriate for a specific wear application, to select the proper surface engineering technology to reduce wear, and to investigate the effect of treatment conditions on the wear performance. There is various type of wear test such as an abrasive wear tester, a rolling sliding wear tester, and a pin on disc wear tester.

2.7.1. The pin on disc wear tester

The pin on disc test is widely used to determine the wear properties because economic cost, short testing period, and easy to access [17]. The schematic of pin on disc wear tester is show in Figure 2.24. The pin on disc tester machine consists of a pin with various geometry, which attached with the precisely weight at a specified load. The most popular geometry of the pin is cylindrical and spherical due to the uniform loading. The pin on disc wear testing is carried out to evaluate friction and wear properties of materials under sliding condition in relative motion. Commonly, the tests are performed under various testing standards such as ASTM F732, ASTM G133, and ASTM G99. While testing was performed, the normal load is transferred from pin to the contacting surface results in wear mechanism on pin and surface of tested specimen. The temperature, wear and friction force are continuously monitored during the test which can be convert to the tribological properties such as Friction coefficient (COF), wear rate, and wear resistance.

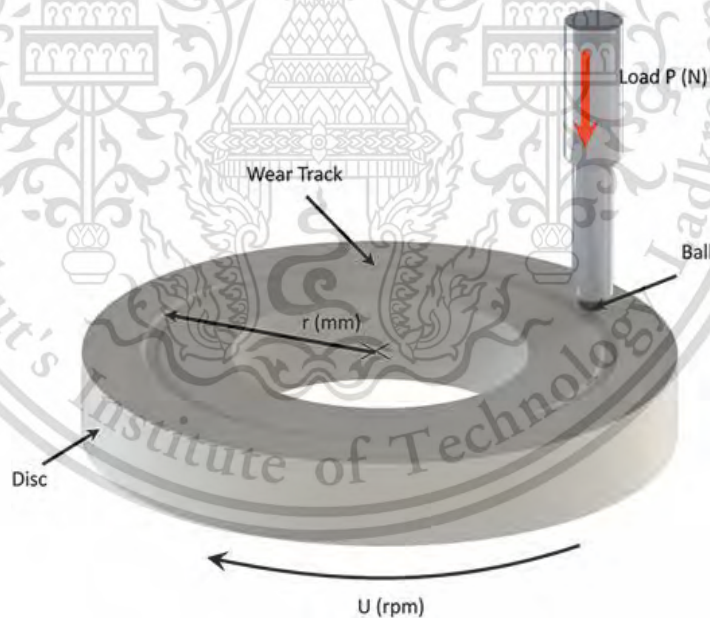


Figure 2.24 The schematic of pin on disc wear tester.

2.7.2. The friction coefficient

The friction coefficient (μ) obtained from the wear test, which indicate the ratio of the friction force and the normal applied load between two counterpart specimens. The equation 2.2 express the friction coefficient equation, where f defined as friction force and F_{load} defined as normal applied load. Figure 2.25 present the typical curve of friction coefficient and time [18]. It shows two sections of COF, the transition section and the steady state section. The transition section is attributed to the run-in state. During the run-in state, some chemical reactions occur, and the surface roughness changes until the system comes to a steady state. The second section is call as steady state because the friction coefficient in this state is already stable. The steady state may either decrease or increase from the run-in state, depend on the types of material contact and parameters of contact pairs.

$$\text{Friction Coefficient } (\mu) = f / F_{load} \quad (2.1)$$

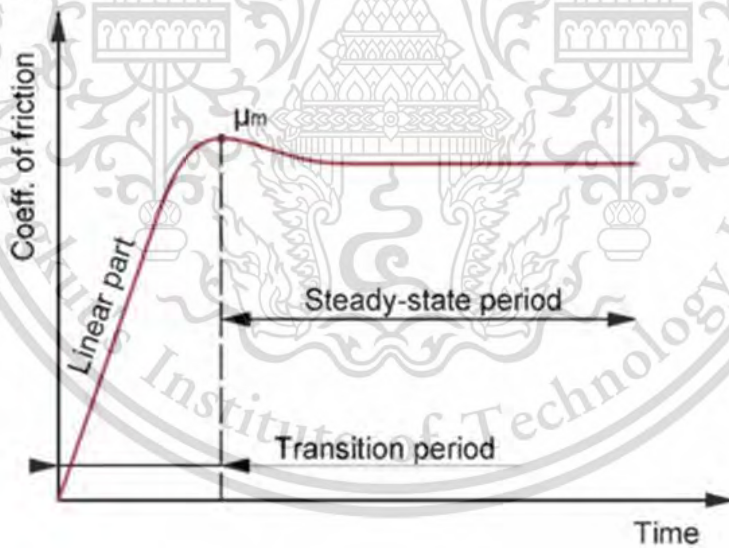


Figure 2.25 The typical curve of friction coefficient and time.

2.7.3. Wear rate

Wear rate can describe the material removal per unit sliding distance or time by reflecting mass loss, volume loss or linear dimension change. The common unit of wear rate is m^3/m or mm^3/mm .

2.7.4. Mass loss

Mass loss is a mass difference between initial mass and final mass which cause from wear. Mass loss obtained by precision digital balance measurement, which is the convenient method for wear measurement, especially when the worn surface is irregular shape. Before the weight measurement, the specimen must be carefully cleaned. The common unit of mass loss is gram (g) and milligram (mg).

2.7.5. Volume loss

Volume loss is one of factor that can describe the wear behavior. Normally, volume loss calculated from length and width of wear scar track, or scar profile according to the geometry of the wear track. The measurement of length and width of wear scar track can be performed by a microscope. The common unit of volume loss is mm^3 , mm^3/m , mm^3/N , and $\text{mm}^3/\text{N.m}$. Volume loss enables a better comparison of wear among materials having different densities. However, this method is inappropriate for a irregular wear track.

2.8. Wear mechanism

Wear mechanism is the removal of solid material from surface and/or subsurface when two solid surfaces are in the tribological contact due to the moving components. Tribological contact are influenced by many properties and environment such as hardness, surface of materials, surface roughness, normal load, type of motion, humidity, temperature, and lubricant properties. The wear mechanism can characterize as severe and mild wear. The worn surfaces with smooth and small wear debris size not over about $1\mu\text{m}$ is characterize as mild wear. On the other hand, the roughened worn surface with a large wear debris size which can be observed by naked eye can defines as severe wear. The large amount of wear results in low life service time of the components. Thus, the

components life cycle time can be developed by mainly in two ways which is applying a lubricant and surface modification [9]. The important wear mechanisms can be categorized into adhesive wear, abrasive wear, delamination wear, and corrosive wear. Table 2.2 presents the overall of possible wear scenarios [19].

Table 2.2 Relative importance of the forms of wear

Type of Wear	Eyre (1976)	Rabinowicz (1983)
Adhesive Wear	23%	45%
Abrasive Wear	58%	36%
Corrosive Wear	5%	4%
Surface Fatigue Wear	14%	15%

2.8.1. Adhesive wear

Adhesive wear is occurred from shearing of adhesive bond (cold welds) of asperities lead to transferring of material from one surface to another surface as Figure 2.26. The cold welded of asperities is resulted from plastically deformed and welded under high temperature and load in relative motion. When considerate at the contact points, the cohesive bond of the weaker material is weaker than the adhesive bond of welded asperities.

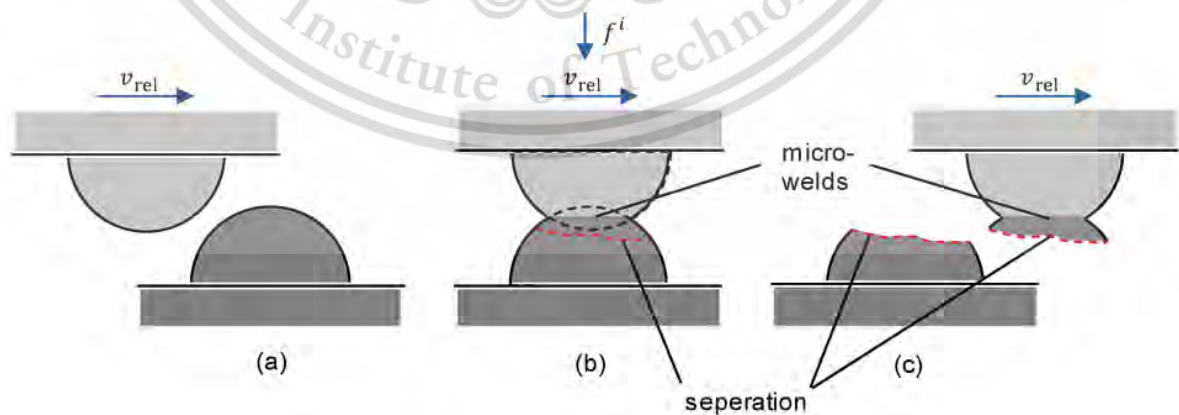


Figure 2.26 Schematic of adhesive wear mechanism.

2.8.2. Abrasive wear

Abrasive wear is damaging of surface by plastic deformation or fracture which occur from asperities of a rough, hard particles or hard surfaces sliding along a softer solid surface. The character of damaging is wedging, cutting, and ploughing phenomena. The ploughing is a groove on surface of material. Abrasive wear can categorize by mainly in two modes of wear that is two body abrasive wear and three body abrasive wear. Figure 2.27 show the schematic diagram of two body abrasive wear which is a simple form of abrasion. Its cause from the difference of degree of surface roughness and hardness of two solid rubbing surfaces. Hard abrasive particles are form by fracture and severe abrasion. However, it can be improved by reducing of surface roughness and applying lubrication. Figure 2.28 show the schematic diagram of three body abrasive wear. The abrasive particles between contact area are slide and roll on the surface, which results in cutting wear [20] and localized plastic deformation in relative motion of the contact surface [21]. The detailed of mechanism also depends on the particle size and the gap between the two main bodies [22]–[24].

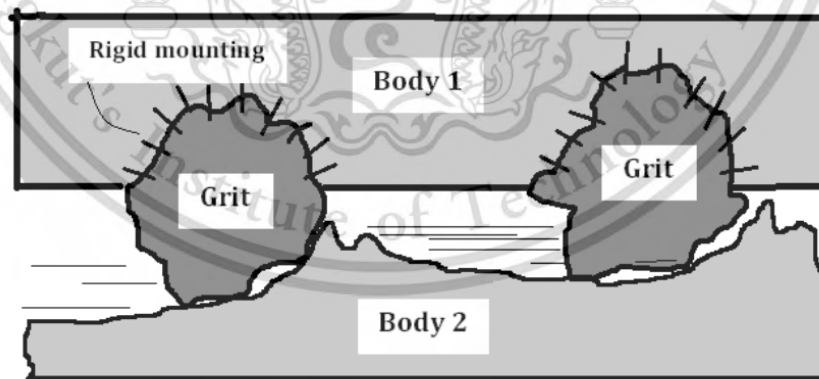


Figure 2.27 Schematic of two body abrasive wear mechanism.

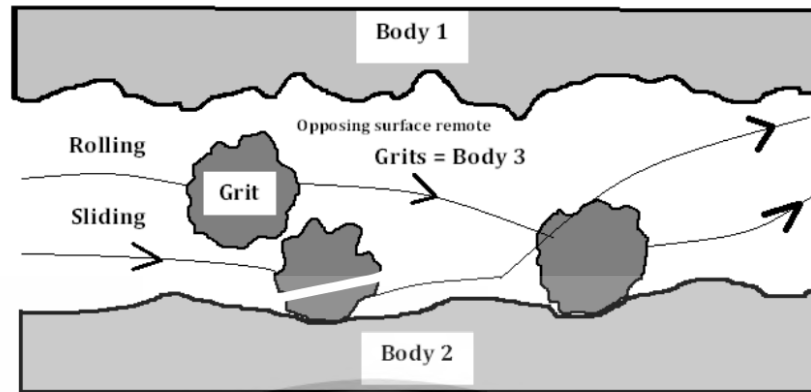


Figure 2.28 Schematic of three body abrasive wear mechanism.

2.8.3. Fatigue/ Delamination wear

Delamination wear is caused by fatigue from cyclic loading. During the cyclic loading, some crack is present on surface or subsurface. Then, the surface cracks propagate and connect together with other cracks. Results in generate of wear particles in flake- like sheets and pits or voids formation on contacting surface. The propagation of crack can be influence by the relative humidity in the air, in the high moisture atmosphere, the crack propagate occurs rapidly when compare with dry atmosphere [9], [25]. Figure 2.29 and figure 2.30 present the SEM micrograph of severe delamination wear and mild delamination wear, respectively.

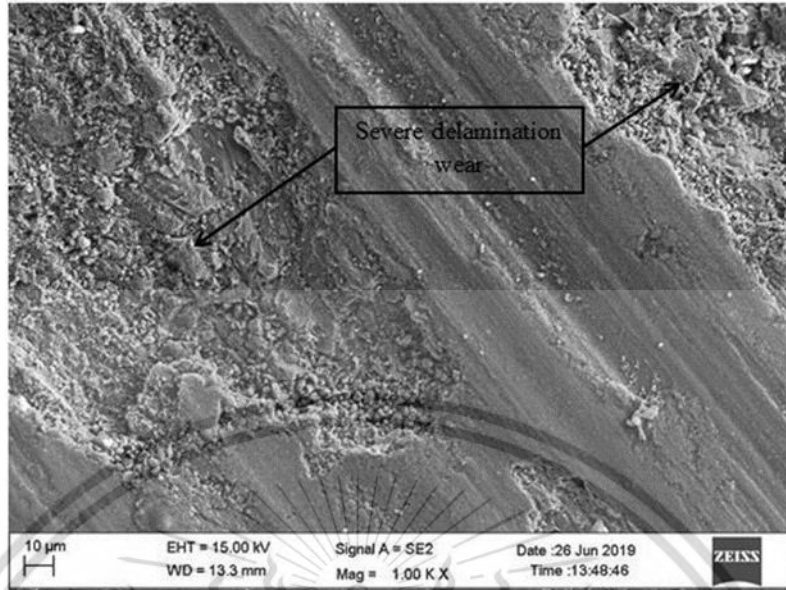


Figure 2.29 SEM micrograph of severe delamination wear.

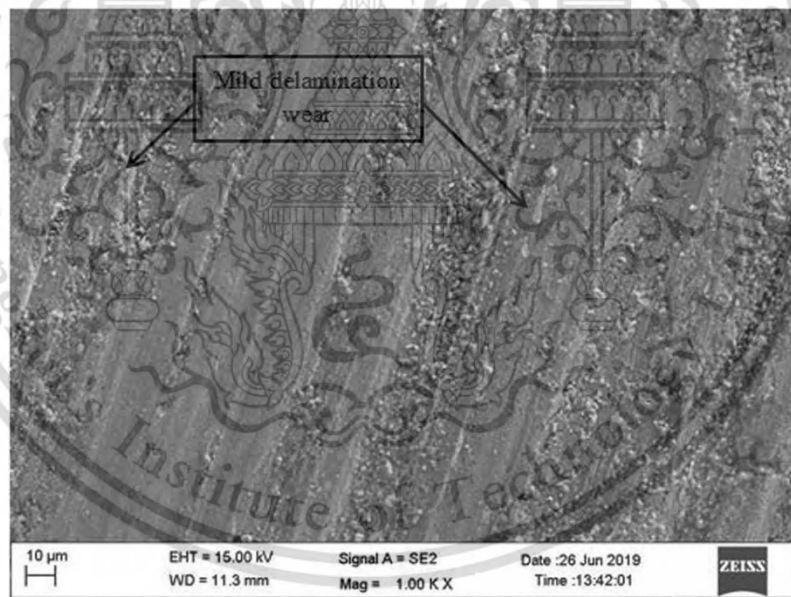


Figure 2.30 SEM micrograph of mild delamination wear.

2.8.4. Corrosive/ Oxidative wear

Corrosive or oxidative wear can occur when the oxygen or other gases have a reaction on the sliding surfaces results in intense damage and material losses. Sometimes oxidative wear can generate by the antiwear or other chemical additives because of the presence of the dissolved oxygen. The oxidation rate at the beginning is fast because of place exchange mechanism and the oxide film grows quickly on the relative surface. When the oxide film thickness on the surface reaches about 2-3 nm, the oxidation rate on the surface decrease and the oxide film continues form by oxygen diffuse into the metal [9], [26]. Figure 2.31 and figure 2.32 present the schematic of oxidative wear mechanism [27] and SEM micrograph of oxidative wear.

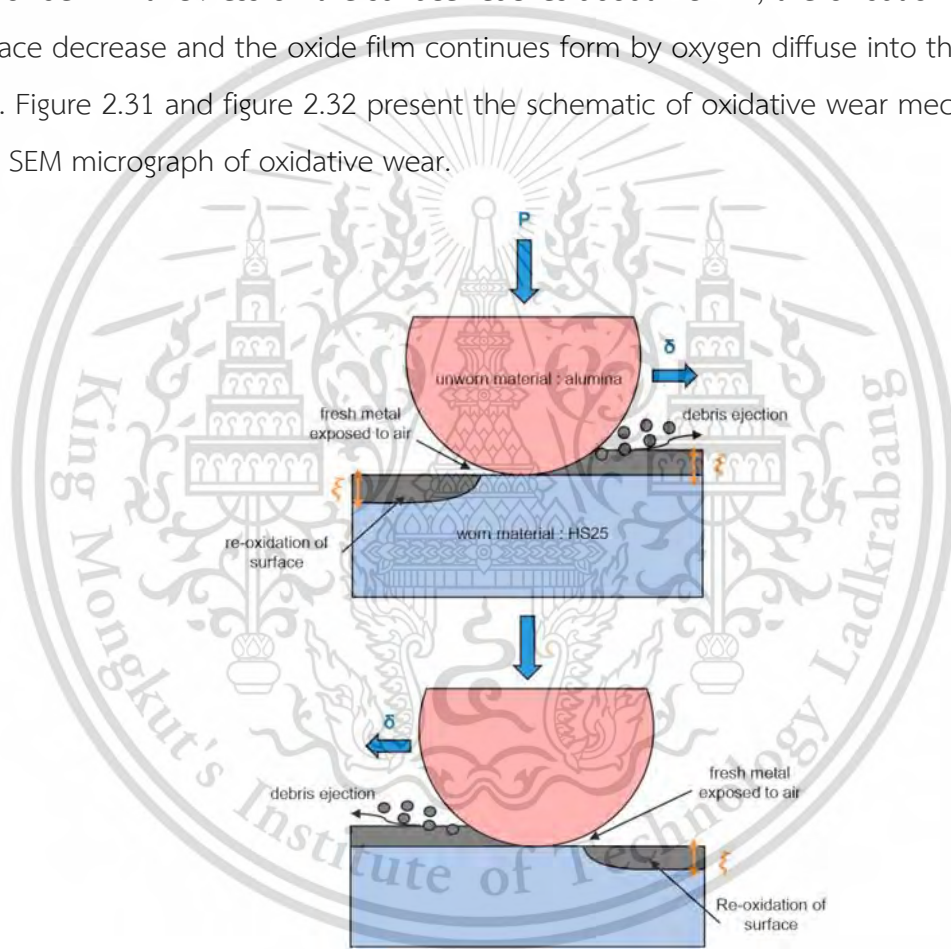


Figure 2.31 Schematic of oxidative wear mechanism.

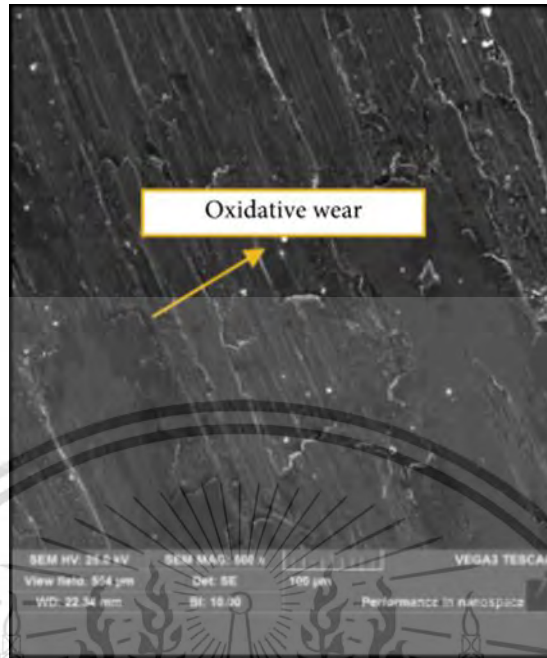


Figure 2.32 SEM micrograph of oxidative wear.



CHAPTER 3

RESEARCH METHODOLOGY

3.1. Materials

3.1.1. Iron base particle powder

Iron base particle powder (MH80.23), shown in Figure 3.1, is a water atomised powders or sponge iron powders available from Höganäs AB, Sweden, having an apparent density of about 2.30 g/cm³ and a particle size substantially below 150 µm, the amount of particles smaller than 45 µm is about 3%. Specially designed to match the requirements for self-lubricating bearings. And it can also be added to powder mixes in small quantities to substantially improve green strength.



Figure 3.1 Iron base particle powder

3.1.2. Pre-alloyed Fe-Mo-Mn powders

Sintered Fe-Mo-Mn-Si-C composites were prepared from 3 different pre-alloyed Fe-Mo-Mn powders as in Figure 3.2, Fe-0.50Mo-0.15Mn, Fe-0.85Mo0.15Mn and Fe-1.50Mo-0.15Mn, namely ATOMET 4001, ATOMET 4401 and ATOMET 4901. These pre-alloyed Fe-Mo-Mn powders is design for a highly compressible, water-atomized alloy steel designed for use in high strength, high performance powder metallurgy and sinter hardening applications.



Figure 3.2 Pre-alloyed Fe-Mo-Mn powders

3.1.3. Silicon carbide

Figure 3.3 show the silicon carbide powder (SiC) which commonly employed as the reinforcing phase in Fe-based alloys owing to its high strength and chemical stability, especially in harsh environments. Moreover, it used to reduce fiction coefficient and mechanical interactions between surfaces in relative motion. Figure 3.4 show the SiC powder in SEM which supplied by AALDARICH. Its physical properties have average particle size lower than 40 μm (as received).



Figure 3.3 SiC powder.

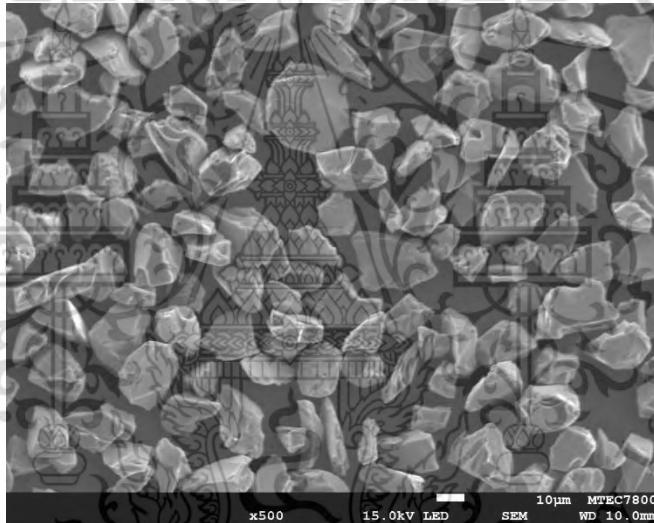


Figure 3.4 SiC powder in SEM.

3.1.4. Zinc stearate

Zinc stearate is added as a lubricant or binding agent during mixing of iron powder or other metallic based composites before compaction for enhances blending properties and improve flow with powdered metal and imparts consistent porosity for fabrication of self-lubricating components. In addition, it prevents the parts from adhering to the mold in compaction process and leaving a better finish. The Figure 3.5 show the zinc stearate powder.

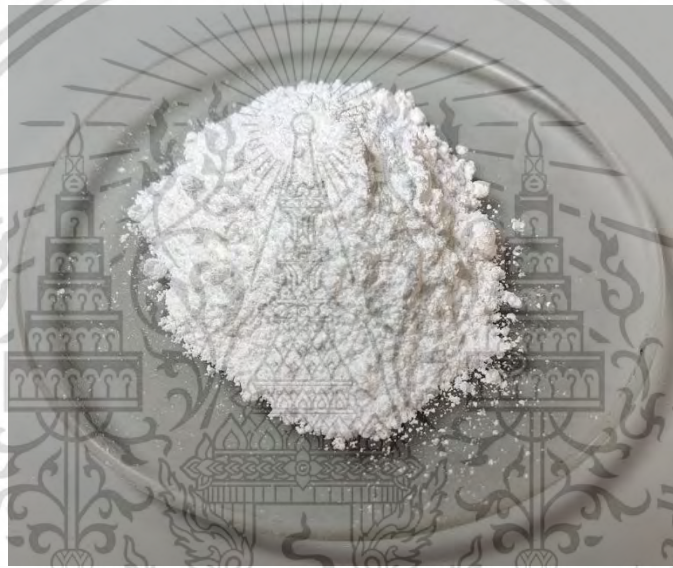


Figure 3.5 Zinc stearate powder

3.1.5. Argon gas

Argon gas, show in Figure 3.6, were used to prevent chemical oxidation on the surface of sintered parts. Because Argon gas can remove oxygen from air before and after sintering process.



Figure 3.6 Argon gas cylinders.

3.1.6. Nital etchant

Nital etchant as Figure 3.7 is a mixture of nitric acid and alcohol commonly used for etching low carbon steels to reveal the microstructure of the metal through selective chemical attack. Etchants will preferentially attack high energy sites, such as boundaries and defects.

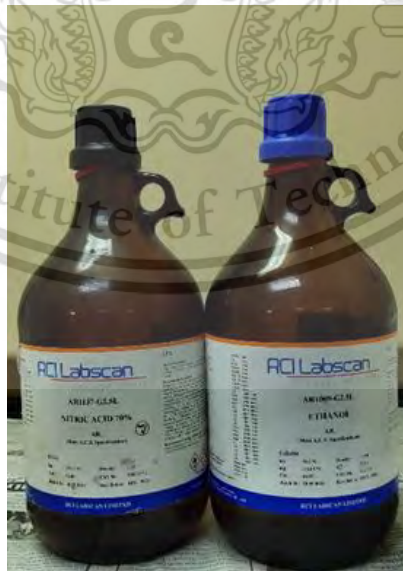


Figure 3.7 Nital etchant

3.2. Experimental Equipment

3.2.1. Digital balance

Laboratory Digital balance 3-digit is used for Lab weighing and density calculation. It defined by high levels of accuracy and precision in analytical testing. Figure 3.8 show the Digital balance (3-digit).



Figure 3.8 The Digital balance (3-digit).

3.2.2. Analytical balance

Analytical Digital balance 4-digit is used for Lab Weighing and wear analysis. It defined by high levels of precision, strong environmental adaptability and readability at 0.0001g. Figure 3.9 show the Analytical balance.



Figure 3.9 The Analytical balance (4-digit)

3.2.3. Powder blender

Powder blender as show in Figure 3.10 is uses for mixing of the metal and additive powders in different area type together, operate using a rotating powder bottle at desired revolution per minute.

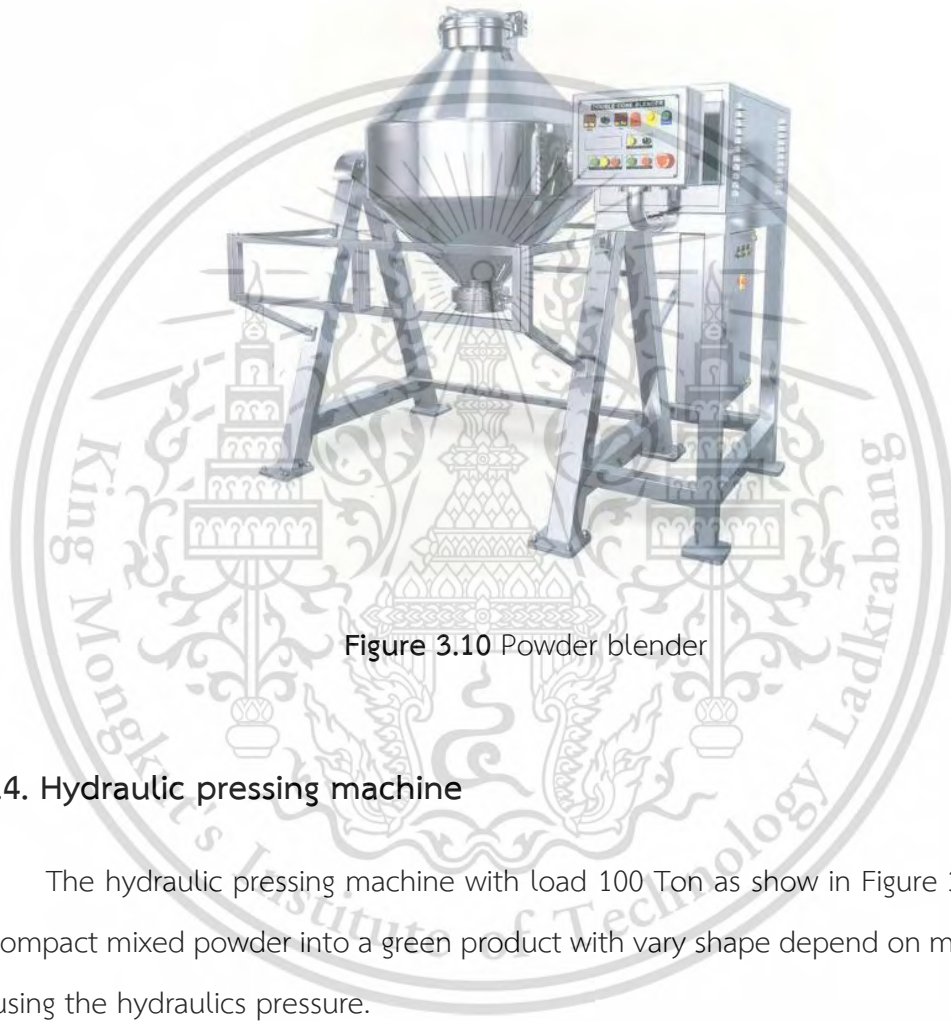


Figure 3.10 Powder blender

3.2.4. Hydraulic pressing machine

The hydraulic pressing machine with load 100 Ton as show in Figure 3.11 is used to compact mixed powder into a green product with vary shape depend on mold and die by using the hydraulics pressure.



Figure 3.11 Hydraulic pressing machine

3.2.5. High vacuum sintering furnace

High vacuum sintering furnace offered by SCHMETZ D59708 MENDEN as show in Figure 3.12 is used for sintering the specimens under the vacuum atmosphere. After the sintering process, it becomes the density material. The sintering process directly affects the grain size, pore size and grain boundary shape and distribution in the microstructure, thus affecting the properties of the material.

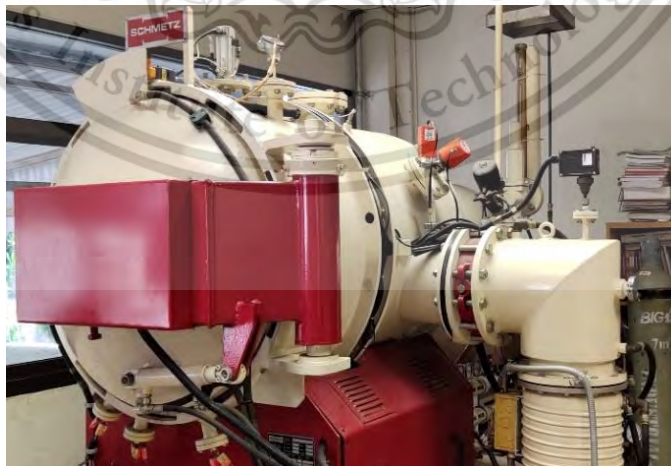


Figure 3.12 High vacuum sintering furnace SCHMETZ D59708 MENDEN

3.2.6. High precision cutting machine.

High precision cutting machine which is Discotom-5 cut off machine as Figure 3.13 is used to cut materials into specific shapes to prepare specimen for microstructure characterization.



Figure 3.13 High precision cutting machine.

3.2.7. Hot mounting press

Hot mounting press as Figure 3.14 is used to prepare the sample to be grinded and polished. The aim of mounting is to handle small or odd shaped specimens and to protect fragile materials, thin layers or coating during preparation as well as to provide good edge retention. In hot mounting, the specimen is mounted under heat and pressure with a hot mounting press.



Figure 3.14 Hot mounting press

3.2.8. Metallographic grinding/polishing machine

The metallographic grinding/polishing machine used in this work was Labopol-5, as shown in Figure 3.15. It was used for both grinding and polishing processes. is a Metallurgical Grinding Polishing Machine which used for sample preparation process by grinding and polishing with high reliability of rotational speed, the ultimate goal being to produce a no deformation, no scratch and highly reflective sample surface.



Figure 3.15 Metallographic grinding/polishing machine.

3.2.9. Silicon Carbide paper

Silicon carbide paper (SiC paper) grit sizes of 120, 180, 240, 400, 600, 800, 1000, and 4000 as shown in Figure 3.16 are used for grinding metallic specimens to remove surface roughness and achieve a flat, smooth, and scratch-free surface before being polished in the next step of metallography specimen preparation.

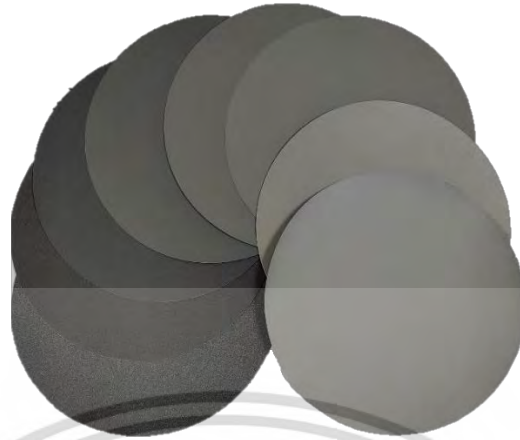


Figure 3.16 Silicon carbide paper.

3.2.10. Polishing cloth

Micron polishing cloth as Figure 3.17 is use after grinding step to remove the scratches produced from the finest grinding stage. The polishing step in specimen preparation removes the last thin layer of the deformed metal for a smooth reflective surface.



Figure 3.17 Micron polishing cloth.

3.2.11. Diamond suspension size 6, 3 and 1 μm

Diamond suspension size 6, 3 and 1 μm as Figure 3.18 is use with polishing cloth during the sample preparation stages for fast stock removal and to produce a perfect polished surface ready for analysis. The diamond suspension type to use is depends on the material and the surface finish required.

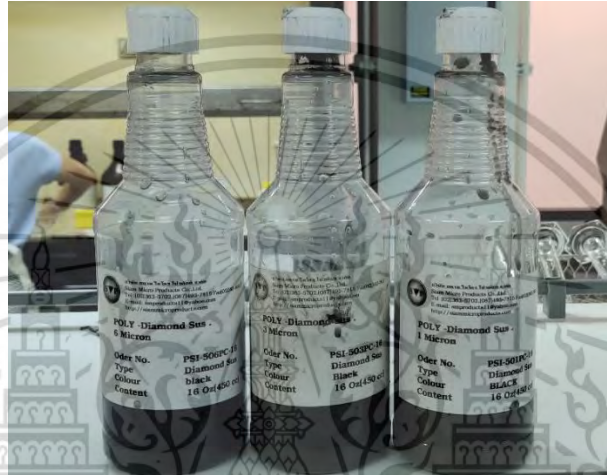


Figure 3.18 Diamond suspension size 6, 3 and 1 μm

3.3. Characterization instruments

3.3.1. Digital vernier

Digital vernier as Figure 3.19 is a precision instrument to measure the internal and external dimensions of an object by displays the reading as a numeric value.



Figure 3.19 Digital vernier

3.3.2. Macro hardness testing machine

Macro hardness testing machine offered by Instron-930 is show in Figure 3.20 which is an equipment for measuring the hardness of the macro structure by conventional Rockwell hardness testing with high precision tester and quick results. In the Rockwell test, results are rapidly and directly obtained without the need for a secondary, dimensional measurement requirement.



Figure 3.20 Instron-930 Macro hardness testing machine

3.3.3. Universal testing machine (Instron 8801)

A Universal Testing Machine by Instron 8801 Universal Instrument, show in Figure 3.21, is used to test the tensile strength of materials in this research. This testing equipment can evaluate materials properties such as tensile strength, elasticity, yield strength, elastic and plastic deformation, and strain hardening.



Figure 3.21 Instron 8801 Universal Instrument

3.3.4. Optical Microscope

Optical Microscope (OM) by Olympus STM7, Japan, show in Figure 3.22, is a type of microscope that uses visible light and a system of lenses to magnify images of small samples such as microstructure of specimens in this research. Optical microscopes were easy to develop and are popular because they use visible light, so samples directly observed by the eye.

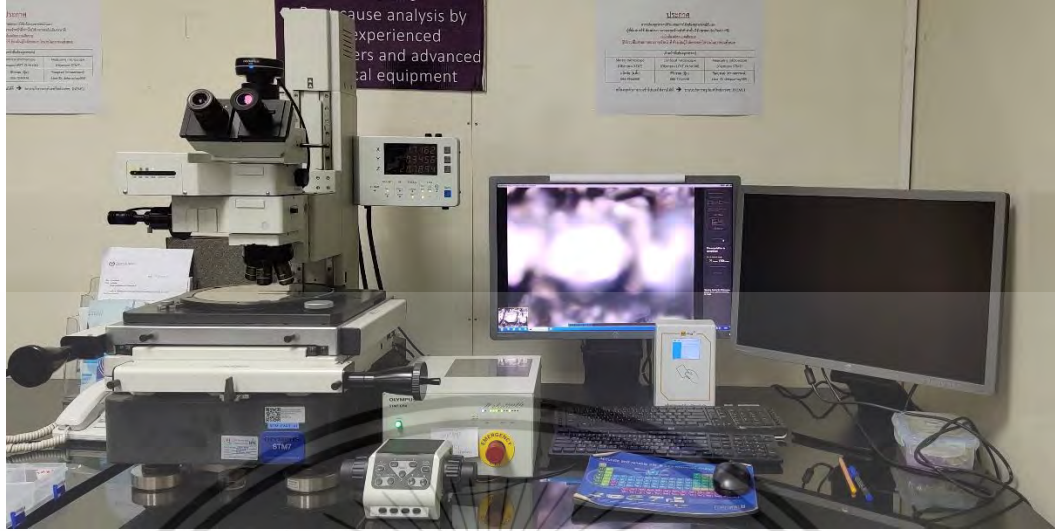


Figure 3.22 Optical microscope by Olympus STM7, Japan

3.3.5. Scanning electron microscope

The scanning electron microscope (SEM) used in this work was Hitachi SU8230, Japan, as shown in Figure 3.23, is used to investigate microstructure of specimens, the worn surface, wear debris and counter ball surface in micro scale. SEM scans a focused electron beam over a surface to create an image. The electrons in the beam interact with the sample, then they produce secondary electrons, backscattered electrons, and characteristic X-rays. These signals are collected by one or more detectors to form images which are then displayed on the computer screen.



Figure 3.23 Scanning electron microscope by Hitachi SU8230, Japan

3.3.6. X-Ray Diffraction Analysis

X-Ray Diffraction Analysis (XRD), show in Figure 3.24., is used to Identify crystalline phases and orientation present in a material and thereby reveal chemical composition information. Identification of phases is achieved by comparison of the acquired data to that in reference databases.



Figure 3.24 X-Ray Diffraction Analysis

3.3.7. Pin-on-disc testing machine

Pin-on-disc testing machine is carried out according to ASTM G99, show in Figure 3.25, is used to evaluate friction and wear characteristics in sliding contacts. Sliding occurs between a rotating disc and a stationary pin. Wear track diameter and normal load can be varied. Electronic sensors are used for monitoring tangential frictional force and wear.



Figure 3.25 Pin-on-disc testing machine (ASTM G99)

3.4 Experimental procedure

3.4.1. Powder mixing

Sintered 000Mo composite was prepared as the reference material from pure Fe powder mixed with 4 wt. % silicon carbide (SiC) powder. Other experimental sintered composites were prepared from 3 different pre-alloyed Fe-Mo-Mn powders, such as Fe-0.50Mo-0.15Mn, Fe-0.85Mo-0.15Mn, and Fe-1.50Mo-0.15Mn, mixed with 4 wt. % SiC powder. The powder mixtures were added with 1 wt.% zinc stearate and blended in a powder mixer with speed 6.5 rpm for 1 hour. The nominal compositions of experimental sintered composites are given in Table 3.1.

Table 3.1 The nominal compositions of experimental sintered composites

Composite	Metal powder	SiC (wt. %)	Nominal composition (wt. %)				
			C	Si	Mo	Mn	Fe
000Mo	Fe	4.0	1.20	2.80	0.00	0.00	Bal.
050Mo	Fe-0.5Mo-0.15Mn	4.0	1.20	2.80	0.48	0.14	Bal.
085Mo	Fe-0.85Mo-0.15Mn	4.0	1.20	2.80	0.82	0.14	Bal.
150Mo	Fe-1.5Mo-0.15Mn	4.0	1.20	2.80	1.44	0.14	Bal.

3.4.2. Compaction

Standard tensile test bars, conforming to the MPIF standard 10 and as given in Figure 3.26, were prepared from mixed powders by using 100-ton hydraulic pressing machine. Densities of compacted or green specimens were measured according to MPIF standard 42. The green densities were controlled to be $6.50 \pm 0.01 \text{ g/cm}^3$. The coin-shape specimens or disks for tribological testing were prepared to have the same green density of $6.50 \pm 0.01 \text{ g/cm}^3$. The disk dimensions are shown in Figure 3.27. To reduce the spring back effect, each compacted specimen was kept in a die under a compacting pressure for 10 seconds before being ejected out of the die.

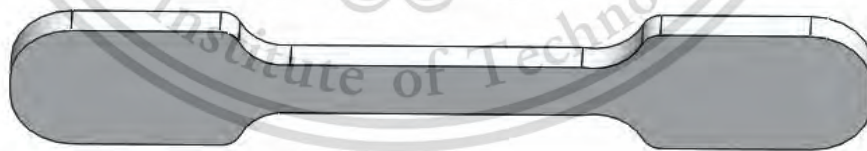


Figure 3.26 The sketch of standard tensile test bar.

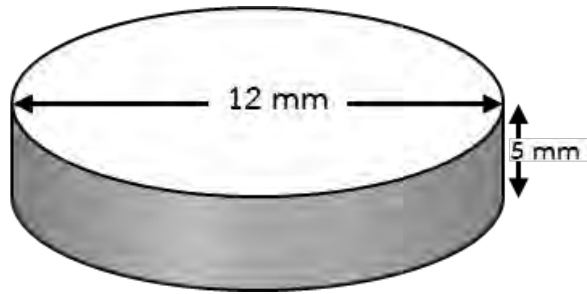


Figure 3.27 Green disk dimensions.

3.4.3. Sintering

Green compacts of both standard tensile test bars and disk specimens were sintered in a high vacuum sintering furnace, which provided both high temperature and reducing atmosphere. Sintering was performed in three stages as shown in Figure 3.28 under high-vacuum atmosphere. In the first stage of sintering, green specimens were heated up to 600 °C, the de-waxing temperature, which was held for 60 minutes to remove all organic materials out of green specimens. In the second stage, brown specimens were heated up to 1250 °C, the sintering temperature, which was held for 45 minutes to facilitate the interactions between Fe/Fe-Mo-Mn metal and SiC powder particles and the sintering between matrix powder particles. In the last step, sintered specimens were slowly cooled in the sintering furnace (with cooling rate of 0.1 °C/s). Under this slow and continuous cooling, relevant transformations from high-temperature to low-temperature phases would occur and result in microstructural development. The phase transformation products were identified or characterized later by using microstructural and X-ray diffraction (XRD) analyses.

Densities of sintered specimens were measured according to MPIF standard 42.

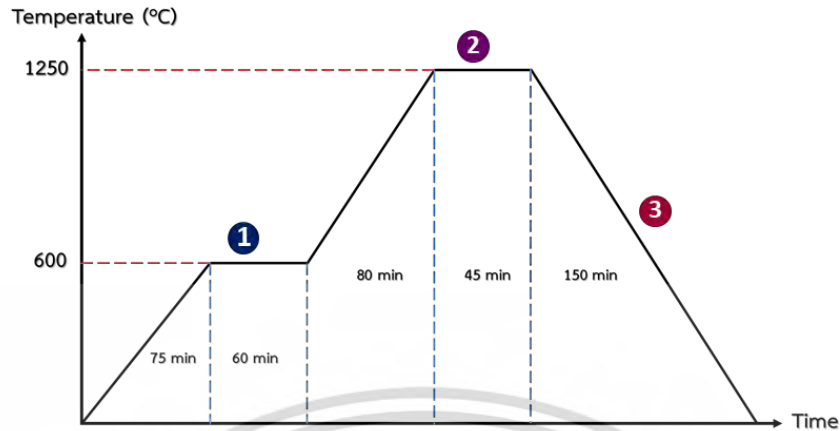


Figure 3.28 The sintering profile.

3.4.4. Mechanical test

1. Hardness test

For macro-hardness, three tensile test bars of each sintered composite were used for Rockwell hardness testing, conforming to ASTM E-18, using ball indenter with diameter of 1/4 inch and Rockwell scale B (HRB). The mean hardness value defines by averaged value from five different areas on each specimen. This is measurement.

2. Tensile test

Three sintered tensile test bars of each sintered composite were tested by universal testing machine, Instron 8801 (according to ASTM E-8). The test process involves placing the test specimen and slowly extending and eventually fractures occurred.

3. Surface preparation

The surfaces of all specimens were prepared by grinding on silicon carbide papers with grits of P80 to P4000. The ground surfaces were then polished with diamond suspensions with sizes of 6, 3, and 1 μm . The properly polished surfaces were etched by 2% Nital solution, cleaned with ethanol, and dried before being metallographically observed by using optical microscopy (OM) or scanning electron microscopy (SEM).

3.4.5. Wear test

Dry sliding wear experiments were carried out on ball-on-disc wear machine in accordance with ASTM G99-05(2010). The sketch of ball-on-disc wear test and conditions are given in as Figure 3.29. The sliding velocity was 0.1 m/s at normal load 5N, 10N and 15N. All specimens were tested under sliding distance of 1,000 m at room temperature with relative humidity 60%. The specimens for dry sliding test had disk shape with roughness of 4-5 μm . The ball, as a counterpart material, was made of SKF chromium steel grade G20 with diameter of 6 mm, hardness of 838 ± 21 HV, and roughness of 4 μm . The friction coefficient, obtained by programmatical converting the friction torque measured by using a load cell into coefficient, was recorded continuously. The mass loss was obtained from specimen mass difference before and after wear test. The volume loss of disk specimens was calculated according to Equation 3.1., where R was defined as wear track radius, and d defined as wear track width. The volume loss of a spherical ended pins was calculated according to Equation 3.2., where d was defined as wear scar diameter, and r defined as pin end radius. At the end of each test, the wear rate was calculated according to Equation 3.3. Worn surfaces and wear debris were investigated by using SEM to better understand the wear mechanism and the influences of material characteristics on wear behavior.

$$\text{Disk volume loss} = 2\pi R [r^2 \sin^{-1}(d/2r) - (d/4)(4r^2 - d^2)^{1/2}] \quad (\text{Equation 3.1})$$

$$\text{Pin volume loss} = (\pi h/6)[3d^2/4 + h^2] \quad (\text{Equation 3.2})$$

$$\text{Wear rate} = (\text{volume loss}/\text{distance}) \quad (\text{Equation 3.3})$$

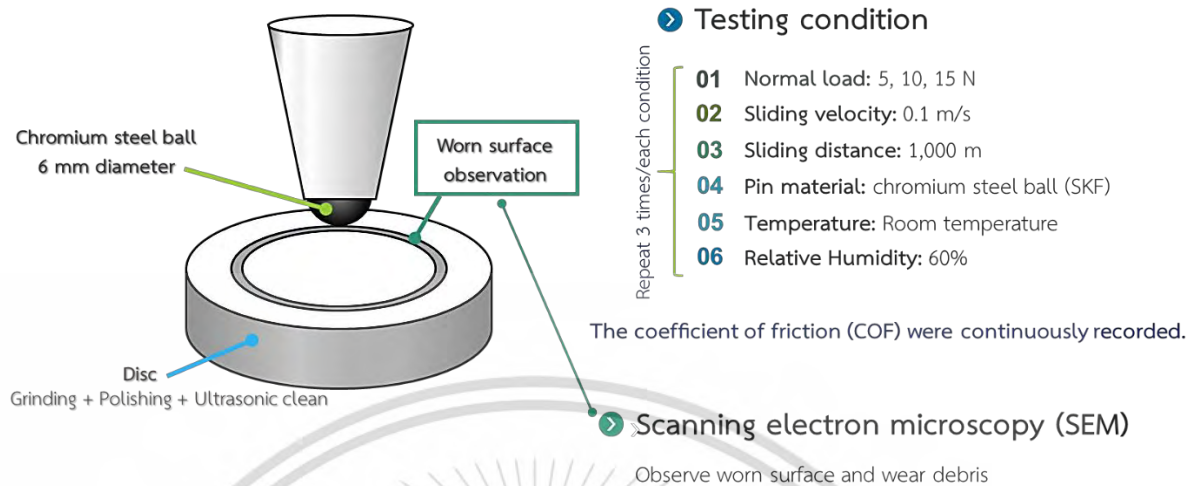


Figure 3.29 The schematic of ball-on-disc wear test set up.

3.4.6. Microstructure Analysis

Optical Microscopy and Scanning Electron Microscopy are equipment to observe the microstructure of specimens. Optical microscopy is a method for general inspection purposes but scanning electron microscopy can provide more topographical and compositional detailed. Thus, this thesis used Optical Microscopy for analyst the overview of microstructure and use Scanning Electron Microscopy for analyst the details of microstructure.

3.4.7. X-Ray Diffraction Analysis

X-Ray Diffraction Analysis (XRD) is equipment used to Identify crystalline phases and orientation present in a material. All specimens for XRD were prepared by cutting, grinding, and polishing and performed by PANalytical X'pert pro with copper source (wavelength of 1.5406 Å) and conditions including step size of 0.2°, time of 0.5 s/step and angle of 30-110°.

CHAPTER 4

RESULTS AND DISCUSSIONS

4.1. Density

In this work, all green specimens in the forms of tensile test bars and disks were produced with green density of 6.5 g/cm^3 . After sintering at $1250 \text{ }^\circ\text{C}$ for 45 minutes, the sintered specimens were cooled slowly in a furnace with cooling rate of about $0.1 \text{ }^\circ\text{C}$. The plot of average sintered density of tensile test bars against sintered composite type is shown in Figure 4.1. The densities of sintered 000Mo, 005Mo, 085Mo and 150Mo composite tensile test bars were 7.07, 7.24, 7.26 and 7.53, respectively. The plot of average sintered density of disks against sintered composite type is shown in Figure 4.2. The densities of sintered 000Mo, 005Mo, 085Mo and 150Mo composite disks were 6.94, 7.27, 7.55 and 7.60, respectively. As indicated by the results, most sintered composite disks showed sintered densities slightly higher than those of sintered composite tensile test bars.

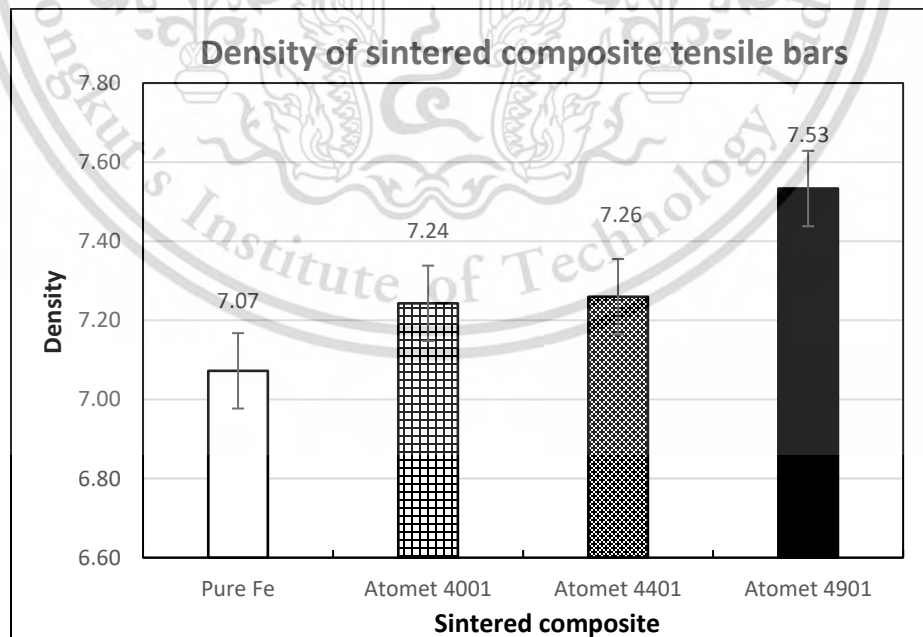


Figure 4.1 The average sintered density of sintered composites tensile test bars.

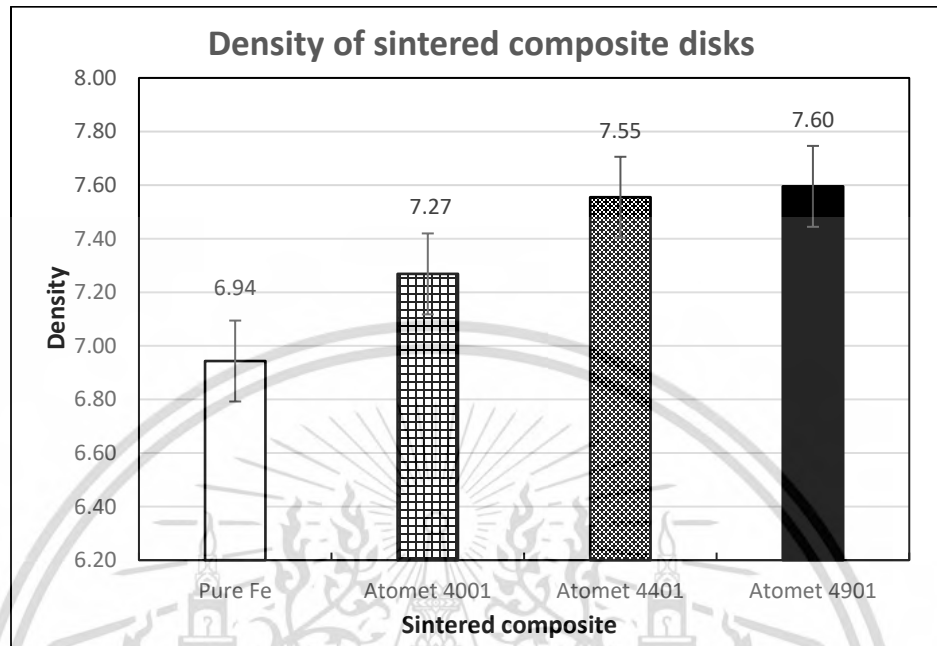


Figure 4.2 The average sintered density of sintered composite disks.

4.2. Fracture surfaces analysis

The fracture surfaces of experimental sintered composite tensile test bars were observed by using SEM as shown in Figure 4.3. The fracture surfaces of sintered 000Mo composite showed 3 different fracture characteristics, such as (1) the coexistence of interparticle ductile dimples and decohesion (Figure 4.3a), (2) cleavage (Figure 4.3b), and crack of a black particle (Figure 4.3a and 4.3b). The presence of interparticle ductile dimples suggests that sintered 000Mo composite undergoes plastic deformation before breakage.

The crack of a black particle, shown in Figure 4.3a, revealed the core/shell nature of such particle. As far the composition was concerned, the solid core was the decomposed SiC residue consisting of Si, C, Fe and Mo constituents, while the shell consisted mainly of carbon [28]. Different characters of black particle cracks were observed on fracture surfaces on sintered composites. In one case, the crack propagated from

matrix/black particle interface through graphite shell, and it was followed by decohesion at solid core/graphite shell interface (Figure 4.3b). The cracks were also found to run through solid cores as shown in Figure 4.3c and 4.3e. In other case, the crack was observed to cut through graphite shell cap (Figure 4.3d).

The fracture surfaces of sintered 050Mo (Figure 4.3c), 085Mo (Figure 4.3d), and 150Mo (Figure 4.3e) composites showed 3 different fracture features, such as typical cleavage, cleavage with high river pattern density, and crack of a black particle. On the fracture surface, a broken black particle was surrounded by typical cleavage, which showed numerous bright crystalline cleavage facets with river pattern strips on the fracture surface. Typical cleavage is characteristic of brittle fracture mechanism [29], [30]. Next to the typical cleavage, the cleavage with high river pattern density was observed. In fact, this type of cleavage was characterized by clusters of planar cleavage facets separated from other clustered facets by ductile tear ridges. The high density of river patterns or cleavage step networks would involve frequent microcrack nucleation and propagation events. This cleavage may be identified as quasi-cleavage [31]. The fracture surfaces of sintered 085Mo (Figure 4.3d) and 150Mo (Figure 4.3e) composites also showed 3 different fracture characteristics, such as cleavage, quasi-cleavage, and crack of a black particle. Accordingly, the SEM results of fracture surfaces of sintered 050Mo, 085Mo and 150Mo composites indicate that the failure of all samples is attributed to brittle mechanism.

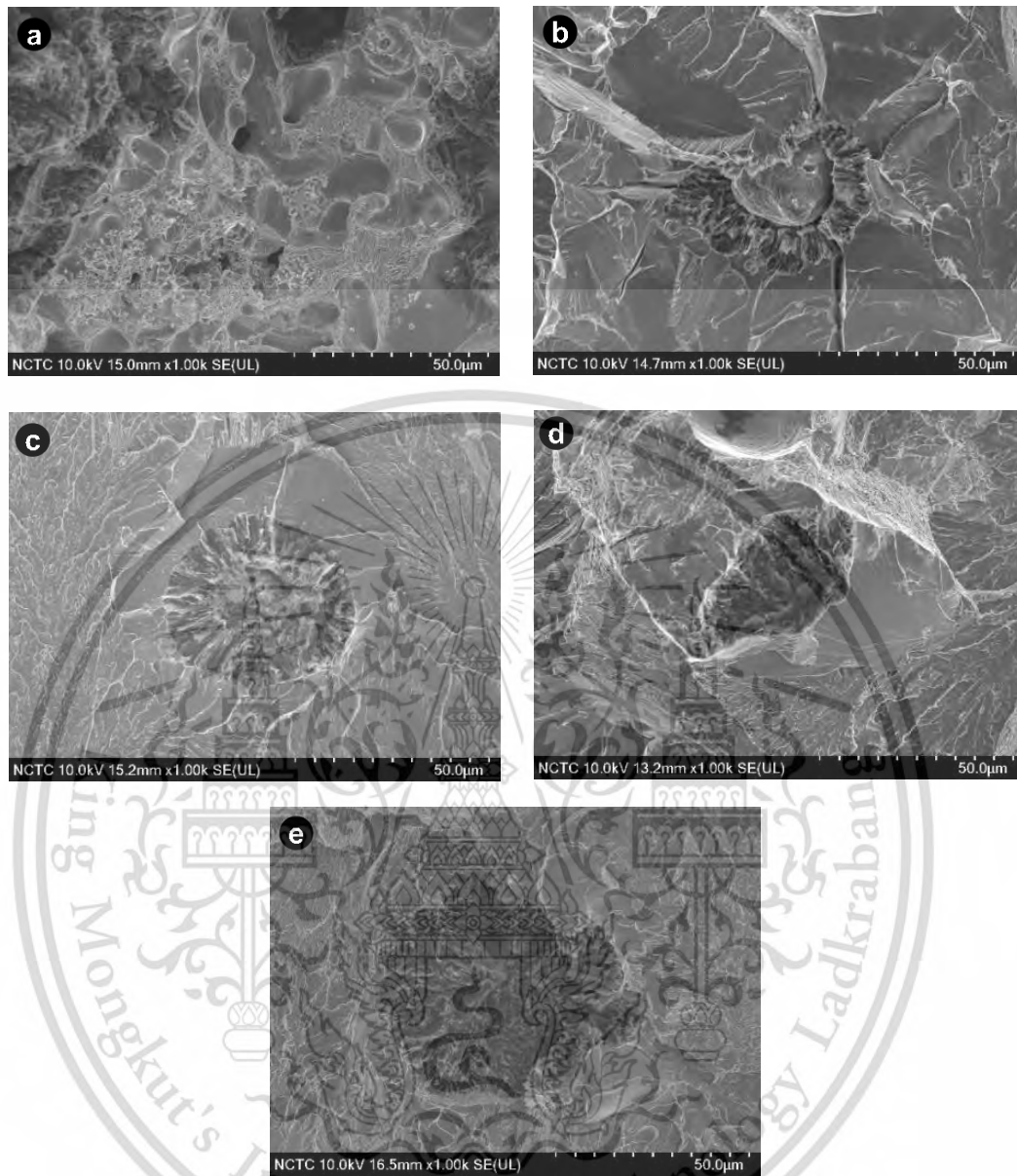


Figure 4.3 SEM fracture micrographs of sintered composites (a, b) sintered 000Mo composite, (c) sintered 050Mo composite, (d) sintered 085Mo composite, (e) sintered 150Mo composite.

EDS analysis was performed on a fractured black particle (Figure 4.4). The whole particle showed red color, which corresponded to carbon element. However, this EDS analysis result does not mean that the whole fractured black particle is a graphite nodule. The presence of carbon all over the fractured black particle is due to the crack nature. The image given in Figure 4.4 displays that the fractured black particle is like a sunflower. According to the image, crack propagates from sintered composite matrix through graphite shells (sunflower petals). When the crack met a graphite shell/solid core interface, it did not cut through but decohesion occurs instead along the interface, resulting information of sunflower seed-like circle.

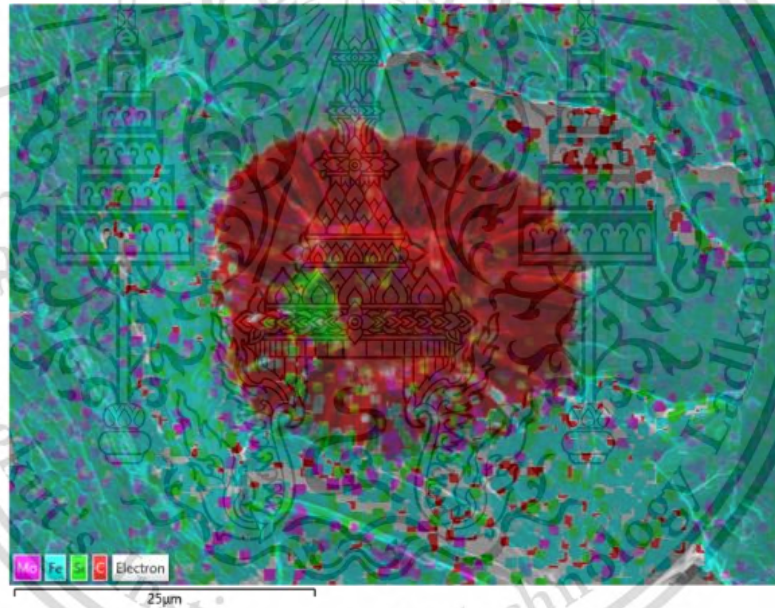


Figure 4.4 EDS mapping of a sintered composite fracture surface.

4.3 Microstructure

4.3.1 OM images

OM images of etched surfaces of sintered composites are shown in Figure 4.5. All sintered composites exhibited a common microstructural feature consisting of a black particle surrounded with light and dark grey areas. The black particles showed different shapes, varied from spherical to irregular shape. The black particle sizes also varied from few to 100 microns. As identified above, the black particles have solid core/graphite shell structure. The white area surrounding a black particle was readily identified as ferrite. Due to ring shape, the light area is commonly known as ferrite halo.

The dark grey areas around ferrite halos could not be resolved in OM images (Figure 4.5). The identification of dark grey areas needs higher resolution microscopy technique. It is shown later in Topic 4.3.2 that SEM images reveal that the dark grey areas contain sole pearlite or pearlite and ausferrite (bainitic ferrite and austenite mixture), depending on sintered composite chemistry. In areas with spherical black particles, the microstructures displayed Bull-eyes structure of a ductile iron (DI) showing halos of ferrite (light contrast) around black particles (dark contrast), the remaining of the matrix being pearlite (dark grey contrast).

The microstructural features as shown in Figure 4.5 resemble those of sintered composites [32]–[36] and of ferritic-pearlitic DIs [37], [38]. The formation of ductile iron-like microstructure was briefly explained in [35]. The conditions, under which ferrite and pearlite transformations occur in DIs, are clearly explained in [39]. Area fractions of microstructural components of sintered composites were measured and presented in Table 4.1. From the table, the fractions of dark grey area, which consists of pearlite and ausferrite and of black particle increased whereas that of ferrite halo decreased with increasing Mo content.

Table 4.1 Fraction of microstructural components in sintered materials

Composite	Area fraction (%)		
	Black particle	Ferrite	Pearlite + Ausferrite
000Mo	3.8	66.2	30.0
050Mo	8.5	36.1	55.4
085Mo	19.0	23.2	57.8
150Mo	19.0	8.5	72.5

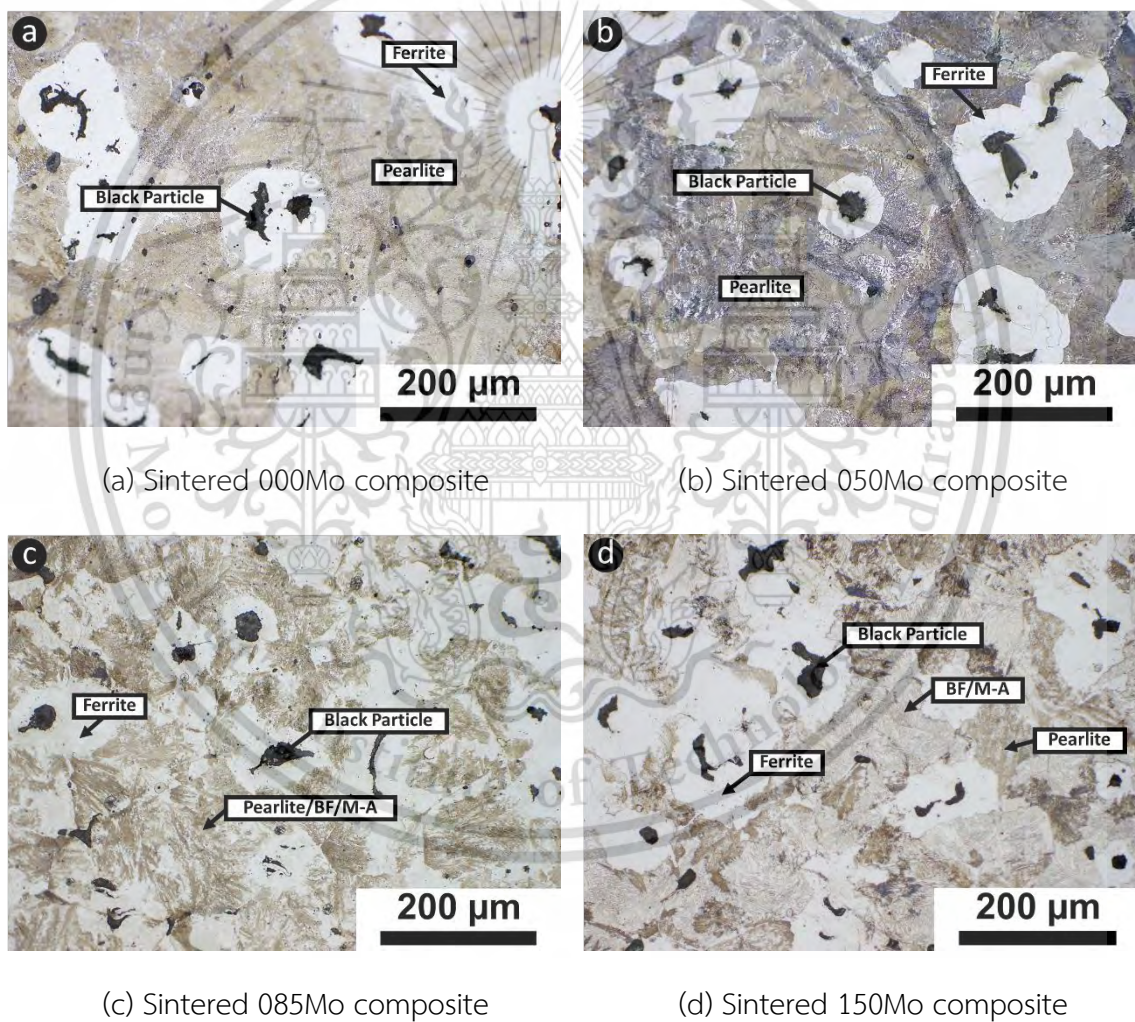
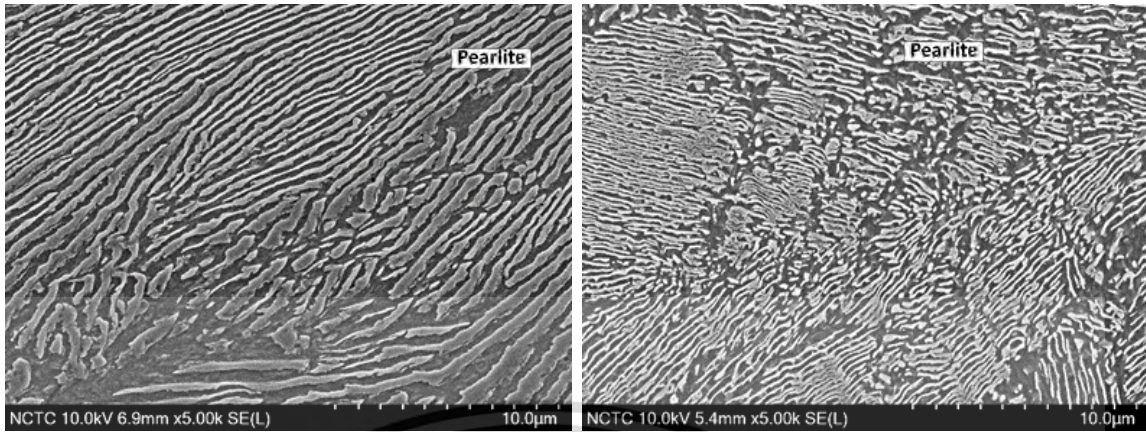


Figure 4.5 OM images of sintered composites.

4.3.2. SEM images

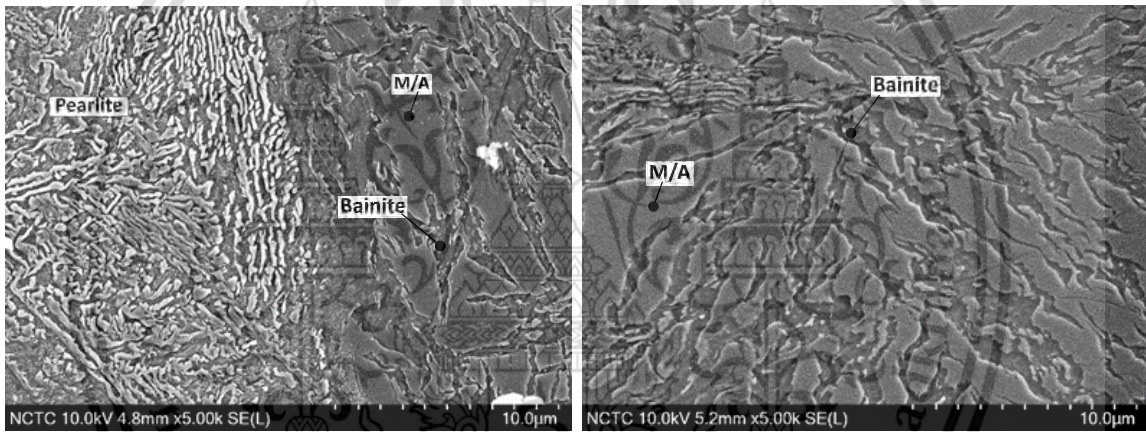
The dark grey areas observed by OM techniques were further investigated by using SEM. The dark grey area SEM images are given in Figure 4.6. It was found that dark grey areas in sintered 000Mo (Figure 4.6a) and 050 (Figure 4.6b) composites contained sole pearlite structure (lamellar consisting of ferrite (dark contrast) and carbide (light contrast)). However, the pearlite of the former composite was clearly coarser than that of the latter composite. Taking the compositions of both sintered composites into account, finer pearlitic structure in the sintered 050Mo composite could be attributed to alloying Mo and Mn elements. According to literatures [40], [41], Mo showed a clear role in refining the pearlite lamellar spacing. For Mn role, fine interlamellar spacing can be tailored by increasing Al content and reducing Mn content for the pearlitic steels [42].

The dark grey areas in sintered 085Mo (Figure 4.6c) and 150Mo (Figure 4.6d) composites contained pearlite and ausferrite. The fraction of ausferrite increased with increasing Mo content. The formation of ausferrite, the common matrix of austempered DI, in both sintered composites is worth discussing here. Since both sintered composites are produced under slow and continuous cooling, phase transformations in these materials should occur in series. OM images given in Figures 4.5c and 4.5d indicate phase transformation series including graphite shell solidification, ferrite transformation, and dark grey area transformation. SEM images given in Figures 4.6c and 4.6d indicate phase transformation series including pearlite transformation and ausferrite transformation. Thus, the whole series include graphite shell solidification, ferrite transformation, pearlite transformation and ausferrite transformation.



(a) Sintered 000Mo composite

(b) Sintered 050Mo composite



(c) Sintered 085Mo composite

(d) Sintered 150Mo composite

Figure 4.6 SEM micrograph of Fe-Mo-Mn-Si-C sintered composites

Mo has a complex effect on phase transformations and precipitation in steels manufactured by conventional casting. On one side, Mo addition up to around 0.5% acts a very powerful pearlite stabilizer and increases strength by refining pearlite [40]. On the other side, Mo addition to some steels results in complete pearlite formation inhibition [43]. The clear examples of Mo influence on ausferrite formation in as-cast irons are given in [44], [45]. The Mo additions of ≥ 1.0 wt. % to Fe-3.2C-1.0Cu-xMo-0.55Mn-2.0Si cast irons resulted in complete pearlite suppression and the whole matrices contained only austenite and bainite (ausferrite). The complete pearlite suppression by Mo addition can be explained, referring to Figure 4.7, by the shift of ferrite and pearlite transformation fields to the right-hand side so the slow and continuous cooling line does not enter the ferrite and pearlite transformation fields. This means the whole austenite matrix is stable until reaching the ausferrite transformation field, in which austenite transforms to ausferrite.

In both sintered 085Mo and 150Mo composites, ferrite halo, pearlite and ausferrite coexist in matrices. To explain the coexistence of these 3 microstructural components, the shift of ferrite and pearlite transformation fields to the right-hand side is still applicable but the degree of shifting must be adjusted to be small, so the slow and continuous cooling line enter the parts of ferrite and pearlite transformation fields. This means that some austenite parts transform to ferrite and pearlite and the retained austenite to ausferrite at the last step.

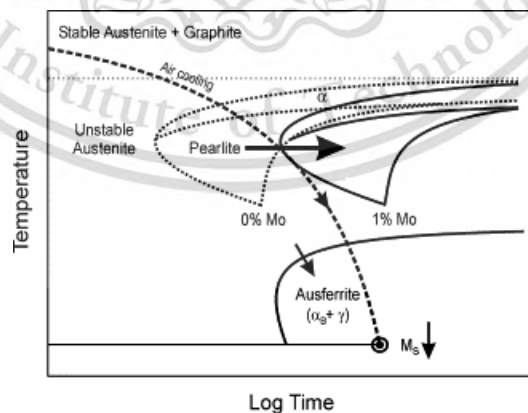


Figure 4.7 Schematic showing the effect of Mo addition on ausferrite formation promotion but pearlite formation suppression [44], [45]

The existence of ausferrite in both sintered 085Mo and 150Mo composites at room temperature is due to stability of austenite component of ausferrite. The austenite stability depends on following factors. The first involves carbon enrichment in austenite. In ausferrite transformation, the formation of bainitic ferrite platelets is associated with carbon diffusion from ferrite to enrich austenite to the extent that it can become thermally stable to well below room temperature [46].

The second involves the addition of judicious Si content. It is well-known that silicon retards the precipitation of cementite from different parent materials or phases, such as cast irons, martensite, and austenite [47]. This is due the fact that silicon has low solubility in cementite (Fe_3C), i.e., up to 4.5 at. % Si [48]. Theoretical study suggests that the formation of $(\text{FeSi})_3\text{C}$ carbide is associated with high formation energy [49], which is not thermodynamically favored.]. This results in carbon-enriched austenite.

The third involves Mo influence on slowing down the decomposition of austenite in ausferrite to ferrite and carbide mixture, known as Stage II reaction of austempering process. It was demonstrated that 0.5 wt. % Mo addition extended the process window or the period of Stage I reaction or the transformation from austenite into bainitic ferrite and austenite components by slowing down Stage II reaction [50].

4.4. XRD analysis

The X-ray diffraction patterns of sintered Fe-Si-C composite and sintered Fe-Mo-Mn-SiC composites are shown in Figure 4.8. The XRD patterns of all sintered composites show peaks corresponding to body-centered cubic (bcc) crystal structure of α -ferrite and orthorhombic crystal structure of M_3C carbide. The XRD identification of α -ferrite and M_3C carbide confirms the existence of lamellar pearlite structure in all sintered composites.

Weak XRD peaks corresponding to face-centered cubic (fcc) crystal structure of M_{23}C_6 carbide were observed in the sintered 085Mo and 150Mo composites. According to microstructures given above, both ferrite and carbide are in the forms of lamellar particles.

This means that both M_3C and $M_{23}C_6$ carbides are in the forms of lamellar particles. Although the existence of ferrite + $M_{23}C_6$ pearlite is not as common as that of ferrite + M_3C pearlite, some previous works [51], [52] provide evidence of the former pearlite.

Strong XRD peaks corresponding to fcc crystal structure of γ -austenite were observed in the sintered 150Mo composite. The XRD peaks of γ -austenite confirms the existence of ausferrite in this sintered composite. In the case of sintered composite with low volume fraction of ausferrite, XRD characterization alone may provide insufficient information. For example, the SEM image of sintered 085 composite (Figure 4.6c) shows ausferrite but there are no XRD peaks corresponding to fcc crystal structure of γ -austenite in this sintered composite. The absence of austenite XRD peaks in the sintered 085 composite is certainly attributed to low volume fraction of austenite or ausferrite.

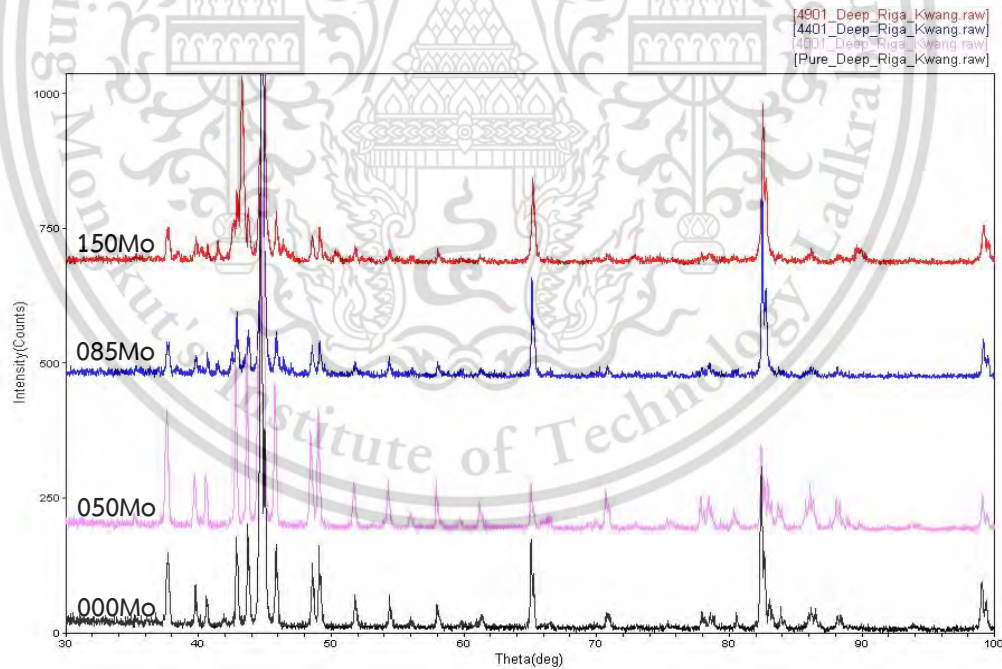


Figure 4.5 The X-ray diffraction patterns of the sintered composites.

4.5. Mechanical properties

4.5.1 Hardness

The Rockwell hardness values of sintered Fe-Si-C composite and sintered Fe-Mo-Mn-Si-C composites are given in Figure 4.9. The hardness of sintered 000Mo, 050Mo, 085Mo and 150Mo composites were 74.67HRB, 76.03HRB, 92.44HRB and 102.30HRB, respectively. The experimental results indicate that hardness of sintered composites increases with increasing Mo content. According to Table 4.1, the increase of Mo content results in decrease of ferrite fraction but increases of black particle and pearlite + ausferrite fractions. Pearlite and ausferrite can be considered as the microstructural components that contribute to hardness increase. In general, the hardness is inversely proportional to ausferrite size [53]–[55]. The SEM images of the sintered 085Mo (Figure 4.6c) and 150Mo (Figure 4.6d) shows no ausferrite size difference. Thus, the contribution of ausferrite on hardness is negligible here. The pearlite contribution on hardness increase is more important. As aforementioned, the pearlite interlamellar spacing decreases with increasing Mo content. Since the hardness is inversely proportional to the pearlite interlamellar spacing [56], [57], it is justifiable that the increase of Mo content leads to finer pearlite interlamellar spacing, which in turn causes hardness increase.

Another Mo contribution on hardness is its solid solution strengthening/hardening effect in ferrite of sintered composites. This effect has been reported in both wrought steel [58], powder metallurgy steel [59] and cast steel [60].

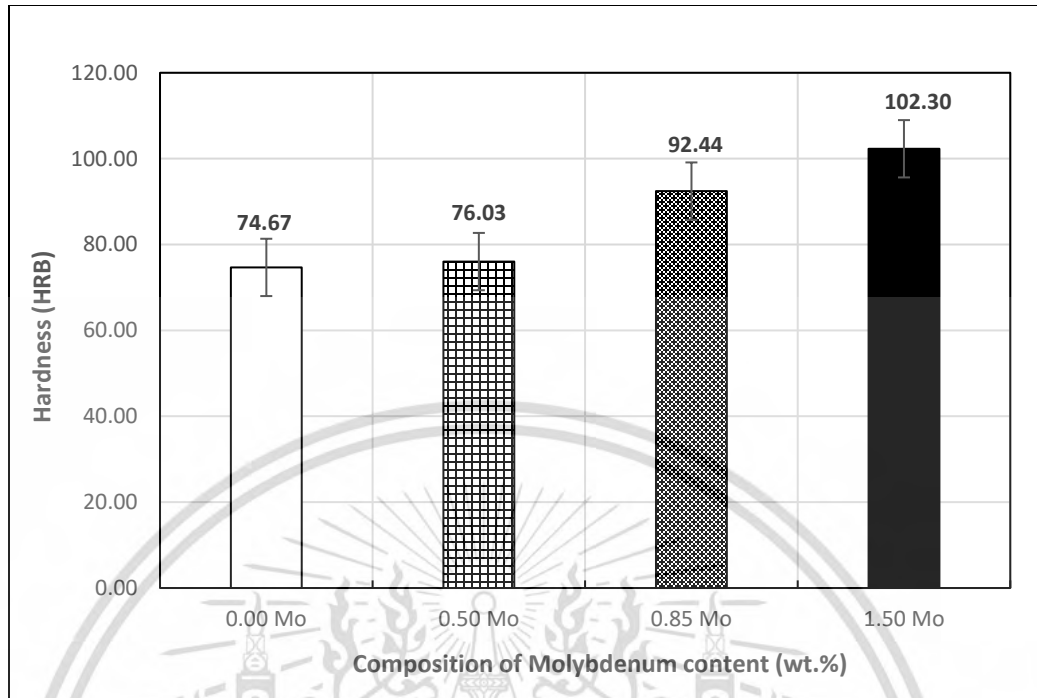


Figure 4.6 The hardness values of the sintered Fe-Mo-Mn-Si-C composites.

4.5.2 Tensile properties

The tensile properties of sintered Fe-Si-C composite and sintered Fe-Mo-Mn-Si-C composites are given in Figure 4.10. The tensile strengths of sintered composites increased with increasing Mo content, which was directly related to the volume fraction of dark grey areas consisting of pearlite and ausferrite. The measured ultimate tensile and yield strengths showed similar trend to that of the hardness value. The values of elongation at break were in the range of 2.5-4.0%.

In general, mechanical property of a material depends on its microstructure. All microstructural components of sintered composites, given in Table 4.1, have contributions to tensile properties. Regarding the contribution of graphite nodules on deformation behavior of DIs, the graphite nodules are assumed as either voids or as rigid, and unbonded particles [61]. The impacts of graphite nodules as voids or particles on DI deformation are not much different. In this work the fraction of black particles (Table 4.1), which are

equivalent to graphite nodules in DIs, increases with increasing Mo content, which is directly proportional to tensile strength. This means that the increase of fraction of black particles has a direct relationship with the increase of tensile strength. Similar relationship was reported in an as-cast and as-sintered DIs [62].

The contribution of sintered composite matrix on tensile strengths can be considered from the decrease of ferrite fraction and the increase of dark grey area (pearlite + ausferrite) fraction with increasing Mo content. Since the sintered composite matrix consists of ferrite and dark grey area it can be simply classified as dual phase material. Therefore, the dependence of sintered composite mechanical properties on the dark grey area fraction can be explained in similar fashion as that of a dual phase material consisting of ferrite and hard structure. According to micromechanical models for a dual phase material, the increase of hard phase results in enhancement of mechanical properties [63]–[66].

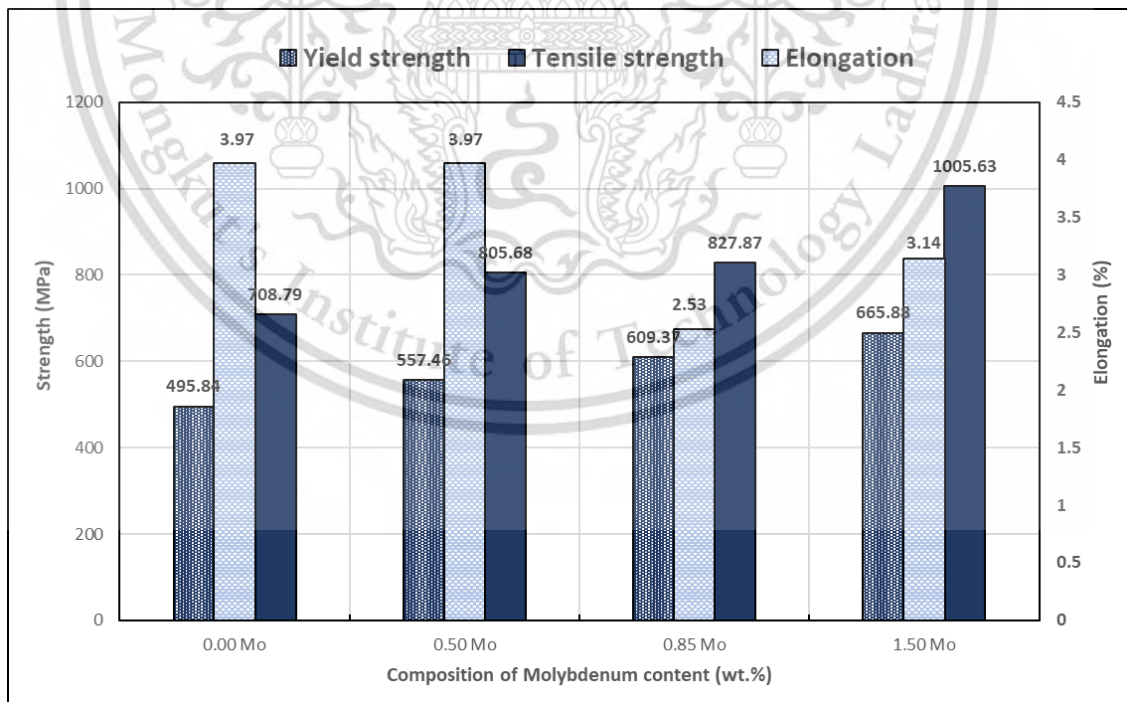


Figure 4.7 The tensile properties of sintered composites.

4.6. Friction coefficient

The friction coefficient values of sintered Fe-Mo-Mn-Si-C composites were examined under following conditions. The sliding velocity was 0.1 m/s at normal loads of 5, 10, 15N. All specimens were tested under sliding distance of 1,000 m at room temperature with relative humidity of 60%. The specimens for tribometer test were disks with roughness of 4-5 μm under a ball made of SKF chromium steel grade G20 that had diameter of 7 mm with hardness of 838 ± 21 HV and had roughness of 4 μm as a counterpart material.

The friction coefficients of sintered composites with different Mo contents, tested under normal loads of 5N, 10N, and 15N, are shown in Figure 4.11-4.13, respectively. The friction/distance plots showed two stages, such as the run-in stage and the stable stage. The run-in stage appeared at sliding distance range of 0-100m, in which the unsteady friction coefficient was detected. When the sliding distances were longer than about 100m, the friction coefficient became stable. In most cases of sintered Fe-Mo-Mn-Si-C composites, the friction coefficient decreased from the run-in state down to a constant value at the steady state. This is attributed to two reasons. The first is due to the change of point contact to surface contact. The second is due to the fact that graphite shells of black particles are flaked off and graphite flakes lubricate the rubbing surfaces, resulting in decrease of the friction coefficient [67].

With exception, the friction coefficient at the steady stage was higher than that in the run-in stage for the sintered 000Mo composite tested at the load of 15N. The initial friction coefficient increases because the influence of ploughing effect, inclusion of trapped wear particles and roughening of the disc surface is higher than that of the flaked off graphite lubrication. Thus, the friction coefficient gradually increases until it reaches a stable value.

The friction coefficients at the steady stage are listed in Table 4.2. The results show that the friction coefficient of the sintered composite with higher Mo content is obviously lower than that of the sintered composite with lower Mo content. However, it does not mean that the Mo addition can directly improve the friction coefficient of sintered Fe-Mo-Mn-Si-C composites but because the increase of Mo content leads to the increase of fraction of black particles, which act as lubricating material for reducing direct contact areas between two rubbing surfaces. The reduction of direct contact areas causes decrease in the friction coefficient.

Experimental results show that friction coefficient increase with increasing normal load, which causes the increase of the adhesion strength. The explanation for the increase of the adhesion strength with increasing normal load is given in [68]. At a low normal load, the oxide film effectively separates two rubbing metal surfaces, resulting in less metallic contact, hence the friction coefficient is low. At a high normal load, the oxide film is broken, resulting in intimate metallic contact, which leads to the increase of adhesion strength, hence the friction coefficient is high.

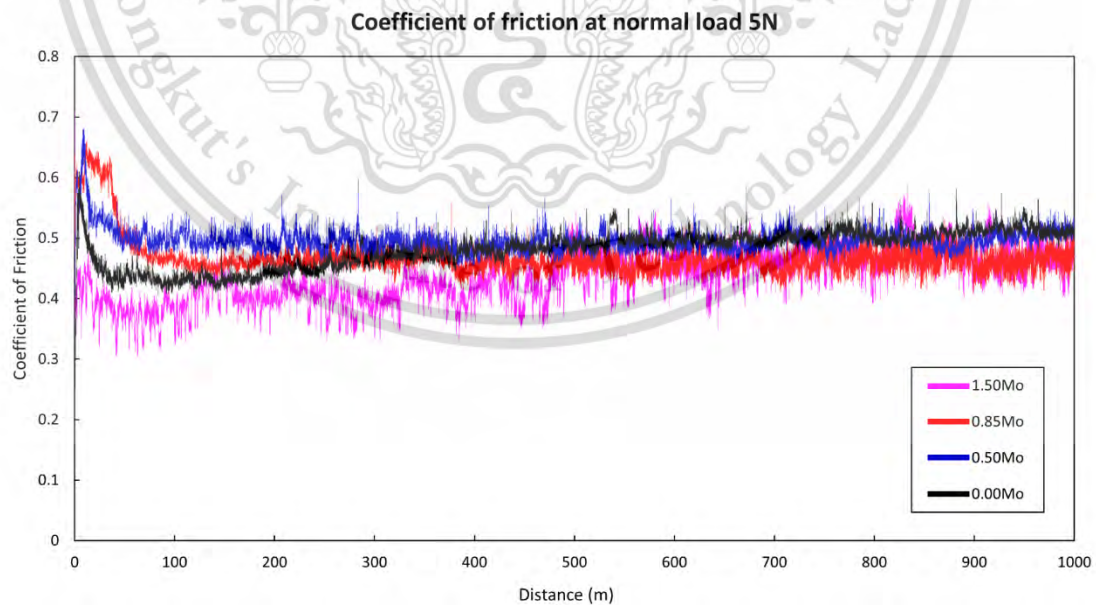


Figure 4.8 Friction coefficients of sintered composites tested at load of 5 N.

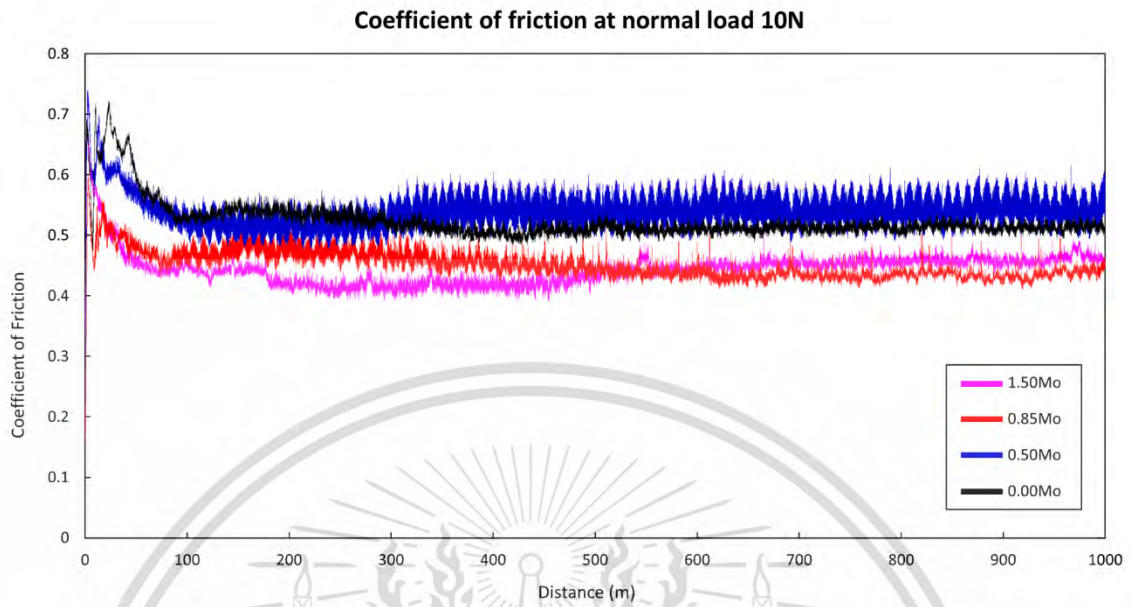


Figure 4.9 Friction coefficients of sintered composites tested at load of 10 N.

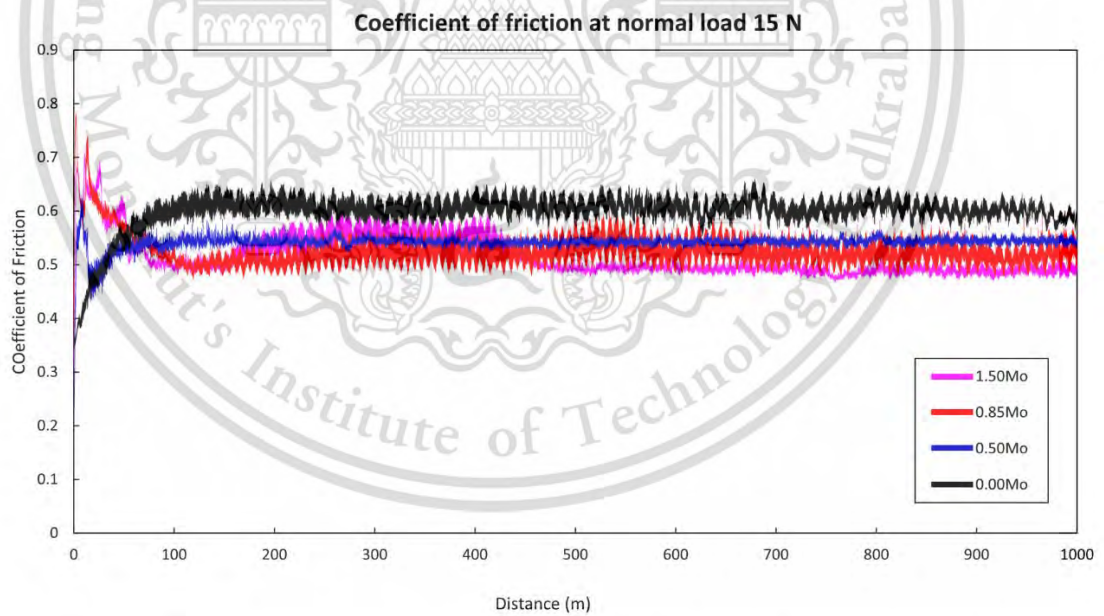


Figure 4.10 Friction coefficients of sintered composites tested at load of 15 N.

Table 4.2 Friction coefficients of sintered composites under different normal loads.

Molybdenum (wt.%)	Friction coefficient		
	5N	10N	15N
000Mo	0.49	0.52	0.61
050Mo	0.50	0.54	0.54
085Mo	0.46	0.45	0.52
150Mo	0.44	0.44	0.51

4.7. Wear rates

The wear rates, with respect to sliding distance and normal applied load and used to express the material removal during tribology test, are listed in Table 4.3. Figure 4.14 demonstrates the effect of different normal applied loads of 5N, 10N, 15N on the wear rate of sintered composites at a constant sliding speed of 0.1 m/s. It is inferred that the wear rate of sintered composites is proportional to the normal load, i.e., the increase of normal load leads to wear rate increase. The increase of normal load leads to the thermal softening of material and crack propagation is raised resulting in easy formation of wear fragment.

Under each normal load, the wear rate decreased with increasing Mo content (Figure 4.14). In other words, the wear resistance, the inverse of wear rate, increased with increasing Mo content. It is noticed that the hardness of sintered composites increases with increasing Mo content (Figure 4.9). This means that the wear resistance of sintered composites is directly proportional to hardness. This is consistent with Archard's law stating that wear resistance is proportional to hardness [69]. In addition, because the black particle fraction increases with increasing Mo content the degree of wear is reduced due to higher probability of rubbing surfaces to be lubricated.

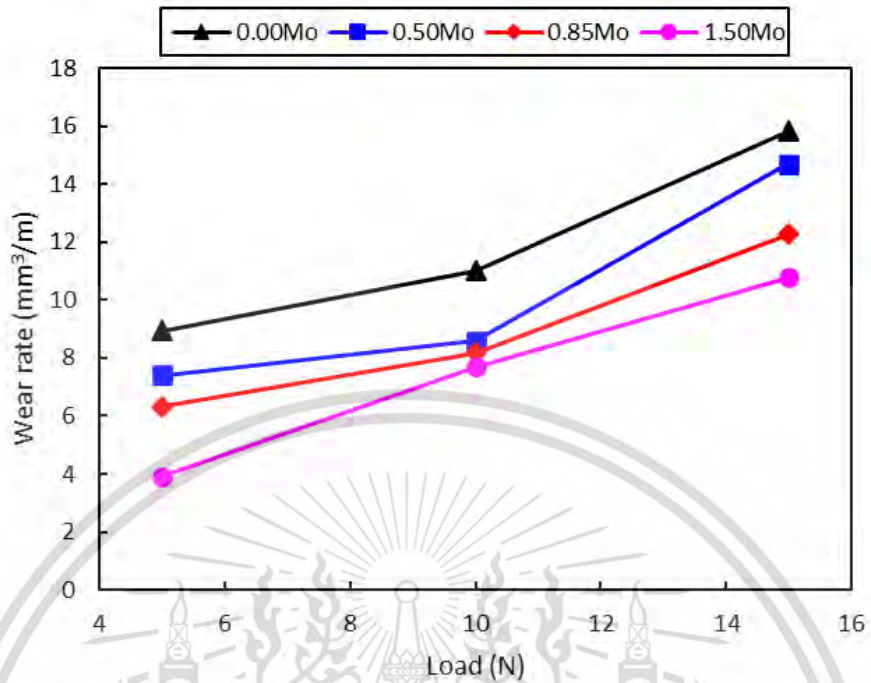


Figure 4.11 Plot of wear rate against normal load for different sintered composites.

Table 4.3 Wear rate of sintered Fe-Mo-Mn-Si-C composite and sintered Fe-Si-C composite under difference Molybdenum content

Sintered composite	Wear rate at specific normal load (mm ³ /m)		
	5N	10N	15N
000Mo	8.95	11.02	15.82
050Mo	7.41	8.58	14.70
085Mo	6.31	8.18	12.28
150Mo	3.92	7.70	10.78

4.8. Worn surfaces and wear debris

4.8.1. Worn surfaces of sintered composites tested under load of 15N

The SEM images of worn surfaces of sintered composites, tested under normal load of 15N, are shown in Figure 4.15. The wear mechanisms observed in on worn surfaces of sintered composites include abrasion and delamination. In abrasion wear mechanism, a surface, sliding against harder particles or protuberances, undergoes plastic deformation and scratching as abrasive grooves parallel to sliding direction [70], [71]. The delamination craters are formed by cracks propagating under and parallel to a rubbing surface. All worn surfaces of sintered composites show agglomerates of oxides, which indicate oxidative wear [70].

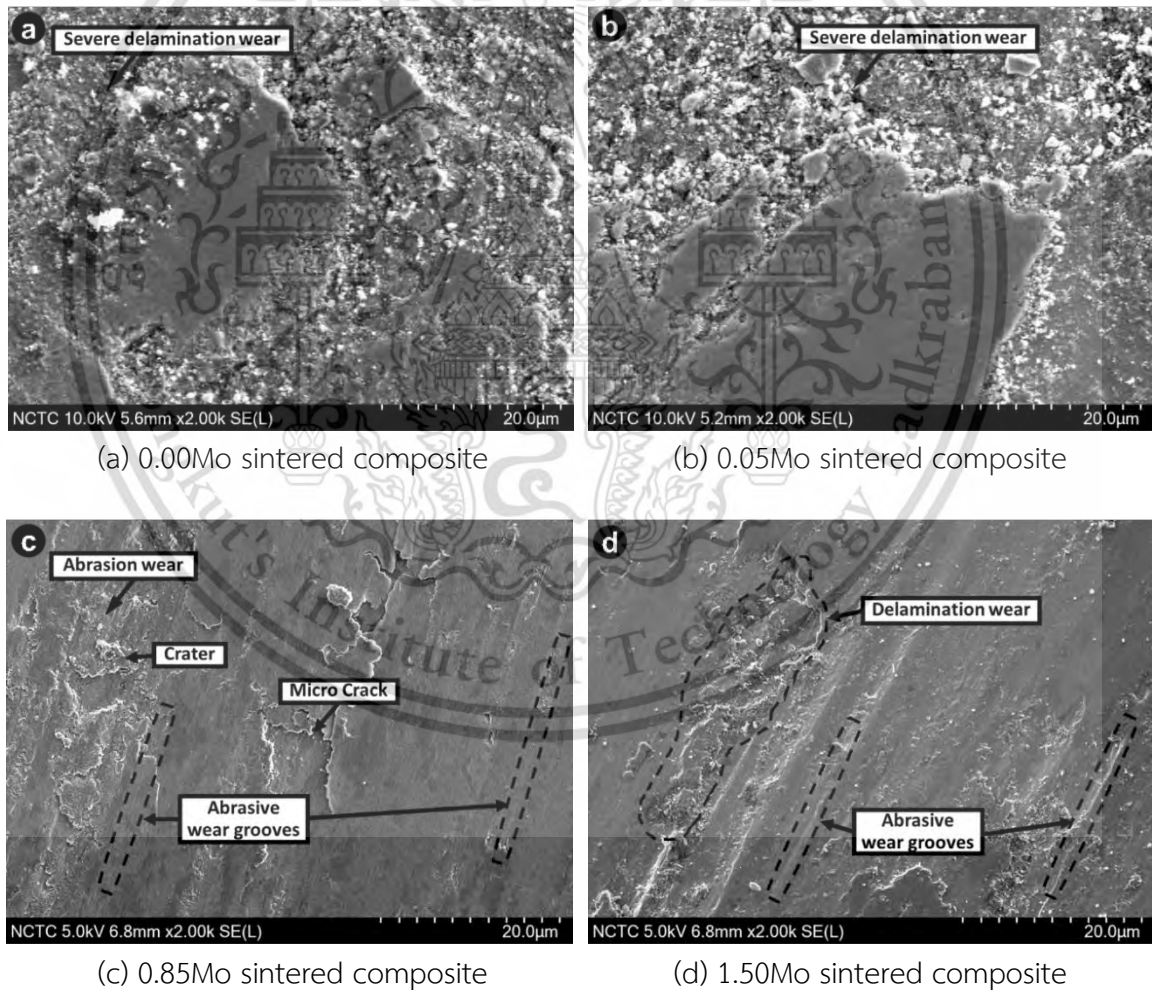
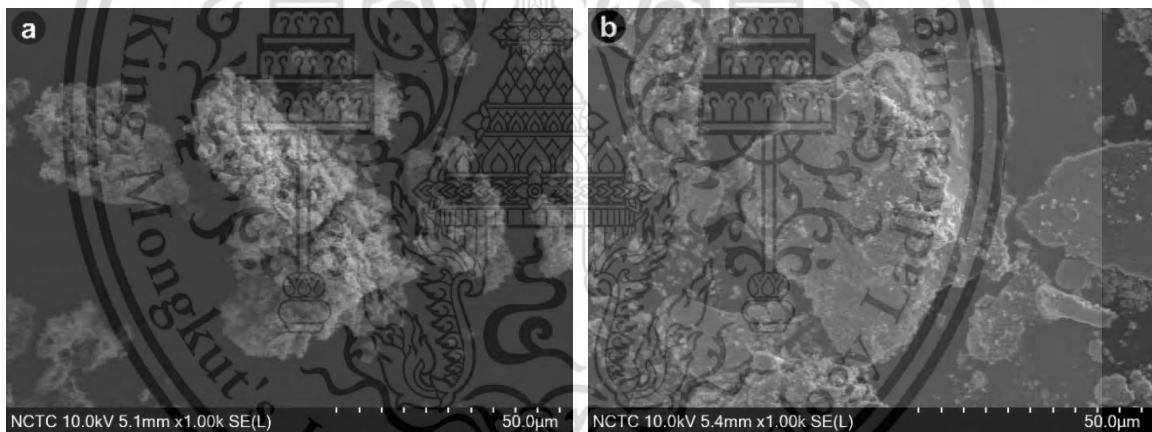


Figure 4.12 SEM micrograph of worn surface of sintered composite at load of 15N.

4.8.2. Wear debris of all sintered composite at normal load 15N

The SEM images of wear debris from dry-sliding tests of sintered composites under normal load of 15N are shown in Figure 4.16. The debris showed particulate and flaky shapes. The debris formation is related to oxidation because the clean rubbing metal surfaces can be oxidized rapidly to form very thin oxide films and later the load-bearing layers formed during sliding wear contain a high percentage of oxygen [72]. The breakage of oxidized layers leads to either the formation of triboparticulates or formation of compacted oxide layers. The further breakage or subsurface delamination of the compacted oxide layers results in particles with different shapes due to the severe plastic deformation show irregular geometry which confirm the delamination wear mechanism. Whereas the debris formed at higher Molybdenum content was large and plate-like structure which also indicate the adhesion wear [73].



(a) 0.00Mo sintered composite

(b) 0.05Mo sintered composite

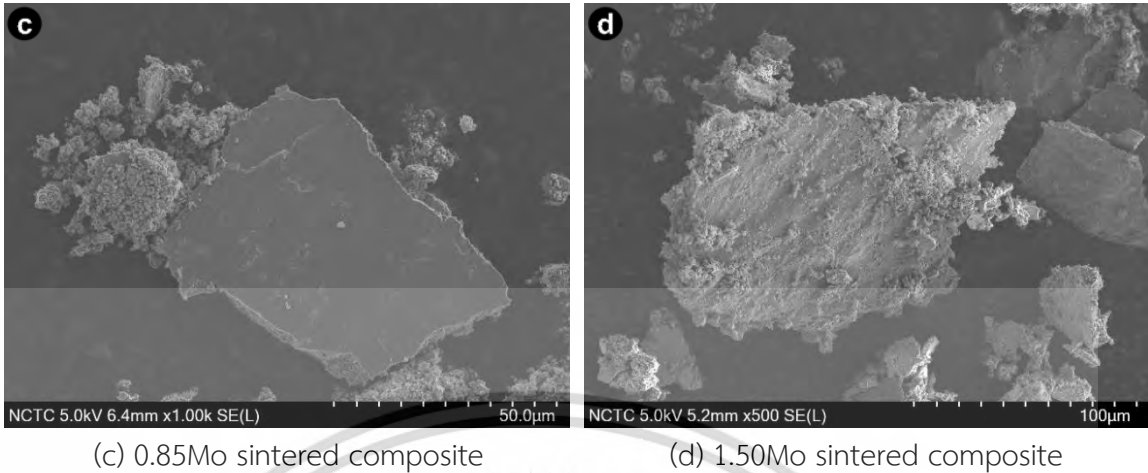


Figure 4.13 SEM micrograph of wear debris of sintered composite at load of 15N.

4.8.3. EDS analysis of wear debris at normal load 15N

The EDS spectra, determined on wear debris from dry-sliding tests at normal load of 15N of sintered composites, are shown in Figures 4.17-4.20. All wear debris of sintered composites showed strong oxygen and iron peaks, which may be referred to iron oxide formed from oxidative wear.

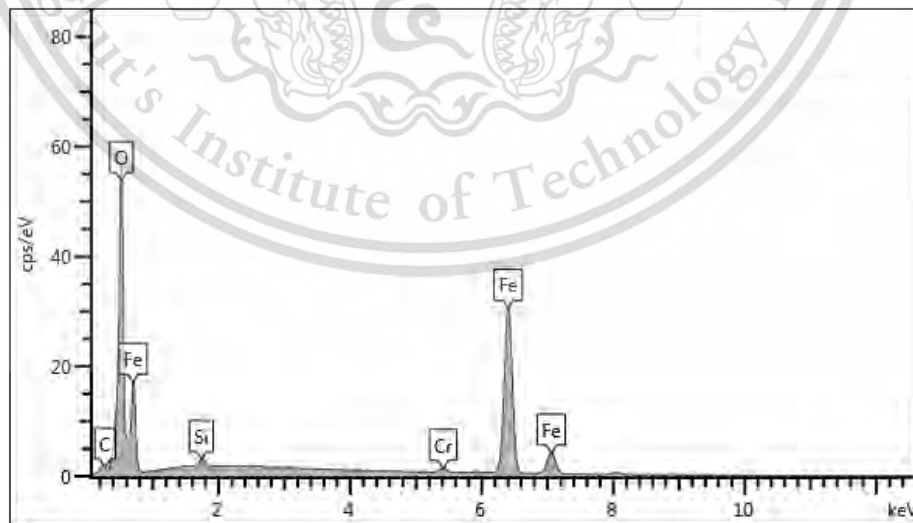


Figure 4.14 EDS spectrum of wear debris from sintered 0.00Mo composite.

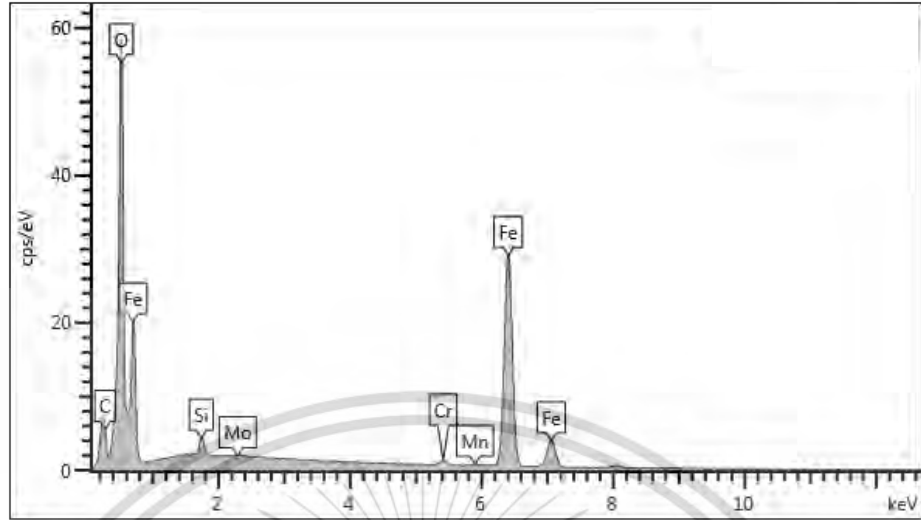


Figure 4.15 EDS spectrum of wear debris from sintered 050Mo composite.

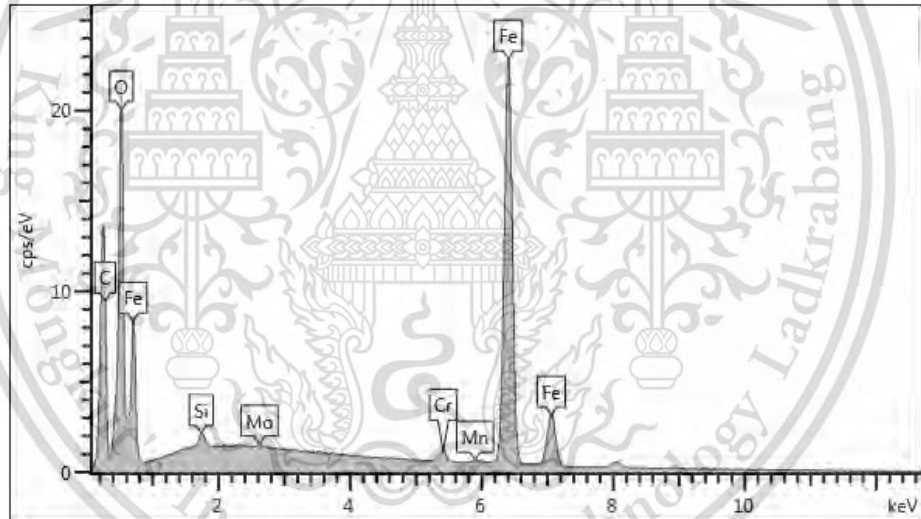


Figure 4.16 EDS spectrum of wear debris of sintered 085Mo composite.

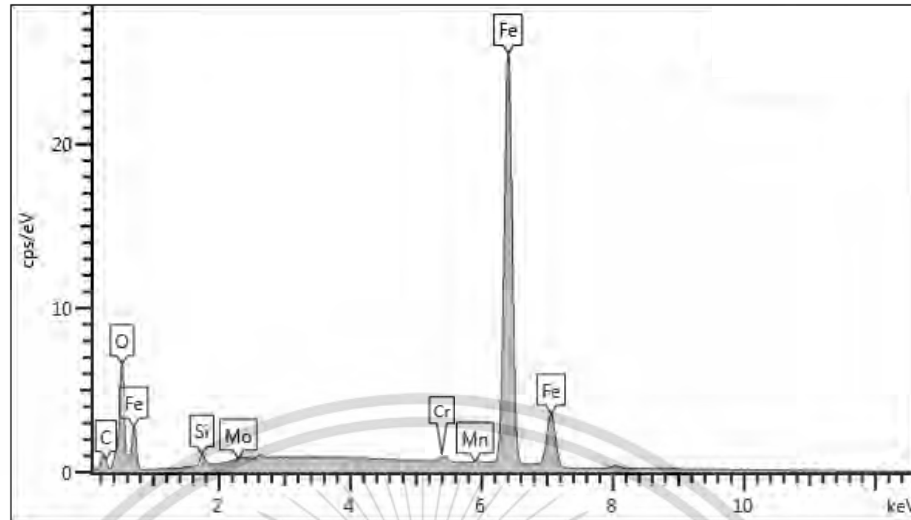


Figure 4.17 EDS spectrum of wear debris from sintered 150Mo composite.

4.8.4 Worn surfaces and wear debris: Effect of normal load

4.8.4.1 Sintered 000Mo composite

The SEM images of worn surfaces and wear debris from dry-sliding tests under different normal loads on sintered 000Mo composite are shown in Figures 4.21 and 4.22, respectively. The severe delamination wear was observed on worn surfaces tested under all normal loads. The wear debris from the tests at 5N and 10N showed flakes while wear debris from the test at 15N showed irregular geometry. The debris morphology indicates the delamination wear.

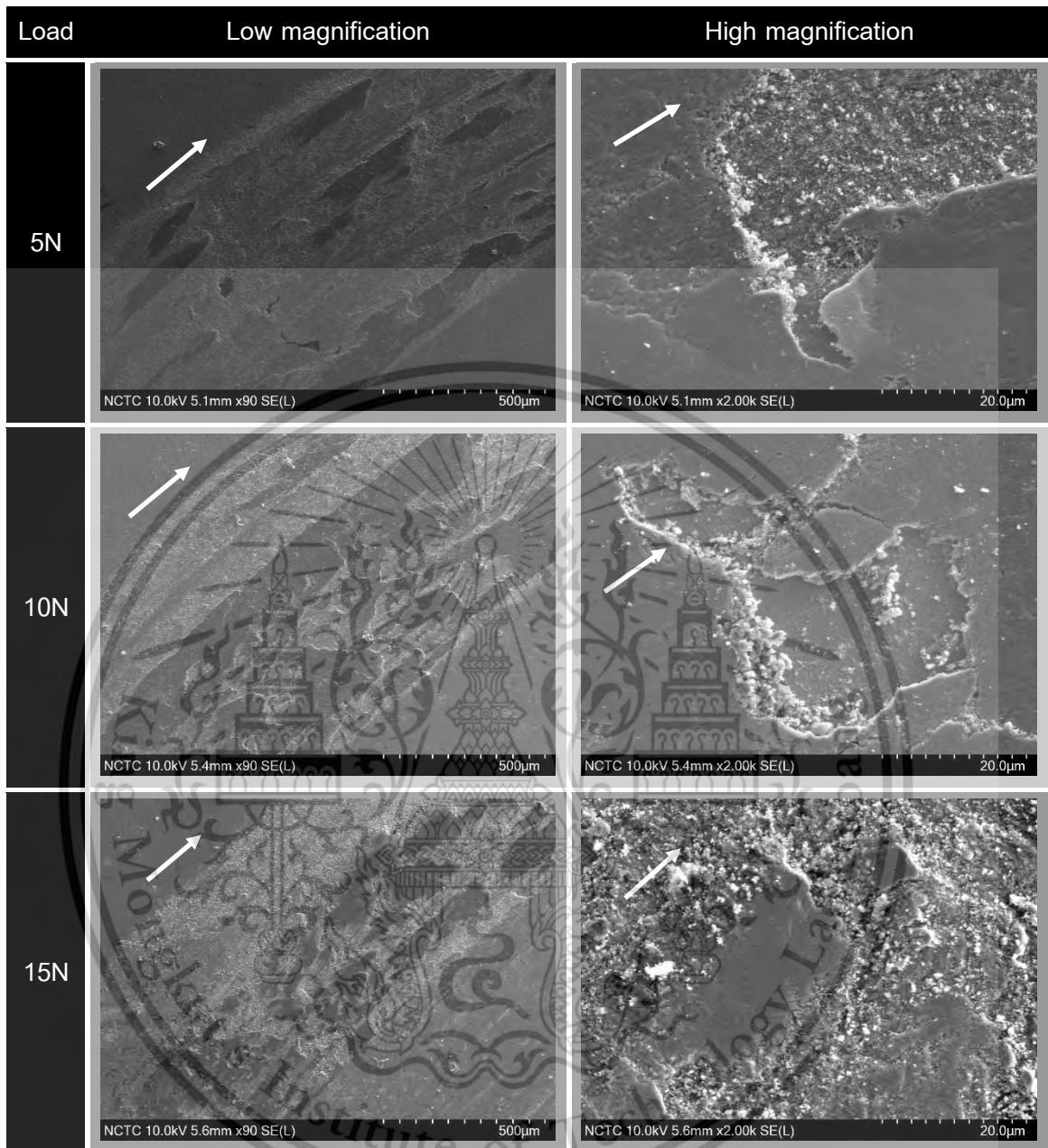
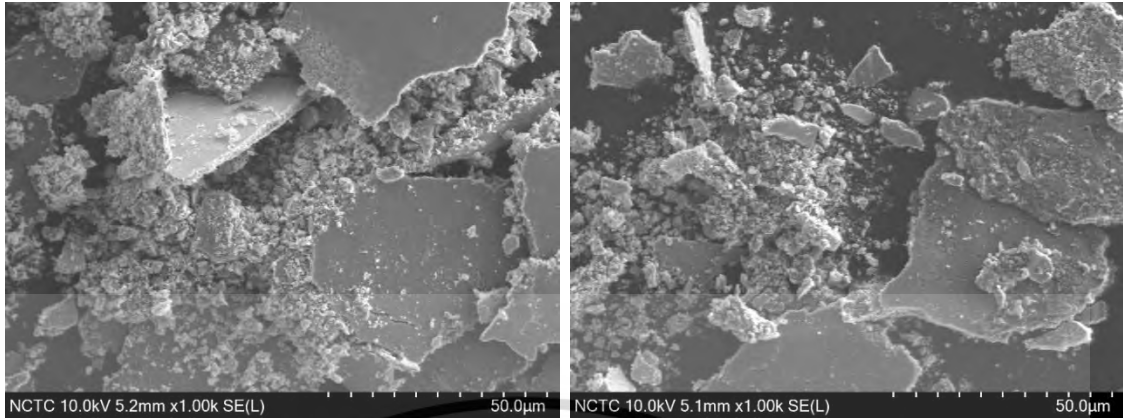
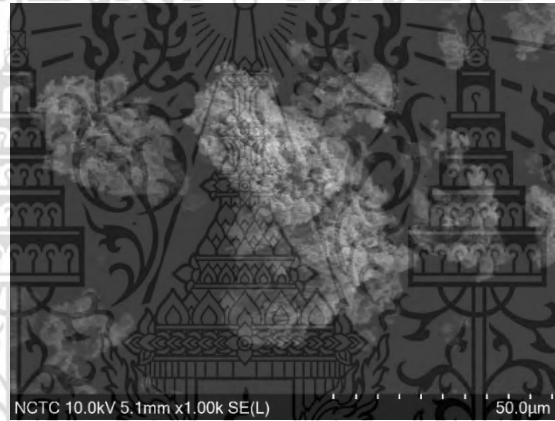


Figure 4.18 SEM images of worn surfaces of sintered 000Mo composite.



(a) Wear debris at load of 5N

(b) Wear debris at load of 10N



(c) Wear debris at load of 15N

Figure 4.19 SEM images of wear debris of sintered 000Mo composite.

4.8.4.2. Sintered 050 Mo composite

The SEM images of worn surfaces and wear debris from dry-sliding tests under different normal loads on sintered 050Mo composite are shown in Figures 4.23 and 4.24, respectively. The degree of surface damage increased with increasing normal load. The worn surfaces consisted of severe delamination and some abrasive grooves at load of 15N. The wear debris with flake-like shape confirm the delamination wear.

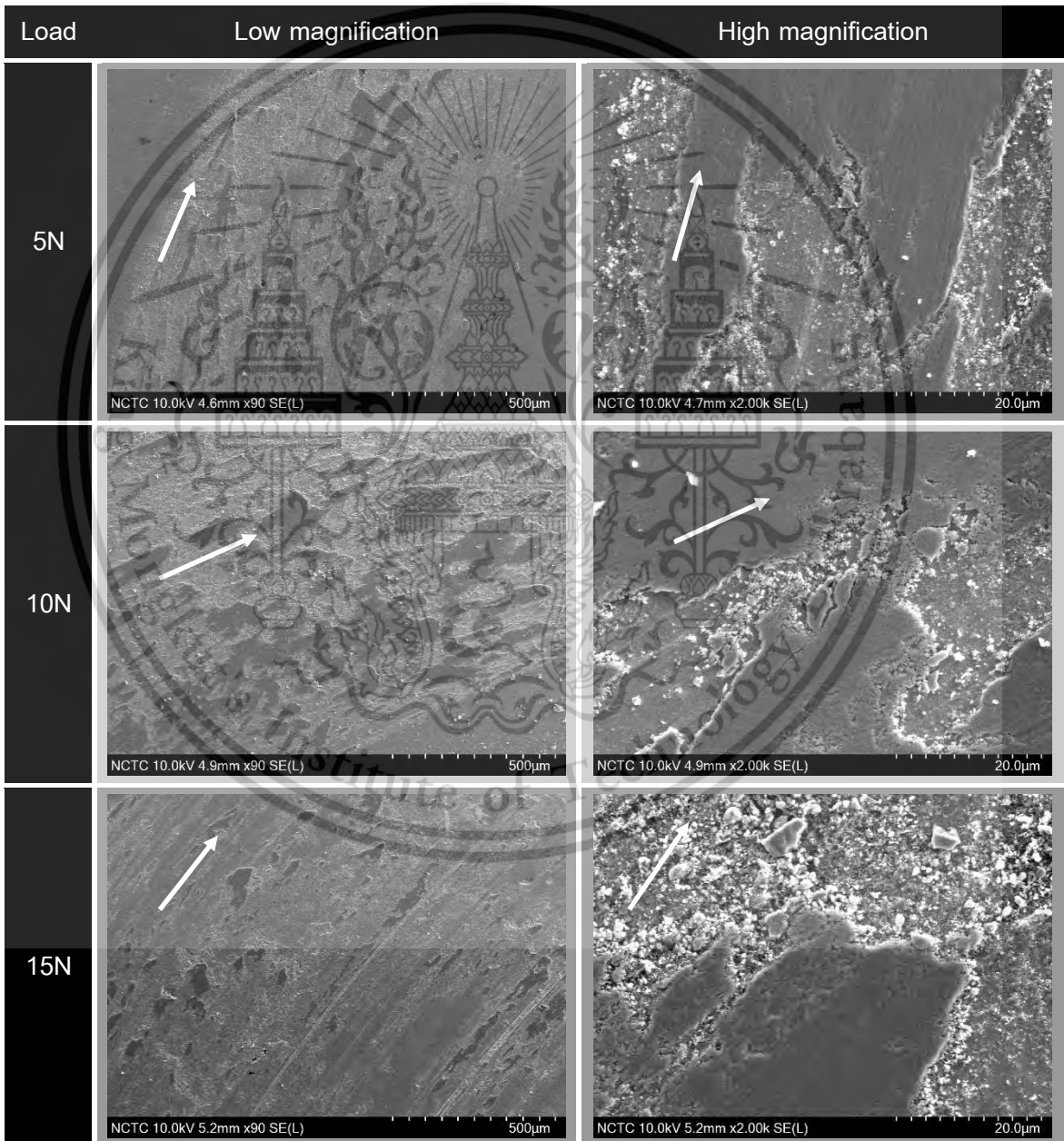
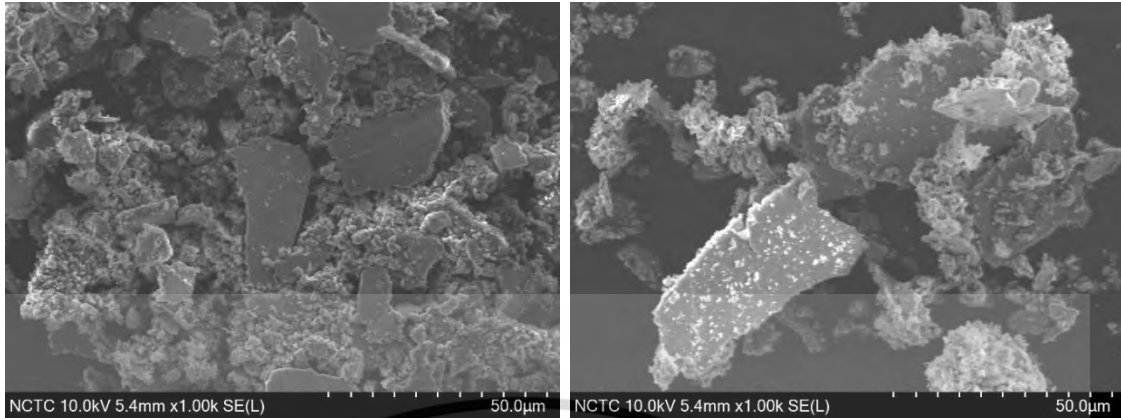


Figure 4.20 SEM images of worn surfaces on sintered 050Mo composite.



(a) Wear debris at load of 5N

(b) Wear debris at load of 10N



(c) Wear debris at load of 15N

Figure 4.21 SEM micrograph of wear debris of sintered 050Mo composite.

4.8.4.3 Sintered 085 Mo composite

The SEM images of worn surfaces and wear debris from dry-sliding tests under different normal loads on sintered 085Mo composite are shown in Figures 4.25 and 4.26, respectively. The worn surfaces showed characters of delamination and abrasion wears at all load conditions. The microcrack was observed at 15N load condition. The debris with flake-like shape confirm the delamination wear.

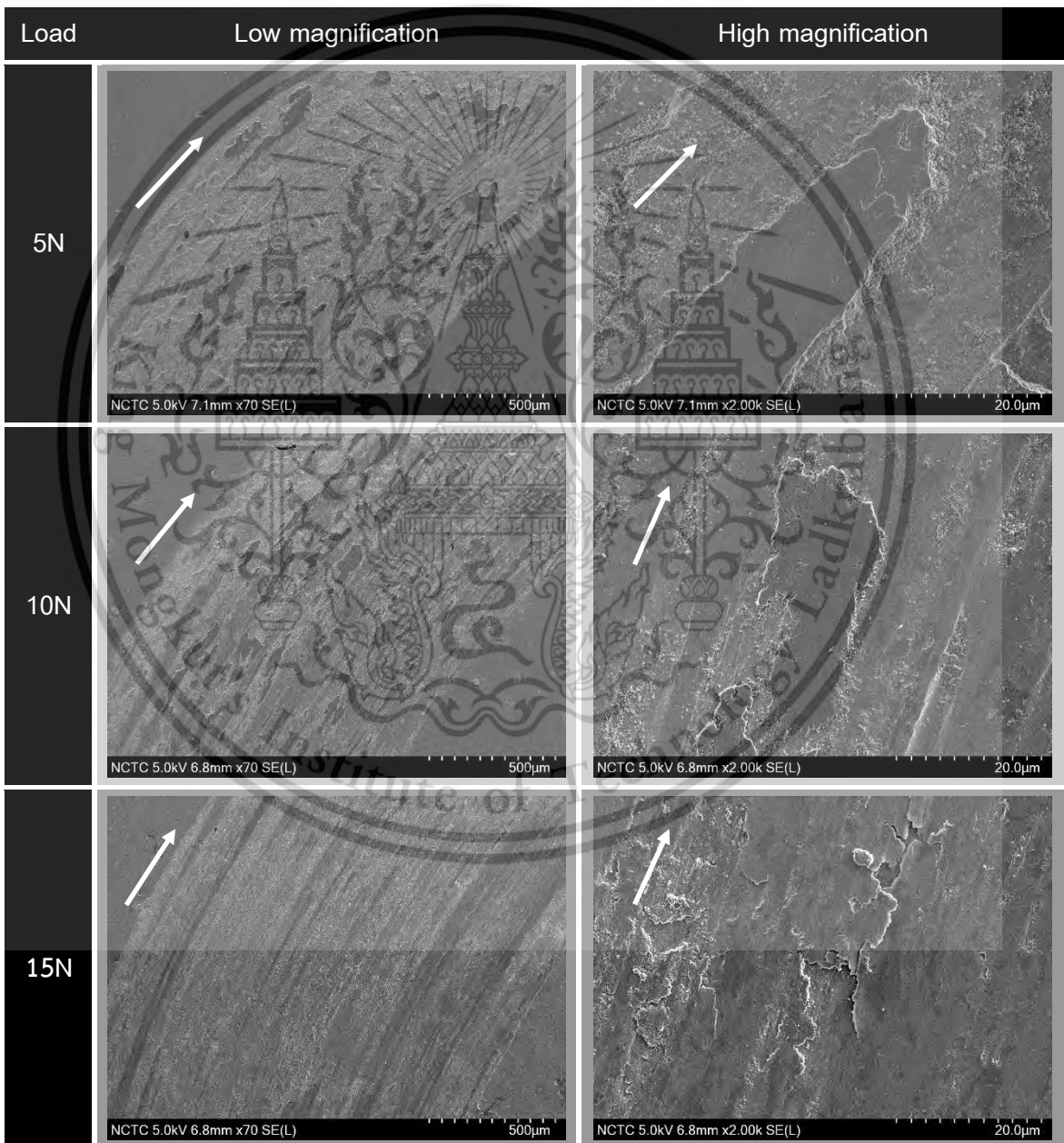
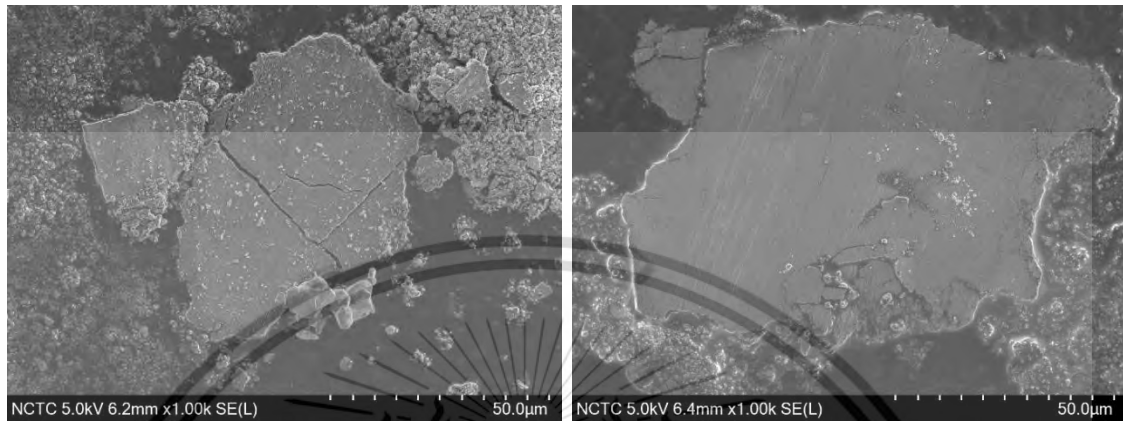


Figure 4.22 SEM images of worn surfaces of sintered 085Mo composite.



(a) Wear debris at load of 5N

(b) Wear debris at load of 10N



(c) Wear debris at load of 15N

Figure 4.23 SEM images of wear debris of sintered 085Mo composite.

4.8.4.4 Sintered 150 Mo composite

The SEM images of worn surfaces and wear debris from dry-sliding tests under different normal loads on sintered 150Mo composite are shown in Figures 4.27 and 4.28, respectively. It was revealed by SEM observation that wear mechanisms included abrasion and delamination. The wear debris morphologies of particulate and flake confirm abrasion and delamination wear mechanisms.

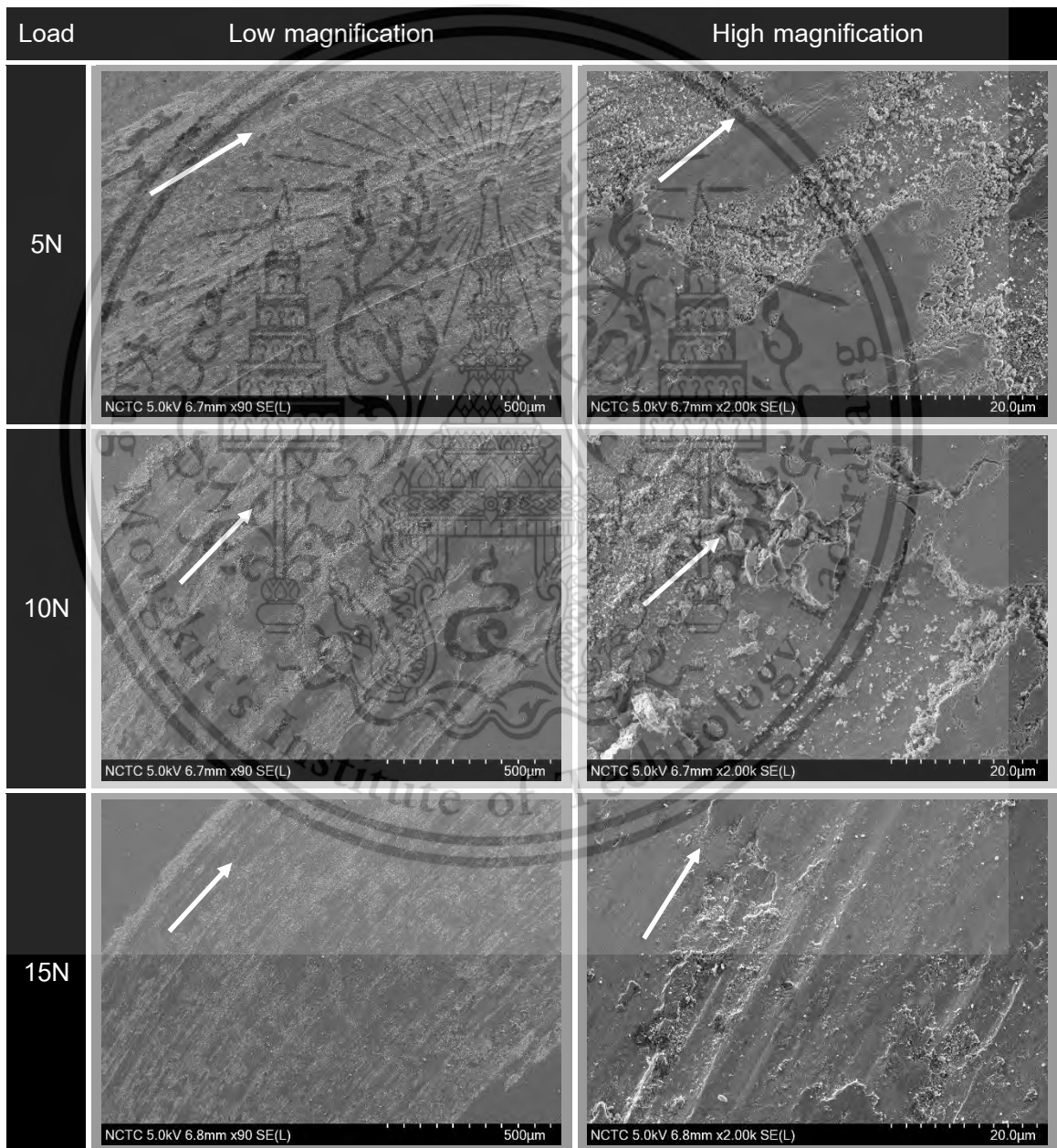
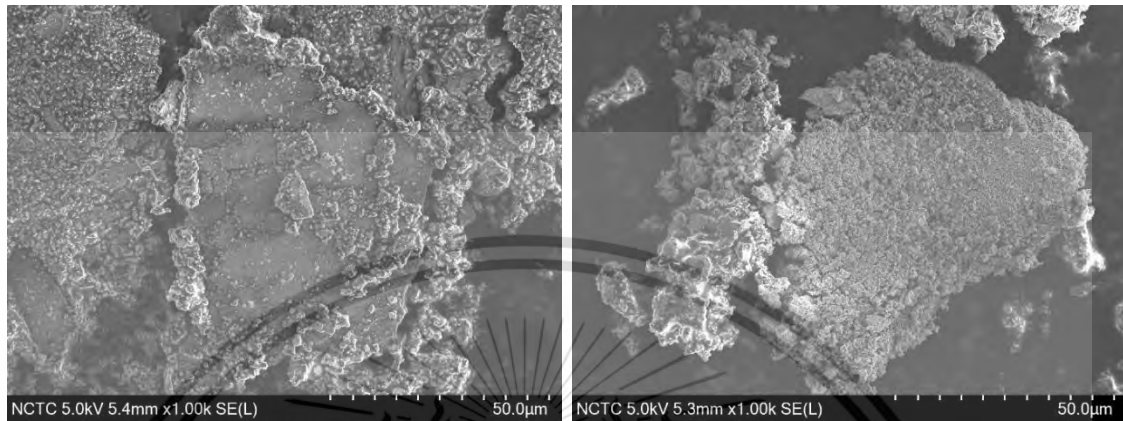


Figure 4.24 SEM images of worn surfaces of sintered 150Mo composite.



(a) Wear debris at load of 5N

(b) Wear debris at load of 10N



(c) Wear debris at load of 15N

Figure 4.25 SEM micrograph of wear debris of sintered 150Mo composite.

4.9. Counter ball surfaces

The SEM images of counter ball surfaces rubbing against sintered composites, tested under normal load of 15N, are shown in Figure 4.29. The results show many abrasive grooves parallel to the sliding direction in all specimens and wear debris glued on ball surfaces countered with sintered 000Mo, 050Mo, and 085Mo composites. The grooves are typical features associated with the abrasive wear. Few micro cracks were observed on the ball countered with sintered 085Mo composite, while the severe delamination wear was present on the ball rubbed against sintered 150Mo composite. The counter balls, rubbed against sintered high Mo-containing composites having high hardness, show high degree of surface damage.

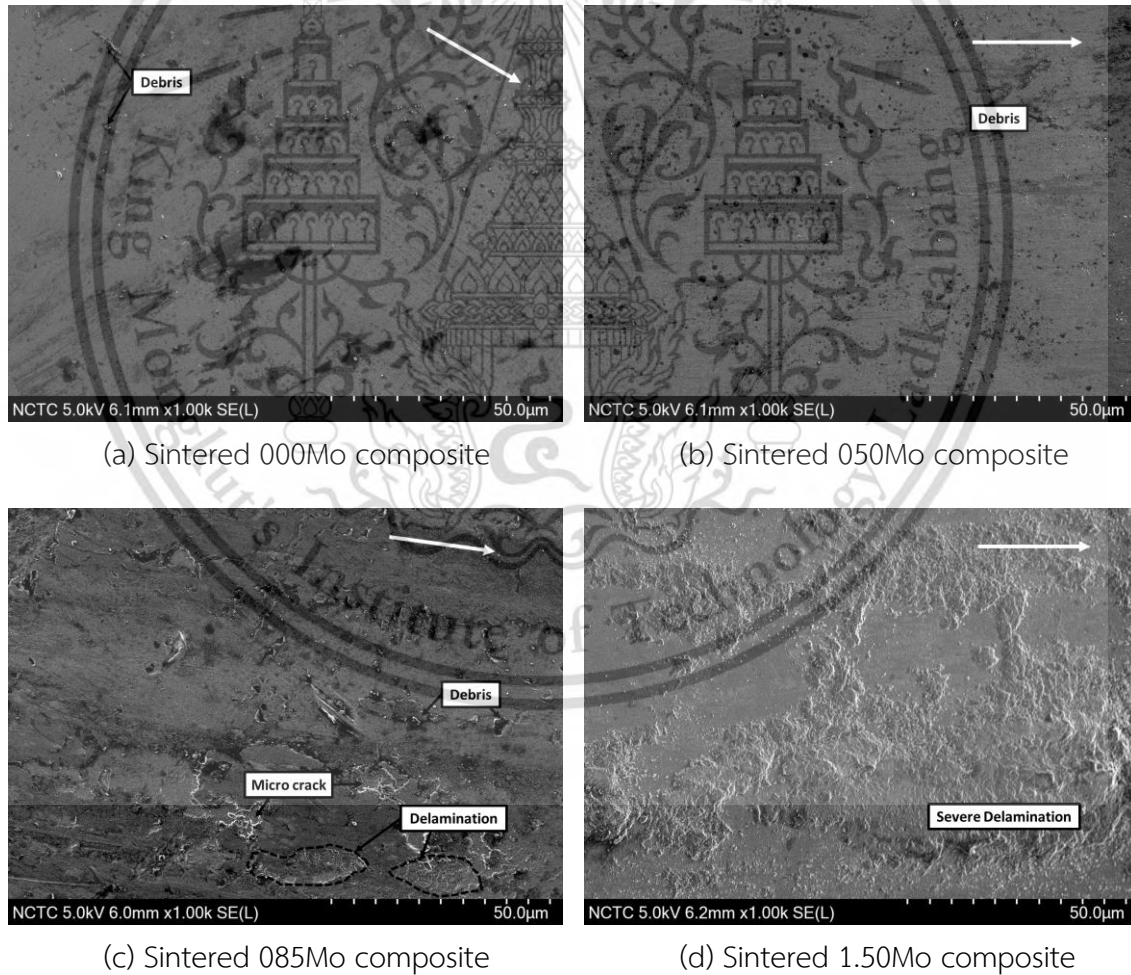


Figure 4.26 SEM images of counter ball surfaces test at load of 15N.

CHAPTER 5

CONCLUSIONS AND RECOMMENDATIONS

The present research was conducted to study the influence of Mo on microstructure, mechanical properties, and dry sliding wear behavior of sintered Fe-Mo-Mn-Si-C composites. The major findings from experimental results are summarized below.

- 1) Sintered composites showed microstructure resembling that of a ductile iron.
- 2) Sintered composites showed Mo-dependent microstructural change.
- 3) The fraction of ferrite decreased whereas those of black particle, pearlite and ausferrite increased with increasing Mo content.
- 4) The hardness and tensile strength of sintered composites increased with pearlite plus ausferrite fraction, which was related to Mo content.
- 5) Friction coefficient of sintered composites decreased with increasing black particle fraction, which in turn increased with increasing Mo content.
- 6) The wear rate of sintered composites increased with increasing applied normal load, but it decreased with increasing black particle fraction, hardness, and strength.
- 7) The wear mechanisms, deduced from characters of worn surfaces and wear debris, included delamination and abrasion.

REFERENCES

- [1] J. Luo, "Guest editorial: Special issue on 6th World Tribology Congress," *Friction*, vol. 5, no. 3, pp. 231–232, 2017, doi: 10.1007/s40544-017-0187-1.
- [2] S. Senthur Prabu, S. Prathiba, M. A. Asokan, and V. Sai Akhil, "Effect of titanium on dry sliding wear behavior of hot forged P/M low alloy steels," *Mater. Today Proc.*, vol. 22, pp. 1380–1389, 2019, doi: 10.1016/j.matpr.2020.01.481.
- [3] D. Ramakrishnan, *Automotive applications of powder metallurgy*. Woodhead Publishing Limited, 2013.
- [4] K. Yamaguchi, N. Takakura, and S. Imatani, "Materials Processing Technology," *Adv. Mater. Res.*, vol. 418–420, no. 96, pp. 1–6, 2012.
- [5] E. Beşteek, "Powder Metallurgy Processes and Making Metal Powder," no. October, pp. 2–5, 2020, doi: 10.13140/RG.2.2.21469.84967.
- [6] Anon, "Powder Metallurgy.," *ATB Metall.*, vol. 27, no. 2–3, pp. 45–121, 1987, doi: 10.1016/0026-0657(95)92855-3.
- [7] M. Maalekian, "Christian Doppler Laboratory for Early Stages of Precipitation The Effects of Alloying Elements on Steels (I)," *Eff. Alloy. Elem. Steels*, vol. 1, no. October, p. 36, 2007.
- [8] A. K. Bhargava and M. K. Banerjee, "Hardenability of Steel," *Compr. Mater. Finish.*, vol. 2–3, pp. 50–70, 2017, doi: 10.1016/B978-0-12-803581-8.09186-4.
- [9] T. Sunil, M. Sandeep, R. Kumaraswami, and A. Shravan, "A critical review on solid lubricants," *Int. J. Mech. Eng. Technol.*, vol. 7, no. 5, pp. 193–199, 2016.
- [10] P. A. Flinn, "Strengthening Mechanisms in Solids," *a. S. M.*, p. 17, 1962.
- [11] G. Vander Voort, "Written by : Microstructure of Ferrous Alloys," vol. 3, no. 7, pp. 1–5, 1937.

- [12] F. Martin, C. García, and Y. Blanco, "Influence of residual porosity on the dry and lubricated sliding wear of a powder metallurgy austenitic stainless steel," *Wear*, vol. 328–329, pp. 1–7, 2015, doi: 10.1016/j.wear.2015.01.025.
- [13] A. Wahi, N. Muhamad, A. B. Sulong, and R. N. Ahmad, "Effect of sintering temperature on density, hardness and strength of MIM Co30Cr6Mo biomedical alloy," *Funtai Oyobi Fumatsu Yakin/Journal Japan Soc. Powder Powder Metall.*, vol. 63, no. 7, pp. 434–437, 2016, doi: 10.2497/jjspm.63.434.
- [14] F. B. Sweidan and H. J. Ryu, "Kinetic Monte Carlo simulations of the sintering microstructural evolution in density graded stainless steel fabricated by SPS," *Mater. Today Commun.*, vol. 26, no. August, p. 101863, 2021, doi: 10.1016/j.mtcomm.2020.101863.
- [15] Z. Xu, M. A. Hodgson, K. Chang, G. Chen, X. Yuan, and P. Cao, "Effect of sintering time on the densification, microstructure, weight loss and tensile properties of a powder metallurgical Fe-Mn-Si alloy," *Metals (Basel)*, vol. 7, no. 3, 2017, doi: 10.3390/met7030081.
- [16] O. Coovattanachai *et al.*, "Effect of heating rate on sintered series 300 stainless steel," *Songklanakarín J. Sci. Technol.*, vol. 32, no. 2, pp. 163–167, 2010.
- [17] A. P. G. Chaves, D. M. A. Centeno, M. Masoumi, and H. Goldenstein, "Effect of the microstructure on the wear resistance of a pearlitic steel," *Mater. Res.*, vol. 23, no. 2, pp. 1–8, 2020, doi: 10.1590/1980-5373-MR-2019-0605.
- [18] M. Krbata, M. Eckert, J. Majerik, and I. Barenyi, "Wear behaviour of high strength tool steel 90mncrv8 in contact with Si3N4," *Metals (Basel)*, vol. 10, no. 6, pp. 1–17, 2020, doi: 10.3390/met10060756.
- [19] S. Das Bakshi, "University of Cambridge Examination," *Br. J. Radiol.*, vol. 4, no. 41, pp. 210–210, 1931, doi: 10.1259/0007-1285-4-41-210.
- [20] E. Rabinowicz, L. A. Dunn, and P. G. Russell, "A study of abrasive wear under three-body conditions," *Wear*, vol. 4, no. 5, pp. 345–355, 1961, doi: 10.1016/0043-

1648(61)90002-3.

- [21] “an Analysis of the Influence of Plastic Indentation,” vol. 122, pp. 123–133, 1988.
- [22] C. Spero, D. J. Hargreaves, R. K. Kirkcaldie, and H. J. Flitt, “Review of test methods for abrasive wear in ore grinding,” *Wear*, vol. 146, no. 2, pp. 389–408, 1991, doi: 10.1016/0043-1648(91)90077-8.
- [23] A. G. Wang and I. M. Hutchings, “The number of particle contacts in two-body abrasive wear of metals by coated abrasive papers,” *Wear*, vol. 129, no. 1, pp. 23–35, 1989, doi: 10.1016/0043-1648(89)90276-7.
- [24] A. Misra and I. Finnie, “Classification of Three-Body Abrasive Wear and Design of a New Tester.,” *Electr. Power Res. Inst. EPRI EL*, vol. 60, no. April 1979, pp. 313–318, 1979.
- [25] K. Endo and H. Goto, “Effects of environment on fretting fatigue,” *Wear*, vol. 48, no. 2, pp. 347–367, 1978, doi: 10.1016/0043-1648(78)90232-6.
- [26] A. W. Batchelor, G. W. Stachowiak, and A. Cameron, “The relationship between oxide films and the wear of steels,” *Wear*, vol. 113, no. 2, pp. 203–223, 1986, doi: 10.1016/0043-1648(86)90121-3.
- [27] A. Dréano, S. Fouvry, and G. Guillonneau, “A tribo-oxidation abrasive wear model to quantify the wear rate of a cobalt-based alloy subjected to fretting in low-to-medium temperature conditions,” *Tribol. Int.*, vol. 125, no. April, pp. 128–140, 2018, doi: 10.1016/j.triboint.2018.04.032.
- [28] K. Ruangchai and A. Wiengmoon, “Microstructure , Hardness and Wear Properties of Sintered Fe-Mo-Si-C Steels with Spheroidal Graphite Iron / Compacted Graphite Iron-Like,” no. August, 2017, doi: 10.4028/www.scientific.net/KEM.751.47.
- [29] N. Zimmermann and P. H. Wang, “A review of failure modes and fracture analysis of aircraft composite materials,” *Eng. Fail. Anal.*, vol. 115, p. 104692, 2020, doi: 10.1016/j.engfailanal.2020.104692.

- [30] Y. Liu, Z. Lian, S. Liu, and T. Luo, "Fracture failure analysis and structure improvement on thread joint of turbine shaft," *Eng. Fail. Anal.*, vol. 115, no. January, p. 104625, 2020, doi: 10.1016/j.engfailanal.2020.104625.
- [31] A. Kumar, A. J. Wilkinson, and S. G. Roberts, "Quasi-cleavage fracture planes in spheroidized A533B steel," *J. Microsc.*, vol. 227, no. 3, pp. 248–253, 2007, doi: 10.1111/j.1365-2818.2007.01808.x.
- [32] C. Binder *et al.*, "Structure and properties of in situ-generated two-dimensional turbostratic graphite nodules," *Carbon N. Y.*, vol. 124, pp. 685–692, 2017, doi: 10.1016/j.carbon.2017.09.036.
- [33] N. I. Araya, C. Binder, A. N. Klein, G. Hammes, J. D. B. De Mello, and C. Aguilar, "Effect of heat treatments and SiC content in the mechanical properties and microstructure of self-lubricating steels," *Mater. Res.*, vol. 21, no. 1, pp. 1–10, 2018, doi: 10.1590/1980-5373-mr-2017-0664.
- [34] S. Chakthin, N. Poolthong, and R. Tong Sri, "Effect of reaction between Fe and carbide particles on mechanical properties of Fe-base composite," *Adv. Mater. Res.*, vol. 55–57, no. January 2008, pp. 357–360, 2008, doi: 10.4028/www.scientific.net/amr.55-57.357.
- [35] K. Ruangchai, A. Wiengmoon, M. Morakotjinda, N. Tosangthum, and R. Tong Sri, "Sintered Fe-Mo-Si-C alloys with ductile cast iron microstructure," *J. Phys. Conf. Ser.*, vol. 1144, no. 1, 2018, doi: 10.1088/1742-6596/1144/1/012099.
- [36] J. D. B. De Mello, C. Binder, G. Hammes, R. Binder, and A. N. Klein, "Tribological behaviour of sintered iron based self-lubricating composites," *Friction*, vol. 5, no. 3, pp. 285–307, 2017, doi: 10.1007/s40544-017-0186-2.
- [37] T. Peng, Q. Yan, and X. Zhang, "Stability of Metal Matrix Composite Pads During High-Speed Braking," *Tribol. Lett.*, vol. 66, no. 2, pp. 1–13, 2018, doi: 10.1007/s11249-018-1014-1.
- [38] F. Iacoviello, O. Di Bartolomeo, V. Di Cocco, and V. Piacente, "Damaging

micromechanisms in ferritic-pearlitic ductile cast irons,” *Mater. Sci. Eng. A*, vol. 478, no. 1–2, pp. 181–186, 2008, doi: 10.1016/j.msea.2007.05.110.

- [39] J. Lacaze, J. Sertucha, and L. Magnusson Åberg, “Microstructure of as-cast ferritic-pearlitic nodular cast irons,” *ISIJ Int.*, vol. 56, no. 9, pp. 1606–1615, 2016, doi: 10.2355/isijinternational.ISIJINT-2016-108.
- [40] X. R. Chen, Q. J. Zhai, H. Dong, B. H. Dai, and H. Mohrbacher, “Molybdenum alloying in cast iron and steel,” *Adv. Manuf.*, vol. 8, no. 1, pp. 3–14, 2020, doi: 10.1007/s40436-019-00282-1.
- [41] T. Kanno and I. Kang, “Effect of Mn and S on the mechanical properties of gray cast iron,” *71st World Foundry Congr. Adv. Sustain. Foundry, WFC 2014*, vol. 3, no. 5, pp. 81–84, 2014.
- [42] S. Liu, F. Zhang, Z. Yang, M. Wang, and C. Zheng, “Effects of Al and Mn on the formation and properties of nanostructured pearlite in high-carbon steels,” *Mater. Des.*, vol. 93, pp. 73–80, 2016, doi: 10.1016/j.matdes.2015.12.134.
- [43] L. Jiang, R. K. W. Marceau, T. Dorin, P. D. Hodgson, and N. Stanford, “Effect of molybdenum on phase transformation and microstructural evolution of strip cast steels containing niobium,” *J. Mater. Sci.*, vol. 54, no. 2, pp. 1769–1784, 2019, doi: 10.1007/s10853-018-2908-x.
- [44] W. Xu, M. Ferry, and Y. Wang, “Influence of alloying elements on as-cast microstructure and strength of gray iron,” *Mater. Sci. Eng. A*, vol. 390, no. 1–2, pp. 326–333, 2005, doi: 10.1016/j.msea.2004.08.030.
- [45] M. Ferry and W. Xu, “Microstructural and crystallographic features of ausferrite in as-cast gray iron,” *Mater. Charact.*, vol. 53, no. 1, pp. 43–49, 2004, doi: 10.1016/j.matchar.2004.07.008.
- [46] L. Meier, M. Hofmann, P. Saal, W. Volk, and H. Hoffmann, “In-situ measurement of phase transformation kinetics in austempered ductile iron,” *Mater. Charact.*, vol. 85, pp. 124–133, 2013, doi: 10.1016/j.matchar.2013.09.005.

- [47] E. Kozeschnik and H. K. D. H. Bhadeshia, "Influence of silicon on cementite precipitation in steels," *Mater. Sci. Technol.*, vol. 24, no. 3, pp. 343–347, 2008, doi: 10.1179/174328408X275973.
- [48] N. Filonenko and A. Babachenko, "Investigation of Silicon and Manganese Solubility in Cementite of Iron-Based Alloys," *East Eur. J. Phys.*, vol. 51, pp. 46–51, 2019, doi: 10.26565/2312-4334-2019-2-07.
- [49] J. H. Jang, I. G. Kim, and H. K. D. H. Bhadeshia, "Substitutional solution of silicon in cementite: A first-principles study," *Comput. Mater. Sci.*, vol. 44, no. 4, pp. 1319–1326, 2009, doi: 10.1016/j.commatsci.2008.08.022.
- [50] M. Landesberger *et al.*, "Phase transition kinetics in austempered ductile iron (ADI) with regard to MO content," *Materials (Basel)*, vol. 13, no. 22, pp. 1–23, 2020, doi: 10.3390/ma13225266.
- [51] W. C. Cheng and S. M. Hwang, "A eutectoid reaction for the decomposition of austenite into pearlitic lamellae of ferrite and M₂₃C₆ carbide in a Mn-Al steel," *Metall. Mater. Trans. A Phys. Metall. Mater. Sci.*, vol. 42, no. 7, pp. 1760–1766, 2011, doi: 10.1007/s11661-010-0597-4.
- [52] W. C. Cheng and Y. C. Li, "The coexistence of two different pearlites, lamellae of (Ferrite + M₂₃C₆), and lamellae of (Ferrite + M₂₃C₆) in a Mn-Al steel," *Metall. Mater. Trans. A Phys. Metall. Mater. Sci.*, vol. 43, no. 6, pp. 1817–1825, 2012, doi: 10.1007/s11661-011-1051-y.
- [53] B. Wang, G. C. Barber, C. Tao, X. Sun, and X. Ran, "Characteristics of tempering response of austempered ductile iron," *J. Mater. Res. Technol.*, vol. 7, no. 2, pp. 198–202, 2018, doi: 10.1016/j.jmrt.2017.08.011.
- [54] P. Sellamuthu, D. G. H. Samuel, D. Dinakaran, V. P. Premkumar, Z. Li, and S. Seetharaman, "Austempered ductile iron (ADI): Influence of austempering temperature on microstructure, mechanical and wear properties and energy consumption," *Metals (Basel)*, vol. 8, no. 1, 2018, doi: 10.3390/met8010053.

- [55] R. Bendikiene *et al.*, “Influence of austempering temperatures on the microstructure and mechanical properties of austempered ductile cast iron,” *Metals (Basel)*, vol. 11, no. 6, pp. 1–15, 2021, doi: 10.3390/met11060967.
- [56] O. P. Modi, N. Deshmukh, D. P. Mondal, A. K. Jha, A. H. Yegneswaran, and H. K. Khaira, “Effect of interlamellar spacing on the mechanical properties of 0.65% C steel,” *Mater. Charact.*, vol. 46, no. 5, pp. 347–352, 2001, doi: 10.1016/S1044-5803(00)00113-3.
- [57] K. M. Wu and H. K. D. H. Bhadeshia, “Extremely fine pearlite by continuous cooling transformation,” *Scr. Mater.*, vol. 67, no. 1, pp. 53–56, 2012, doi: 10.1016/j.scriptamat.2012.03.019.
- [58] P. Uranga, C. S. Takehide, and S. J. Yang, “Molybdenum alloying in high-performance flat-rolled steel grades,” *Adv. Manuf.*, vol. 8, no. 1, pp. 15–34, 2020, doi: 10.1007/s40436-019-00285-y.
- [59] S. S. Rathore, M. M. Salve, and V. V. Dabhade, “Effect of molybdenum addition on the mechanical properties of sinter-forged Fe-Cu-C alloys,” *J. Alloys Compd.*, vol. 649, pp. 988–995, 2015, doi: 10.1016/j.jallcom.2015.07.156.
- [60] Z. Chen, S. Miao, L. Kong, X. Wei, F. Zhang, and H. Yu, “Effect of mo concentration on the microstructure evolution and properties of high boron cast steel,” *Materials (Basel)*, vol. 13, no. 4, pp. 1–16, 2020, doi: 10.3390/ma13040975.
- [61] G. Hütter, L. Zybell, and M. Kuna, “Micromechanisms of fracture in nodular cast iron: From experimental findings towards modeling strategies - A review,” *Eng. Fract. Mech.*, vol. 144, pp. 118–141, 2015, doi: 10.1016/j.engfracmech.2015.06.042.
- [62] Z. Glavas, A. Strkalj, and A. Stojakovic, “The properties of silicon alloyed ferritic ductile irons,” *Metalurgija*, vol. 55, no. 3, pp. 293–296, 2016.
- [63] J. A. Nemes, “Micromechanical modeling of dual phase steels,” vol. 45, pp. 1449–1465, 2003, doi: 10.1016/j.ijmecsci.2003.10.007.

- [64] Q. Lai *et al.*, “In fl uence of martensite volume fraction and hardness on the plastic behavior of dual-phase steels : Experiments and micromechanical modeling,” pp. 1–17, 2015, doi: 10.1016/j.ijplas.2015.09.006.
- [65] M. Amirmaleki, J. Samei, D. E. Green, I. Van Riemsdijk, and L. Stewart, “Mechanics of Materials 3D micromechanical modeling of dual phase steels using the representative volume element method,” *Mech. Mater.*, vol. 101, pp. 27–39, 2016, doi: 10.1016/j.mechmat.2016.07.011.
- [66] A. H. Jahanara, Y. Mazaheri, and M. Sheikhi, “Materials Science & Engineering A Correlation of ferrite and martensite micromechanical behavior with mechanical properties of ultrafine grained dual phase steels,” *Mater. Sci. Eng. A*, vol. 764, no. March, p. 138206, 2019, doi: 10.1016/j.msea.2019.138206.
- [67] J. Wang, Y. Cheng, Y. Zhang, Z. Yin, X. Hu, and Q. Yuan, “Friction and wear behavior of microwave sintered Al₂O₃/TiC/GPLs ceramic sliding against bearing steel and their cutting performance in dry turning of hardened steel,” *Ceram. Int.*, vol. 43, no. 17, pp. 14827–14835, 2017, doi: 10.1016/j.ceramint.2017.07.231.
- [68] D. Muhammad Nuruzzaman and M. Asaduzzaman Chowdhury, “Effect of Load and Sliding Velocity on Friction Coefficient of Aluminum Sliding Against Different Pin Materials,” *Am. J. Mater. Sci.*, vol. 2, no. 1, pp. 26–31, 2012, doi: 10.5923/j.materials.20120201.05.
- [69] J. F. Archard, “Contact and rubbing of flat surfaces,” *J. Appl. Phys.*, vol. 24, no. 8, pp. 981–988, 1953, doi: 10.1063/1.1721448.
- [70] R. L. Deuis, C. Subramanian, and J. M. Yellupb, “Sliding of Aluminium Composites- a,” *Wear*, vol. 3538, no. 96, pp. 415–435, 1997.
- [71] E. Zdravecká, J. Tkáčová, and M. Ondáč, “Effect of microstructure factors on abrasion resistance of high-strength steels,” *Res. Agric. Eng.*, vol. 60, no. 3, pp. 115–120, 2014, doi: 10.17221/20/2013-rae.
- [72] J. Jiang, F. H. Stott, and M. M. Stack, “The role of triboparticulates in dry sliding

wear,” *Tribol. Int.*, vol. 31, no. 5, pp. 245–256, 1998, doi: 10.1016/S0301-679X(98)00027-9.

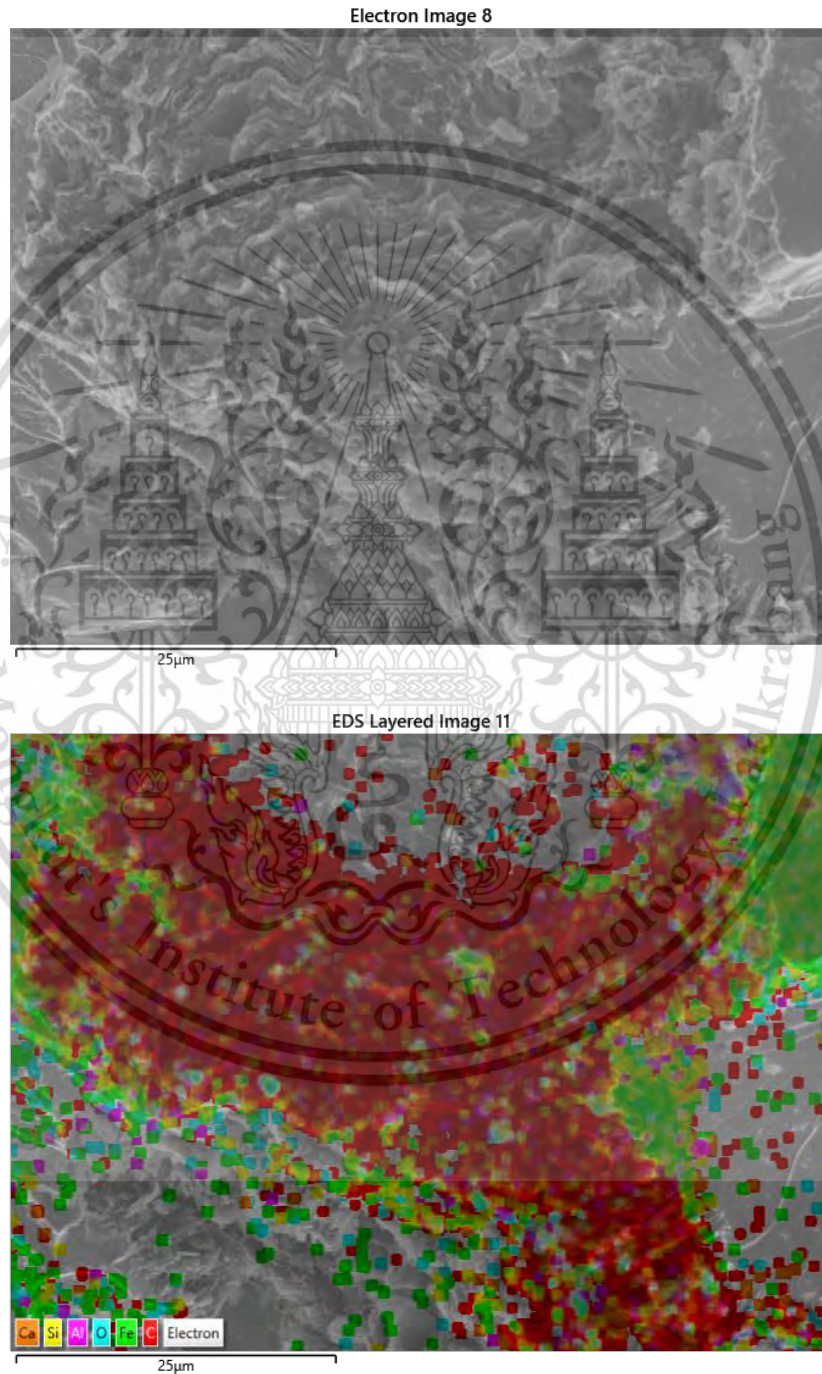
- [73] M. B. N. Shaikh, T. Aziz, S. Arif, A. H. Ansari, P. G. Karagiannidis, and M. Uddin, “Effect of sintering techniques on microstructural, mechanical and tribological properties of Al-SiC composites,” *Surfaces and Interfaces*, vol. 20, p. 100598, 2020, doi: 10.1016/j.surfin.2020.100598.

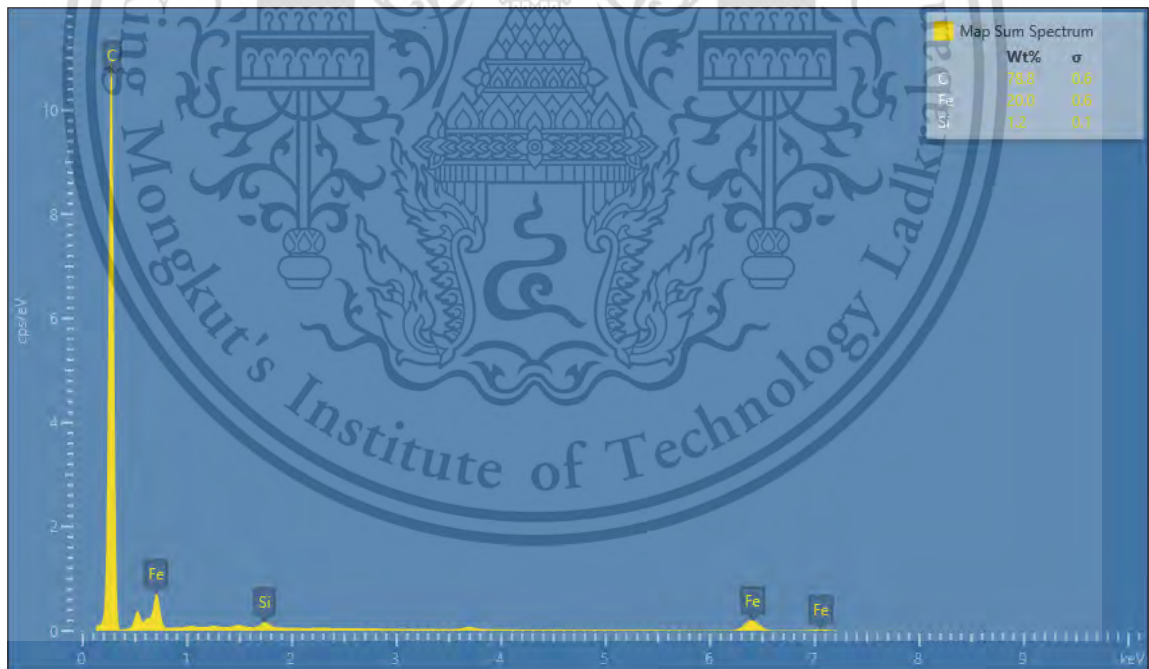
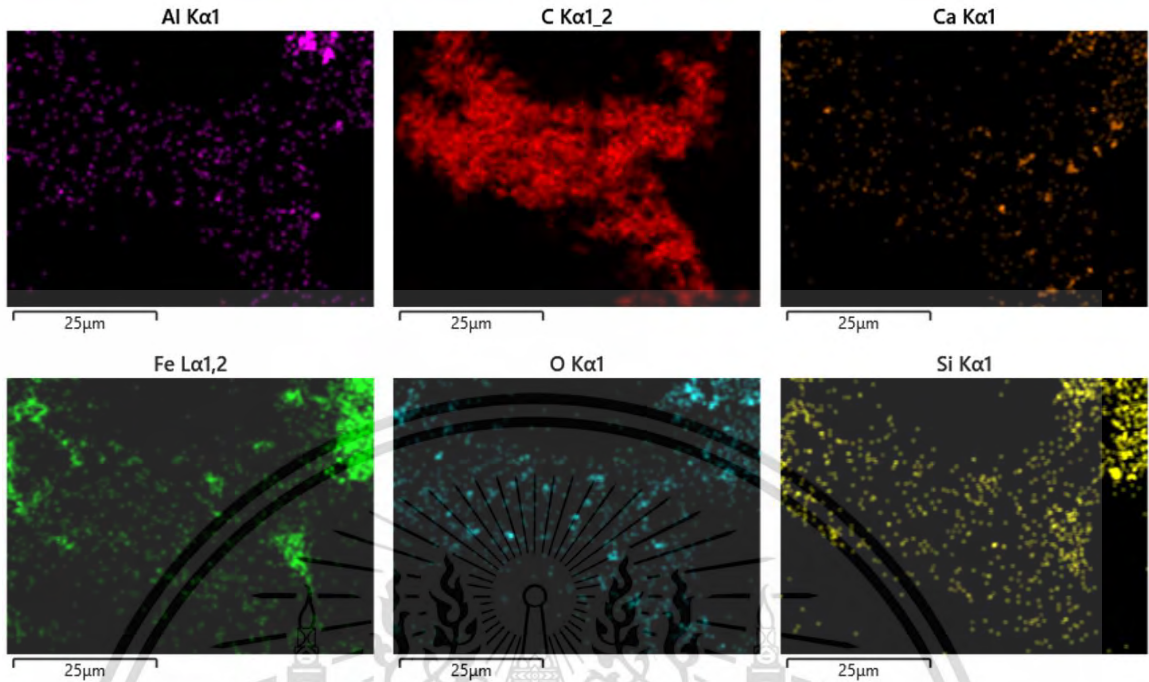


APPENDIX A

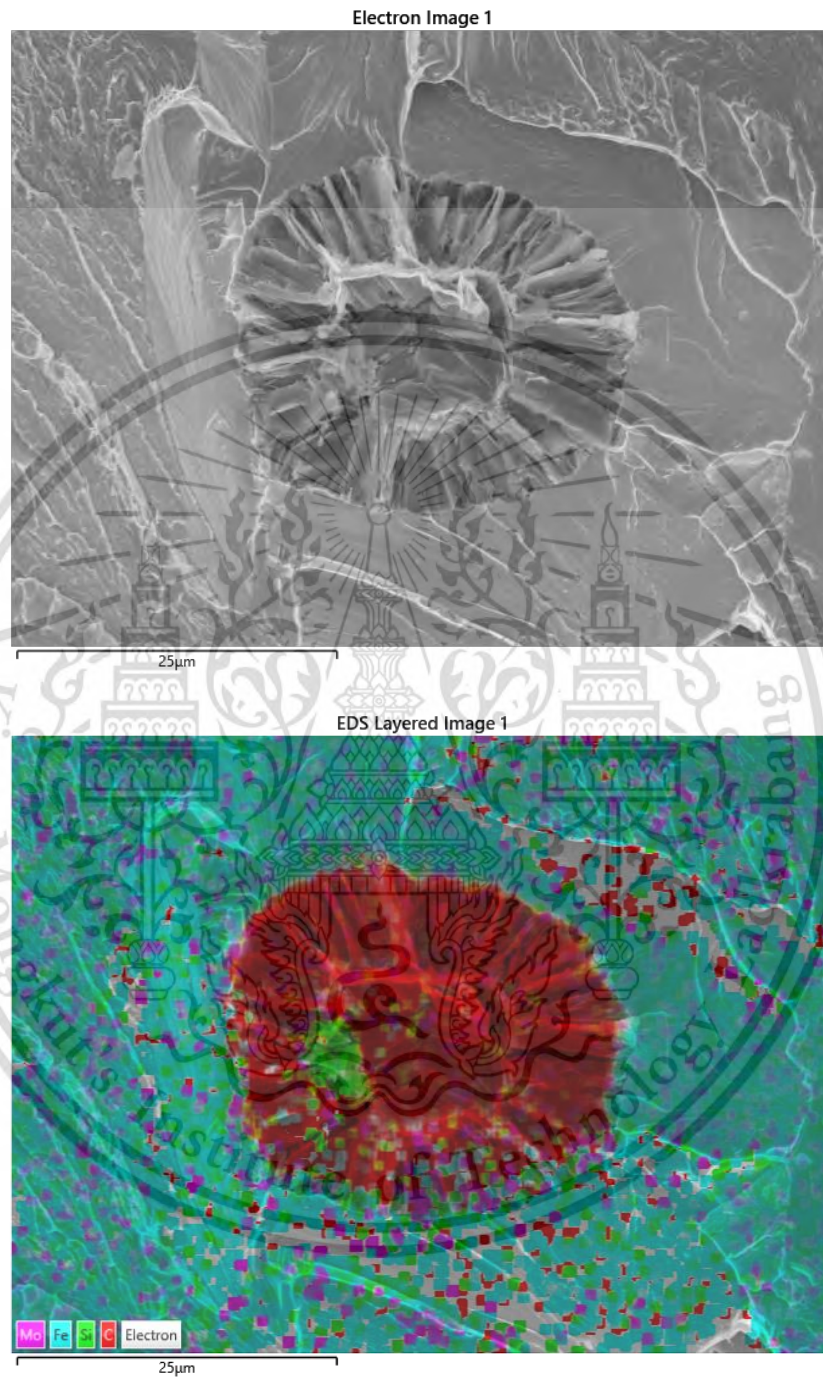
EDS MAPPING AND SPECTRUM ON FRACTURE REPORTS

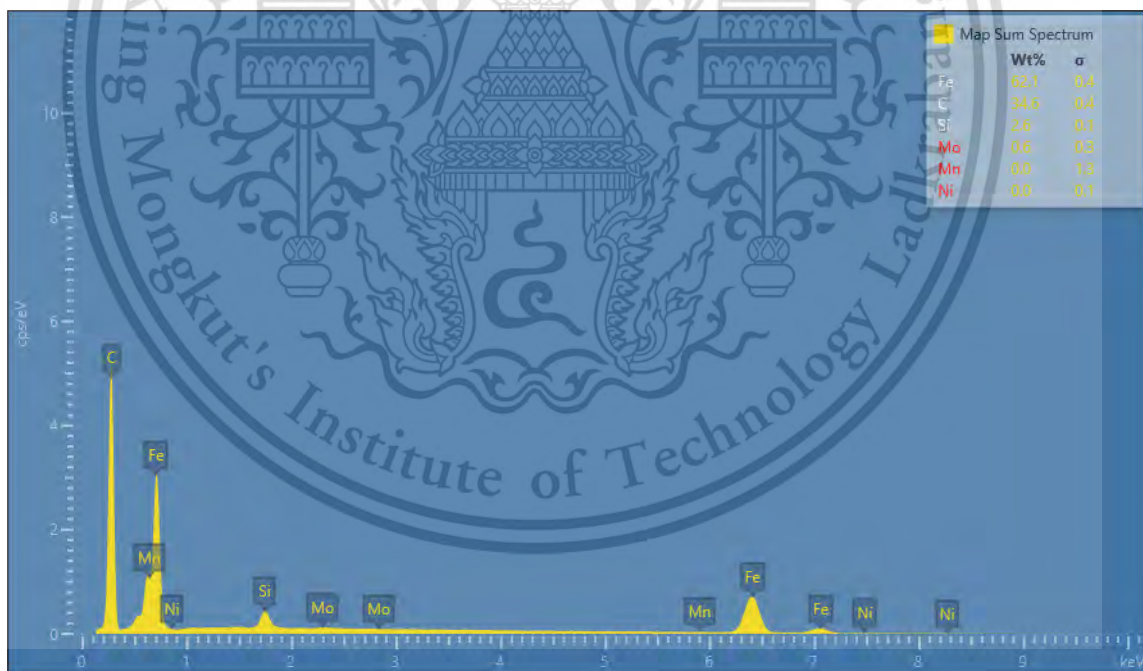
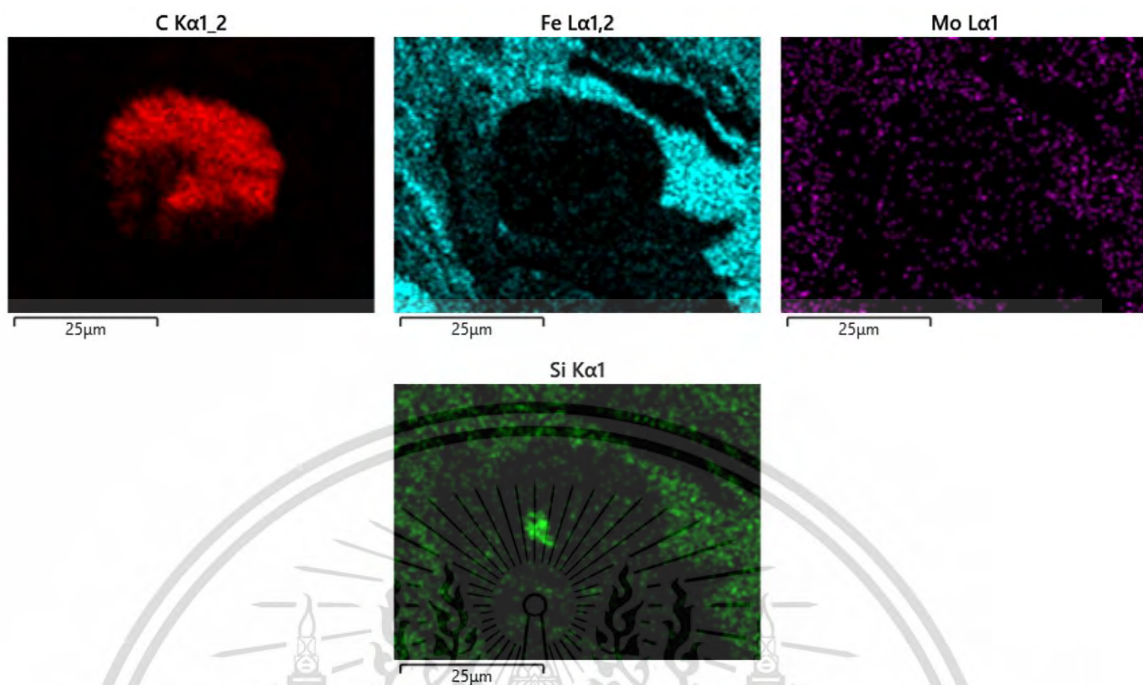
EDS mapping and spectrum on fracture of sintered 0.00Mo composite



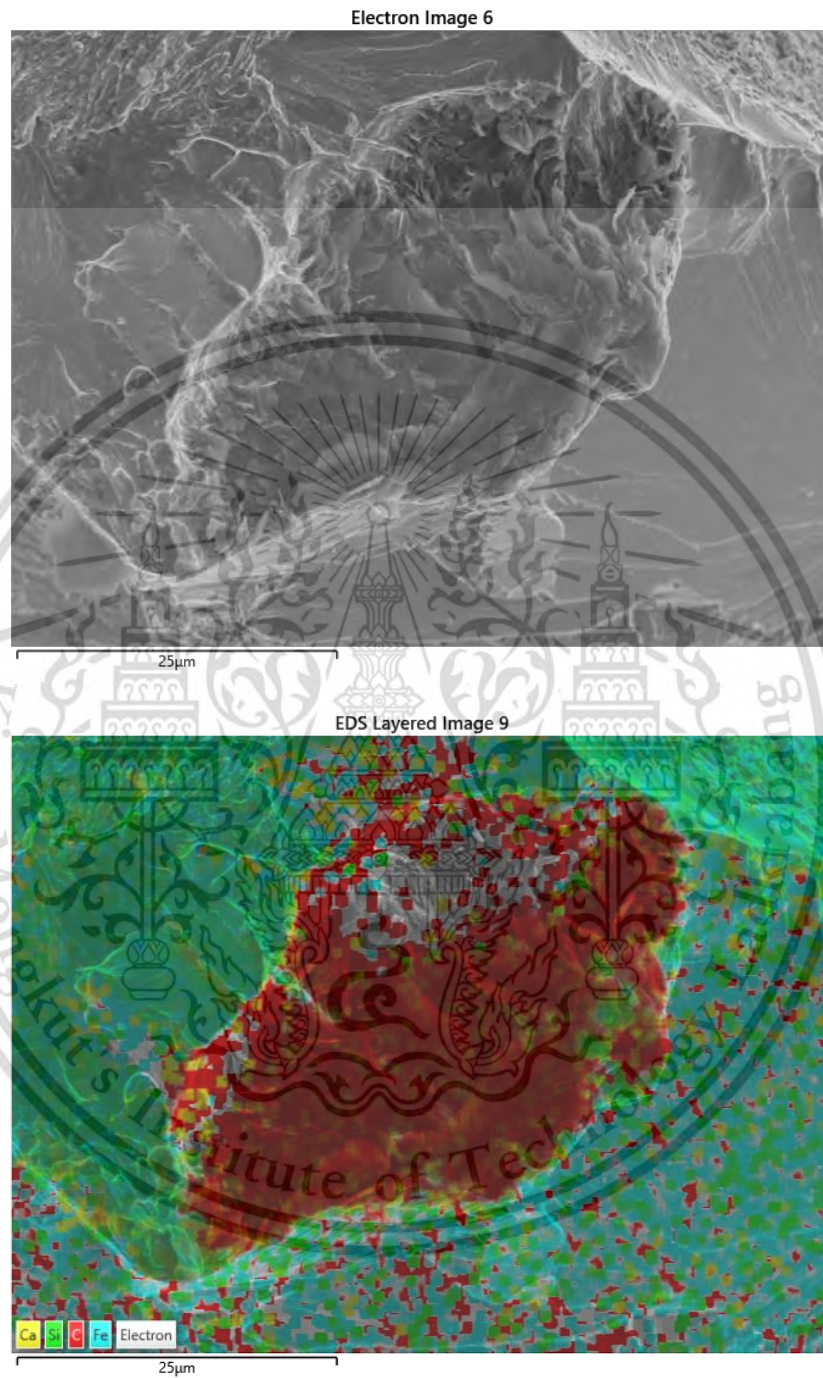


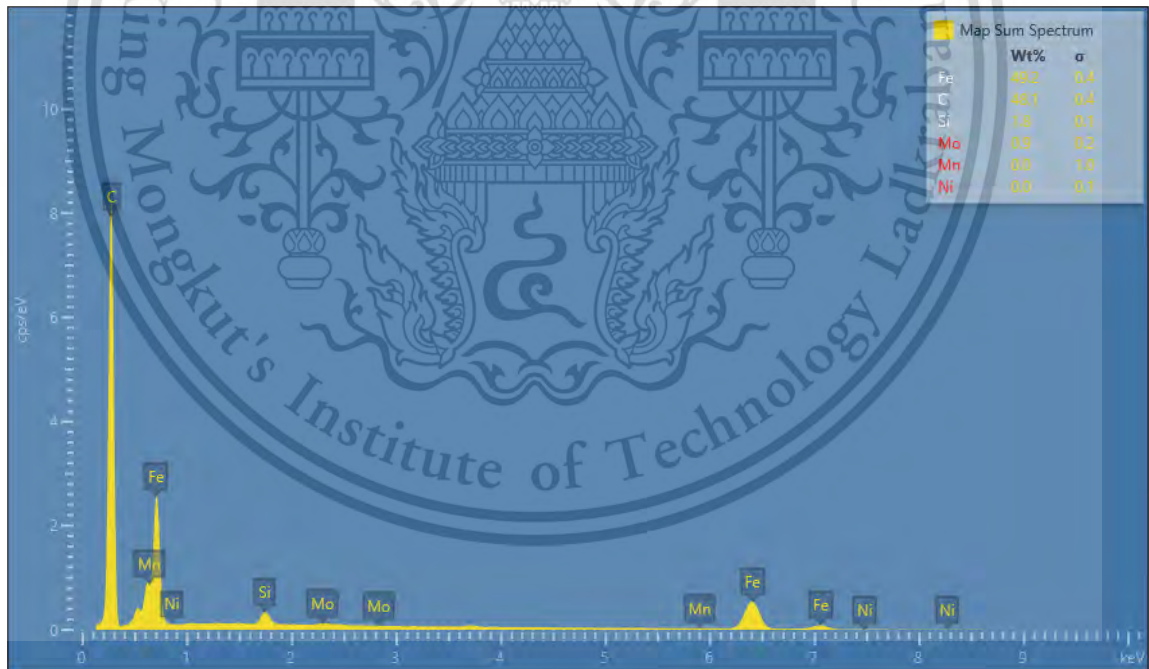
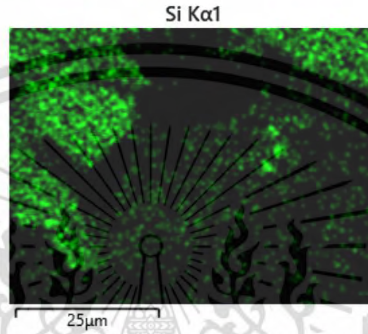
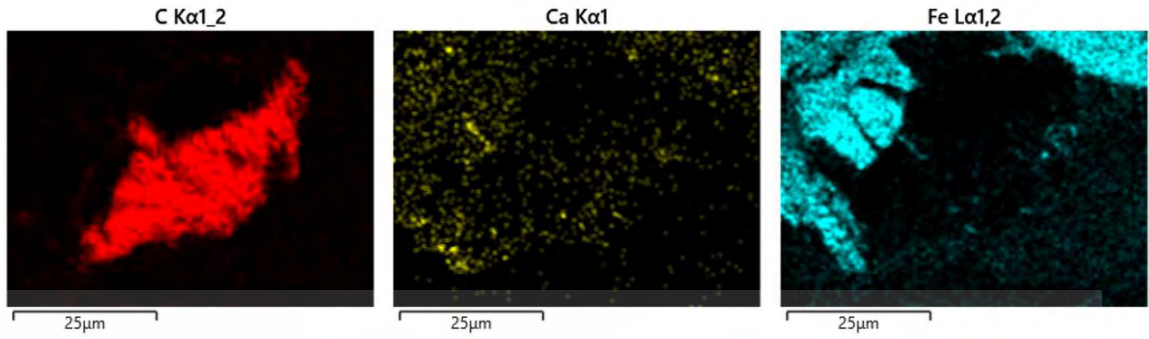
EDS mapping and spectrum on fracture of sintered 0.50Mo composite



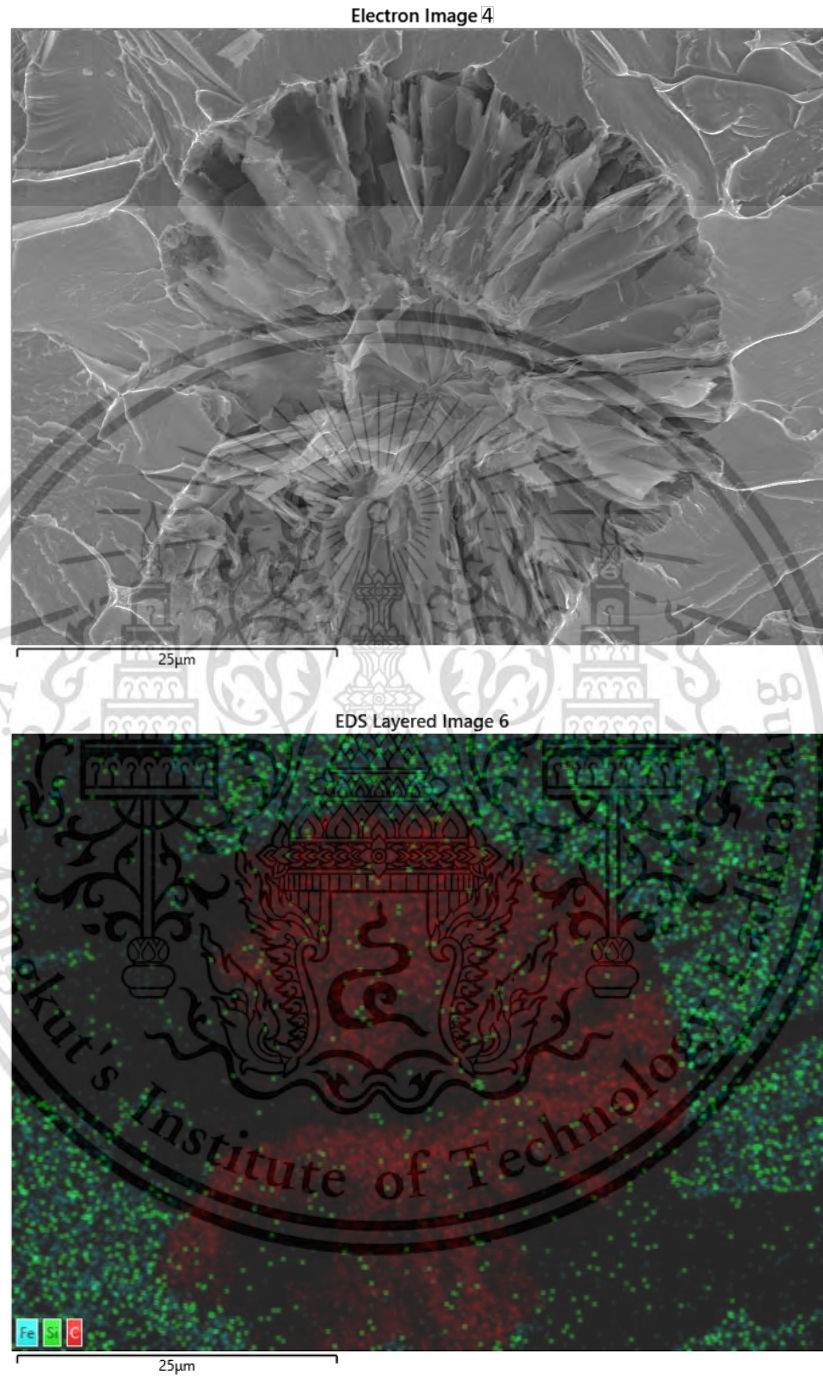


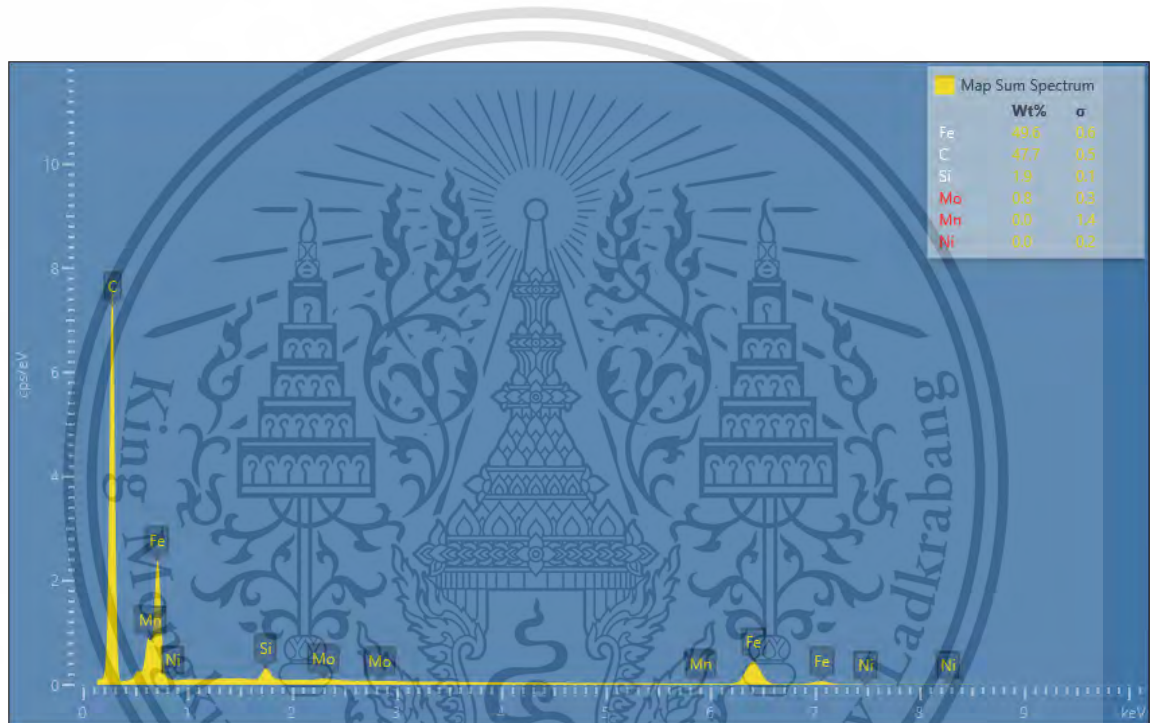
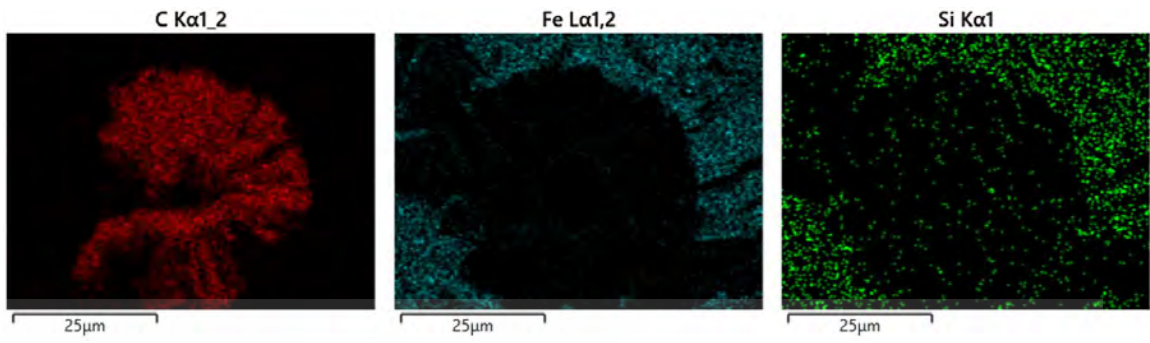
EDS mapping and spectrum on fracture of sintered 0.85Mo composite





EDS mapping and spectrum on fracture of sintered 1.50Mo composite

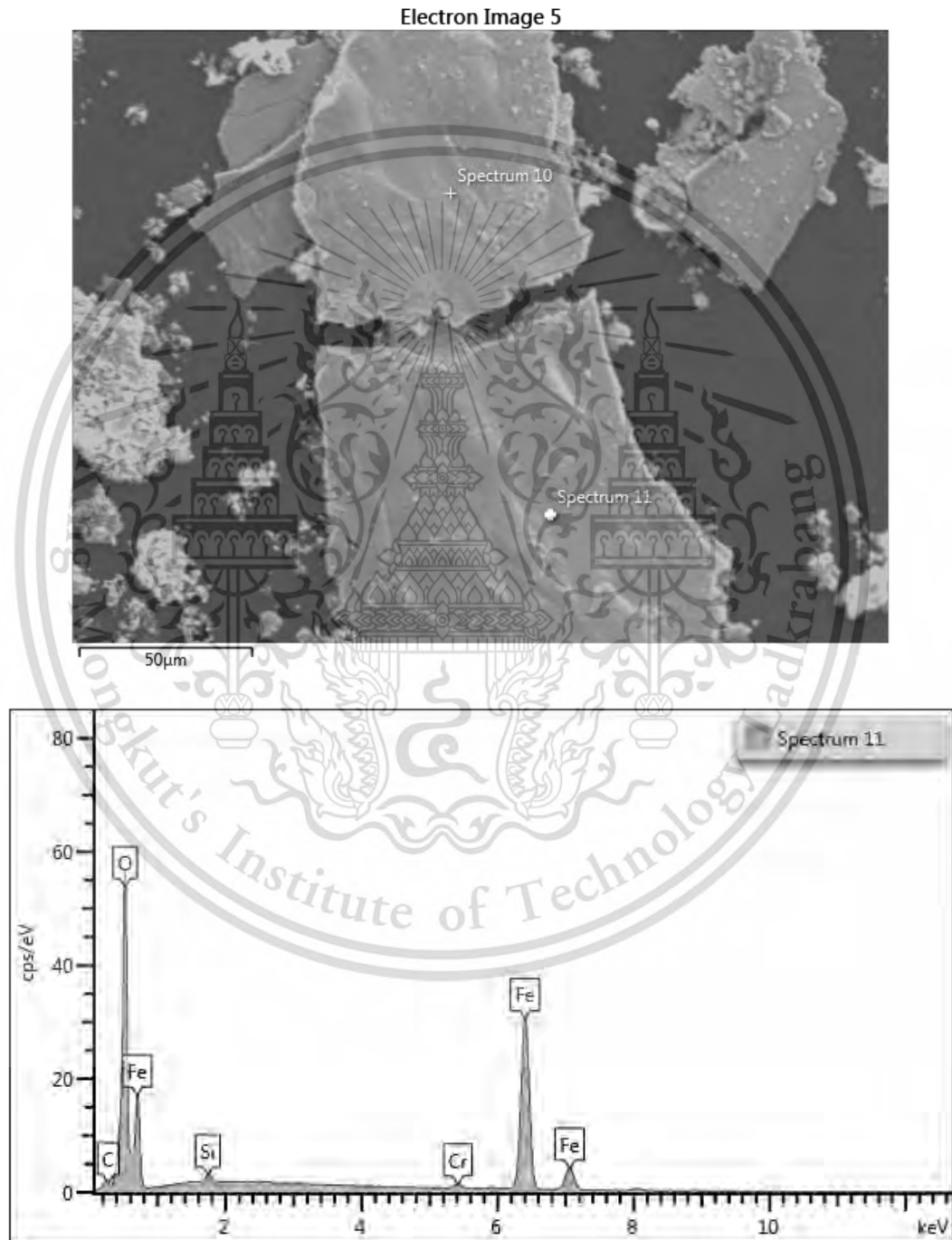




APPENDIX B

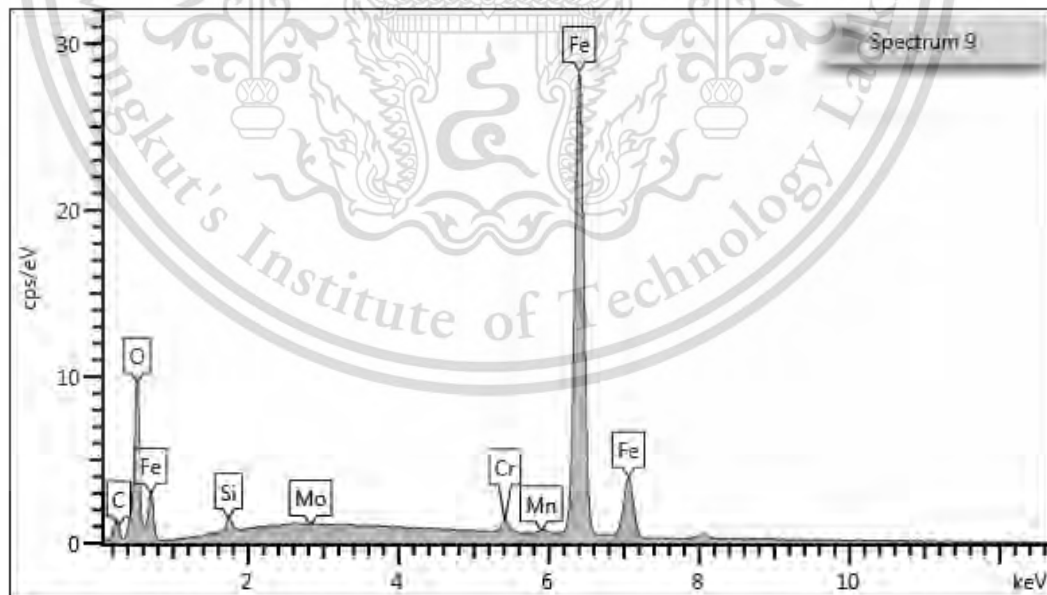
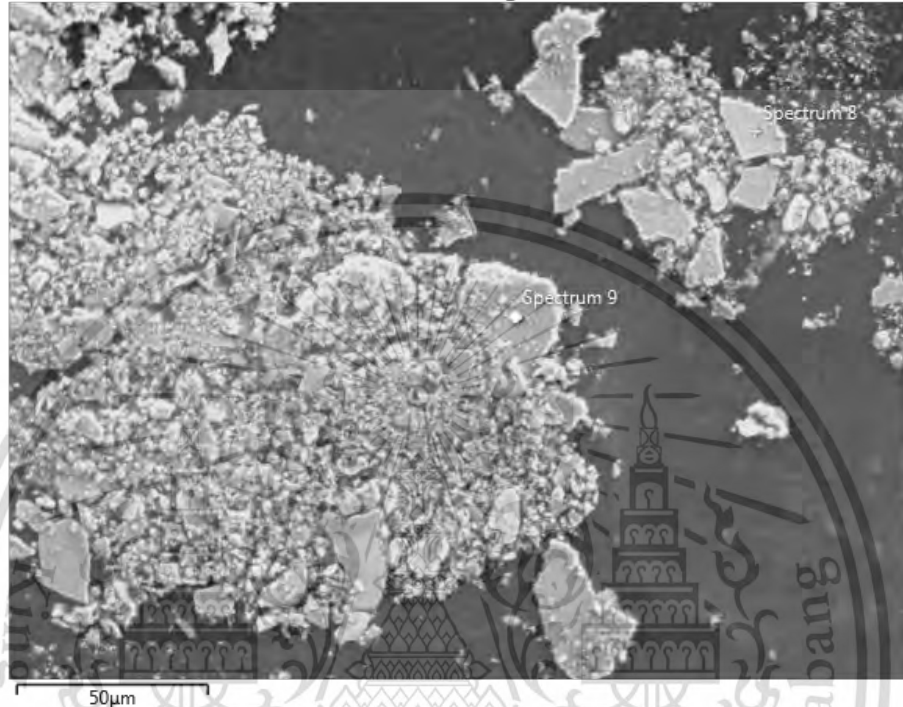
EDS SPECTRUM OF WEAR DEBRIS REPORTS

EDS spectrum of wear debris of sintered 0.00Mo composite

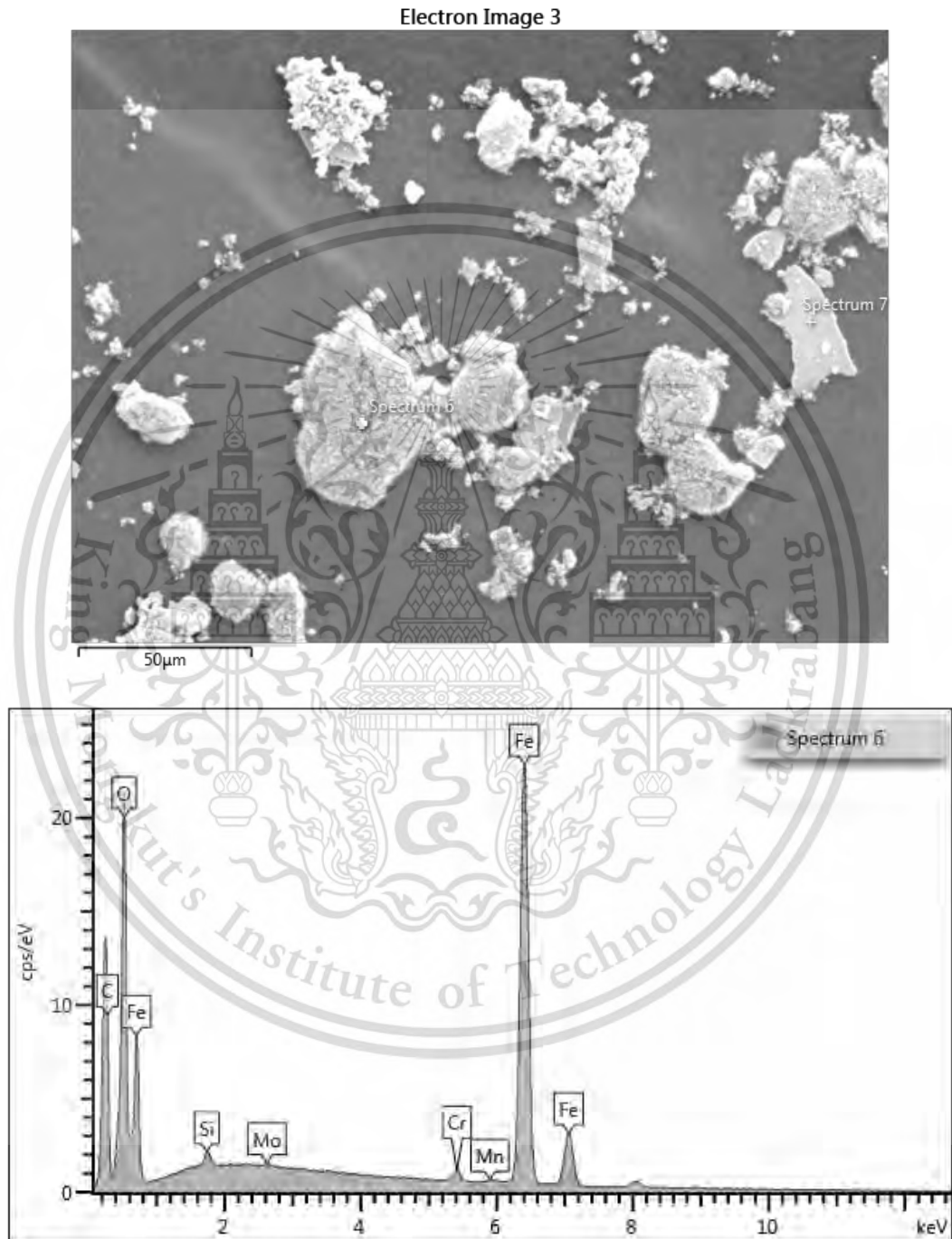


EDS spectrum of wear debris of sintered 0.50Mo composite

Electron Image 4

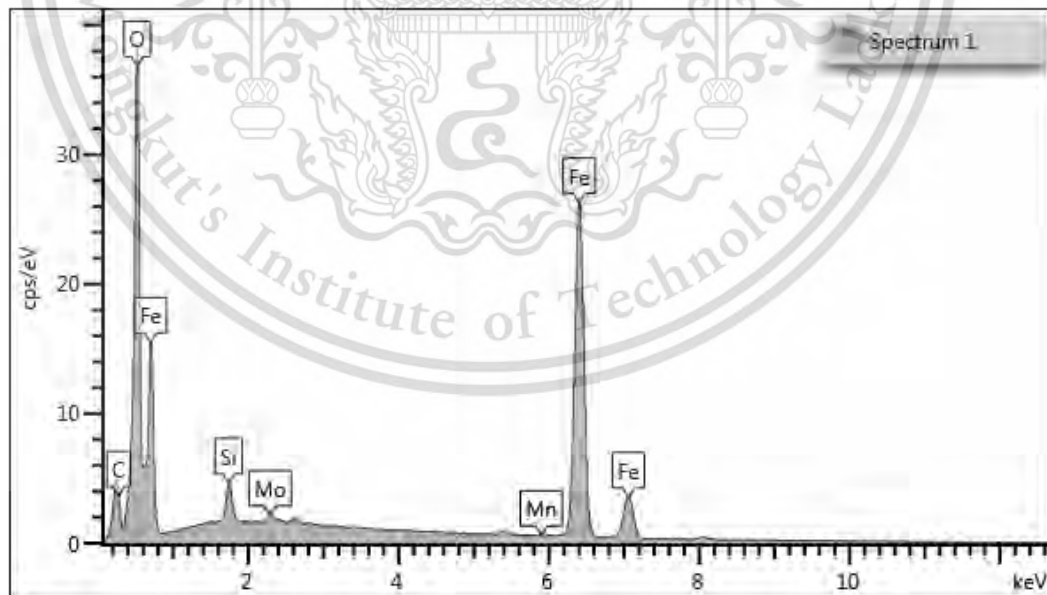
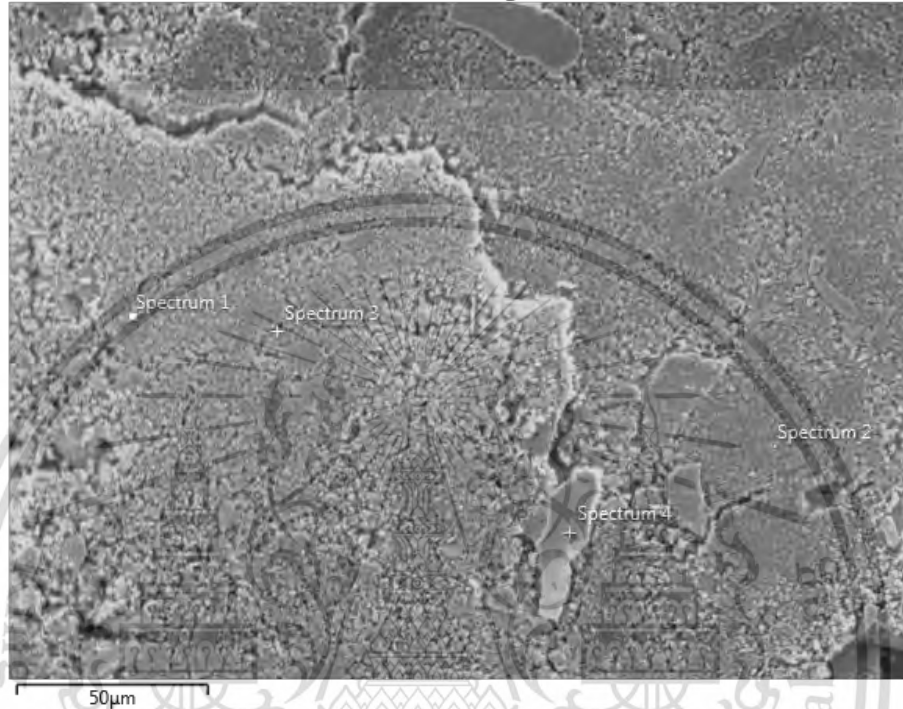


EDS spectrum of wear debris of sintered 0.85 Mo composite



EDS spectrum of wear debris of sintered 1.50 Mo composite

Electron Image 1



APPENDIX C

PUBLICATION

IOP Publishing
Scopus[®]
TCI

11th

Thai Society of Mechanical
Engineering, International Conference
on Mechanical Engineering (TSME-ICoME 2020)

December 1 – 4, 2020
Ubon Ratchathani,
Thailand

Welcome to The 11th Thai Society of Mechanical Engineering, International Conference on Mechanical Engineering (TSME-ICoME 2020).
It is our great pleasure to invite you to the TSME-ICoME 2020 which will be held in the most attractive city of Ubon Ratchathani (Thailand) during December 1-4, 2020.
The conference is organized by the Thai Society of Mechanical Engineers (TSME) that aims to bring together leading scientists, researchers and research scholars to exchange and share their experiences and research results in the field of Mechanical Engineering. You will walk away with new perspectives, concrete ways to shape a better future and a brand-new group of collaborators.

Conference Topics

- Alternative Energy and Combustion (AEC)
- Automotive, Aerospace and Marine Engineering (AME)
- Applied Mechanics, Materials and Manufacturing (AMM)
- Biomechanics and Bioengineering (BME)
- Computation and Simulation Techniques (CST)
- Dynamic Systems, Robotics and Controls (DRC)
- Engineering Education (EDU)
- Energy Technology and Management (ETM)
- Thermal System and Fluid Mechanics (TSF)

Organizing Committees

- Honorary chair: *President of Thai Society of Mechanical Engineers (TSME)*
- General conference Co-Chairs: *Asst. Prof. Prachasani Thaiyasuit*
- General conference secretariat: *Assoc. Prof. Thanarath Sriveerakul*

Important Dates

- Abstract Submission: March 15 - April 30, 2020
- Abstract Acceptance Notification: May 11, 2020
- Full Manuscript Submission: May 11 - August 31, 2020
- Full Manuscript Acceptance Notification: October 30, 2020
- Camera-Ready Manuscript Submission Deadline: October 10, 2020
- Early-bird Registration: October 1 - 17, 2020
- Conference Date: December 1 - 4, 2020

Department of Mechanical Engineering, Faculty of Engineering, Ubon Ratchathani University
85 Sathonlamark Rd. Warin Chamrap, Ubon Ratchathani 34190 THAILAND
Tel: +66 45 353323 Fax: +66 45 353308
Email: tsme-icome2020@ubu.ac.th

Challenging Trends in Mechanical Engineering for 2020 and Beyond

TSME-ICoME 2020: Challenging Trends in Mechanical Engineering for 2020 and Beyond

PAPER • OPEN ACCESS

The effect of molybdenum on the microstructure and mechanical behaviour of the sintered Fe-Mo-Mn-Si-C composite

To cite this article: Thunyamon Nithimethakul et al 2021 *IOP Conf. Ser.: Mater. Sci. Eng.* **1137** 012028

View the [article online](#) for updates and enhancements.



An advertisement for a virtual education course. On the left, the ECS logo is shown with the text 'The Electrochemical Society' and 'Advancing solid state & electrochemical science & technology'. Below this, it says '2021 Virtual Education' and 'Fundamentals of Electrochemistry: Basic Theory and Kinetic Methods'. The instructor is listed as 'Dr. James Noël' and the course dates are 'Sun, Sept 19 & Mon, Sept 20 at 12h-15h ET'. A red button says 'Register early and save!'. On the right, there is a photograph of an open book and a laptop on a desk in front of a chalkboard.

This content was downloaded from IP address 1.47.29.157 on 22/07/2021 at 16:19

The effect of molybdenum on the microstructure and mechanical behaviour of the sintered Fe-Mo-Mn-Si-C composite

Thunyamon Nithimethakul¹, Preechar Karin¹, Naoto Ohtake², Pongsak Wila³,
Thanyaporn Yodkaew³, Bhanu Vetayanugul^{3*}, Monnapas Morakotjinda³, and
Ruangdaj Tongsri²

¹School of Engineering, King Mongkut's Institute of Technology Ladkrabang,
Chalongkrung Road, Ladkrabang, Bangkok 10520, Thailand.

²Department of Mechanical Engineering, Major in Engineering Sciences and Design,
Tokyo Institute of Technology, Tokyo, 152-8550, Japan.

³Particulate Materials Processing Technology (PMPT), National Metal and Materials
Technology Center, 114 Paholyothin Road, Khlong Nueng, Khlong Luang,
Pathumthani 12120, Thailand.

* Corresponding Author: bhanuv@mtec.or.th

Abstract

Experimental sintered Fe-Mo-Mn-Si-C composites were prepared from 3 different pre-alloyed Fe-Mo-Mn powders, namely Fe-0.50Mo-0.15Mn, Fe-0.85Mo-0.15Mn and Fe-1.50Mo-0.15Mn, mixed with fixed 4 wt.% silicon carbide powder. Sintered Fe-SiC composite was also prepared, as a reference material, from pure Fe powder mixed with fixed 4 wt.% silicon carbide powder. All specimens were processed by using the 'press and sinter' method. Sintering was performed in a vacuum furnace at 1250°C for 45 minutes and slow cooling in the furnace. The microstructures of most sintered alloys showed a common feature consisting of a black particle enveloped with ferrite and pearlite. Sintered composites produced from high-molybdenum powders showed different matrices, in which some pearlite regions were replaced by BF/M-A structures. The Tensile and hardness test showed that the sintered alloys exhibited an increase of tensile strength, yield strength, and hardness with increasing molybdenum content. The pearlite → BF/M-A fractions of sintered composites played important roles in material strengthening. In the sintered composites produced from high-molybdenum powders, the carbide-free BF/M-A structure showed a promising strengthening effect.

Keywords: Sintering, Fe-Mo-Mn-Si-C, Pearlite, Carbide-free bainite, Mechanical property.

1. Introduction

The traditional process of 'press and sinter' is commonly used for producing particulate-reinforcement composites. The early attempts to produce silicon carbide (SiC)-reinforced metal matrix composites (MMCs) revealed that interfacial reaction between SiC and iron-base matrix occurred during heating and sintering [1-3]. In 316L/SiC system [1], interfacial reaction resulted in intergranular liquid phase formation. In Fe/SiC system [2, 3], SiC residual particle was enveloped with ferrite-pearlite matrix. Later, pre-alloyed powders, such as Fe-Mo [4] and Fe-Cr-Mo [5] powders, and diffusion bonded

powders [6], were employed as matrices. The final microstructures of sintered composites strongly depended on pre-alloyed powder composition. In the Fe-Mo/SiC systems [4], ductile iron-like microstructure consisting of black (graphite-containing) particle surrounded with ferrite-pearlite matrix was a common microstructural feature. In the Fe-Cr-Mo/SiC systems [5], pearlitic ductile iron-like microstructure was obtained. In the diffusion bonded powders added with SiC systems [6], the matrices surrounding black particles contained bainite instead of pearlite.

These sintered composites based on pre-alloyed powders [4-5] showed promising tensile properties and had graphite-containing particles embedded in their matrices. The formation of graphite-containing particles is attributed to SiC decomposition, interfacial reaction, melting and re-solidification in SiC site vicinities. The interactions between SiC and iron-base powder particles was given by experimental evidence [7]. These interactions were also considered by thermodynamic models as given in [8, 9].

The materials consisting of graphite-containing particles embedded in iron base matrices are classified as self-lubricating composites due to lubricity of graphite [10-12]. The self-lubricating composites containing graphite particles are commonly applied as train brake linings [13,14]. Definitely, tribological properties of self-lubricating composites or brakes pads depend on lubricant characteristics [15, 16]. However, according to the recent study [17], the matrix of train brake linings plays an important role on braking performance, such as stable coefficient of friction (COF) and wear rate. To have such good braking performance, the brake matrix should have mechanical properties as good as tribological properties.

Thus, the sintered composites, having graphite-containing particles embedded in iron-based matrices, have potential for applications as train brake linings. This present work focuses on the influence of molybdenum content in pre-alloyed powders, used for making composite matrices, on mechanical properties of sintered composites. Pure iron powder was also used for producing a sintered composite as the reference material.

2. Materials and Methods

2.1 Specimen Preparation

Sintered composites were prepared from 4 different metal powders, including pure iron (Fe) and 3 pre-alloyed Fe-Mo powders, mixed with fixed 4 wt.% silicon carbide powder and 1 wt.% zinc stearate as a lubricant. The nominal compositions of experimental sintered composites are given in Table 1. Specimen preparation procedure included cold pressing and the sintering of powder mixture compacts. Green specimens were produced by compacting powder mixtures into standard tensile test bars (MPIF standard 10) with green density of 6.50 ± 0.01 g/cm³. Green compacts were sintered at 1250°C for 45 minutes in a vacuum atmosphere. After sintering, the specimens were slowly cooled in the sintering furnace.

2.2 Hardness and tensile tests

Rockwell scale B (HRB) hardness test, with ball diameter of 1/16 inch and 100 kgf load, was used to measure the hardness of each specimen. This test was carried out on un-etched surface of a specimen. Five indentations on each sintered composite were pressed for obtaining a mean hardness value. For tensile test, sintered composites were tensioned at room temperature by using Instron 8801 Universal Instrument with load cell of 100kN and speed of 1 mm/min. Three specimens of sintered composite were tested for obtaining average the tensile properties.

2.3 Microstructure Observation

Microstructures of sintered composites were observed by optical microscopy (OM) and scanning electron microscopy (SEM) equipped with energy-dispersive X-ray spectroscopy (EDS). A surface of a specimen was abraded on silicon carbide grit papers to number 4000 and then polished with 6, 3, and 1 μ m diamond pastes. The polished samples were etched with 2% Nital and cleaned by ethanol. The SEM was operated at 20 kV to observe the details of microstructure. Phase identification was carried out by using X-ray diffraction (XRD) technique.

Table 1. Nominal composition of experimental sintered composites

Composite	Metal powder	SiC (wt. %)	Composite nominal composition (wt. %)				
			C	Si	Mo	Mn	Fe
0.00Mo	Fe	4.0	1.20	2.80	0.00	0.00	Bal.
0.50Mo	Fe-0.5Mo-0.15Mn	4.0	1.20	2.80	0.48	0.14	Bal.
0.85Mo	Fe-0.85Mo-0.15Mn	4.0	1.20	2.80	0.82	0.14	Bal.
1.50Mo	Fe-1.5Mo-0.15Mn	4.0	1.20	2.80	1.44	0.14	Bal.

3. Results and Discussion

3.1 Microstructure

All experimental sintered composites exhibited common microstructural features consisting of black particle(s) surrounded with white and dark areas (Figure 1). The black particles had different shapes from irregular to spherical ones. They were identified as graphite-containing particles. The white area contained polygonal ferrite grains the forms of halos around black particles. The dark area was revealed by SEM (Figure 2) to contain a pearlite structure and bainitic ferrite (BF) and martensite-austenite (M-A) constituent. The BF/M-A structure with no carbide precipitation was observed in sintered composites with high molybdenum contents (sintered 0.85Mo and 1.50Mo composites). Area fractions of microstructural components in sintered composites were measured and presented in Table 2.

The microstructural features as shown in Figure 1 resemble those of sintered composites [3,4, 10-12] and of ferritic-pearlitic ductile irons [17, 18]. The formation of ductile iron-like microstructure was briefly explained in [4]. The conditions, under which ferrite and pearlite transformations occur in ductile irons, are also explained in [19]. Discussion on such issues is not repeated here but the attention is focused on the molybdenum effect on the sintered composite matrix feature.

Pearlite structures are found in all experimental sintered composites produced under slow continuous cooling. The existence of a pearlite structure indicates that cementite (Fe_3C) precipitation does form at high temperatures, under which substitutional alloying elements (silicon and molybdenum) are possible to undergo partitioning. XRD patterns given in Figure 3 show strong peaks corresponding to α -iron or ferrite (labelled) and weak peaks corresponding to cementite (not labelled). Other alloy carbides are not detected by XRD. This suggests that the partitioning of silicon from cementite to ferrite occurs to favor cementite precipitation and hence pearlite transformation. It is well-known that silicon retards the precipitation of cementite from different parent materials or phases, such as cast irons, martensite and austenite [20]. This is due to the fact that silicon has low solubility in cementite (Fe_3C), i.e., up to 4.5 at. % Si [21]. Theoretical study suggests that the formation of $(FeSi)_3C$ carbide is associated with high formation energy [22], which is not thermodynamically favored.

In the sintered composites with high molybdenum contents, such as sintered 0.85Mo and 1.50Mo composites, the BF/M-A structure forms at low temperatures. The BF/M-A formation is strongly under the influence of molybdenum. Under continuous cooling, molybdenum additionally retards ferrite and pearlite transformations by shifting the corresponding transformation fields to lower cooling rates [23, 24]. The delay of high-temperature transformations opens up the window for low-temperature transformations even under a slow cooling. The BF/M-A constituent contains no carbide particles. This indicates that carbide precipitation retardation occurs at low temperatures in such sintered composites.

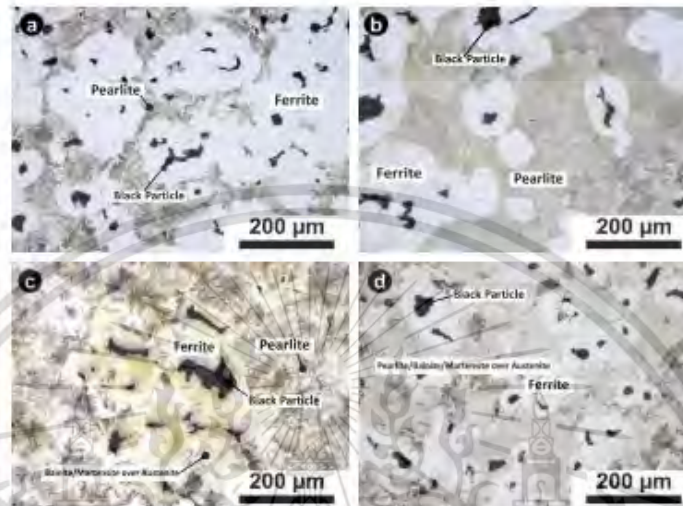


Figure 1. Optical micrograph of sintered composites (a) 0.00Mo composite, (b) 0.50Mo composite, (c) 0.85Mo composite, and (d) 1.50Mo composite.

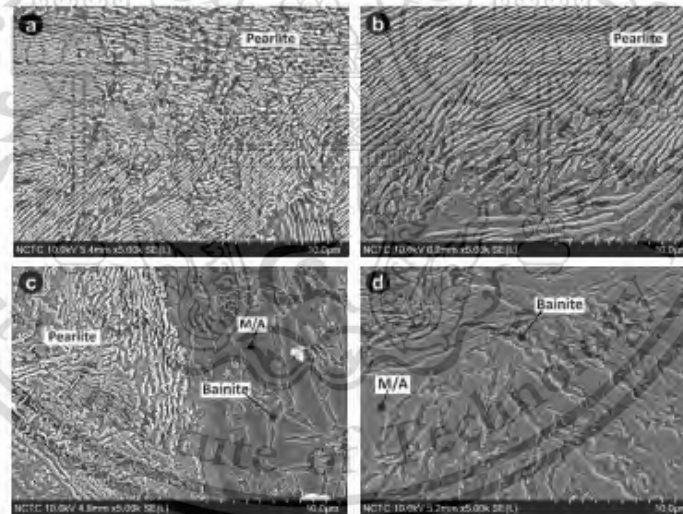
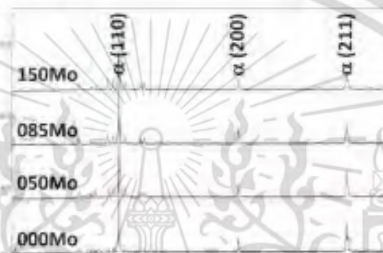


Figure 2. SEM micrographs of sintered composites (a) 0.00Mo composite, (b) 0.50Mo composite, (c) 0.85Mo composite, and (d) 1.50Mo composite.

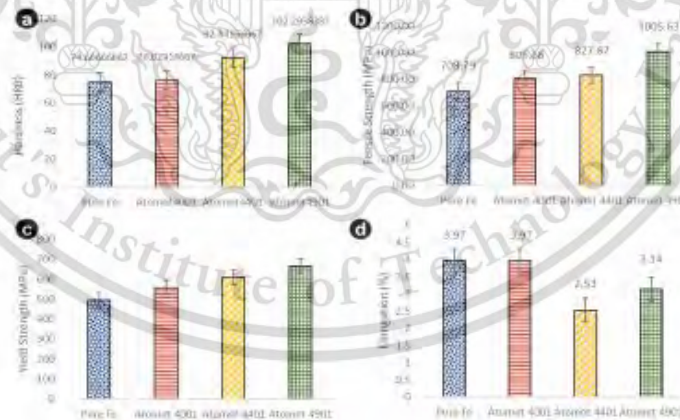
Table 2. Total area of each phase of sintered materials.

Composite	Area fraction (%)		
	Black particle	Ferrite	Pearlite + BF/M-A
0.00Mo	3.8	66.2	30.0
0.50Mo	8.5	36.1	55.4
0.85Mo	19.0	23.2	57.8
1.50Mo	19.0	8.5	72.5

**Figure 3.** XRD patterns of the sintered composites.

3.2 Mechanical property

The Tensile strength and hardness of sintered composites increased with increasing molybdenum content while the values of elongation at break were in the range of 2.5-4.0 % (Figure 4). The strength and hardness of sintered composites depends strongly on pearlite + BF/M-A fractions, which are promoted by high molybdenum content. The fraction of soft phase or ferrite is supposed to dictate ductility of sintered composites, but experimental results do not give any evidences to support such a concept.

**Figure 4.** Mechanical properties of the sintered composites; (a) hardness, (b) ultimate tensile strength, (c) yield strength, (d) elongation at break

4. Conclusion

The influences of molybdenum on microstructure and mechanical property of sintered composites were investigated and the conclusions were drawn as given below.

- 1) General microstructures of sintered composites resembled those of ferrite-pearlite ductile irons.
- 2) Molybdenum retards ferrite and pearlite transformations and promotes BF/M-A formation.
- 3) Strength and hardness of sintered composites are influenced by pearlite + BF/M-A fraction.

Acknowledgments

This work was funded by the project P1951261 supported by National Science and Technology Development Agency (NSTDA). The first author is also financially supported by TAIST-Tokyo Tech scholarship. The authors are grateful for supports from Thailand National Metal and Materials Technology Center (MTEC) and King Mongkut's Institute of Technology Ladkrabung (KMITL). The authors are also grateful for the material for this research, courtesy from Rio Tinto Metal Powders of Canada (via P.S. Steel Co., Ltd., of Thailand and Rio Tinto Iron & Titanium (Suzhou) Co., Ltd., of China).

References

- [1] Coovattanachai O Mima S Yodkaew T Krataitong R Morakotjinda M Daraphan A Tosangthum N Vetayanugul B Panumas A Poolthong N and Tongsri R 2006 *Proc. 2006 Int. Conf. Powder Metall. Part. Mater. PowderMet* 7161-7171
- [2] Yodkaew T Morakotjinda M Tosangthum N Coovattanachai O Krataitong R Siriphol P Vetayanugul B Chakthin S and Poolthong N 2008 *J. Met. Mater. Miner.* **18** 57-61
- [3] Chakthin S Poolthong N and Tongsri R 2008 *Adv. Mater. Res.* **55-57** 357-360
- [4] Ruangchai K Wiengmoon A Morakotjinda M Tosangthum N and Tongsri R 2018 *J. Phys. Conf. Ser.* **1144** 012099
- [5] Ruangchai K Wiengmoon A Krataitong R Yodkaew T Tosangthum N and Tongsri R 2018 *J. Phys. Conf. Ser.* **1144** 012147
- [6] Szewczyk-nykiel A 2017 *Czas. Tech.* **6** 179-190
- [7] Tongsri R and Vetayanugul B 2010 *J. Met. Mater. Miner.* **20** 45-49
- [8] Klein A N Furlan K P Schroeder R M Hammes G Binder C Rodrigues Neto J B Probst S H and de Mello J D B 2015 *Powder Technol.* **271** 193-203
- [9] Araya N Neves G O Filho A R Aguilar C Biasoli de Mello J D Binder C Klein A N and Hammes G 2020 *Mater. Chem. Phys.* **253** 123442
- [10] Araya N I Binder C Klein A N Hammes G De Mello J D B and Aguilar C 2018 *Mater. Res.* **21** 1-10
- [11] Binder C Bendo T Hammes G Neves G O Binder R de Mello J D B and Klein A N 2017 *Carbon N. Y.* **124** 685-692
- [12] De Mello J D B Binder C Hammes G Binder R and Klein A N 2017 *Friction* **5** 285-307
- [13] Günay M Korkmaz M E and Özmen R 2020 *Eng. Sci. Technol. an Int. J.* **23** 421-431
- [14] Wang X and Ru H 2019 *Materials (Basel)* **12**(2) 313
- [15] Chen B Bi Q Yang J Xia Y and Hao J 2008 *Tribol. Int.* **41** 1145-1152
- [16] Peng T Yan Q Li G, Zhang X Wen Z and Jin X 2017 *Tribol. Lett.* **65** 1-13
- [17] Peng T Yan Q and Zhang X 2018 *Tribol. Lett.* **66** 1-13
- [18] Iacoviello F Di Bartolomeo O Di Cocco V and Piacente V 2008 *Mater. Sci. Eng. A* **478** 181-186
- [19] Lacaze J Sertucha J and Magnusson Åberg L 2016 *ISIJ Int.* **56** 1606-1615
- [20] Kozeschnik E and Bhadeshia H K D H 2008 *Mater. Sci. Technol.* **24** 343-347
- [21] Filonenko N and Babachenko A 2019 *East Eur. J. Phys.* **51** 46-51
- [22] Jang J H Kim I G and Bhadeshia H K D H 2009 *Comput. Mater. Sci.* **44** 1319-1326
- [23] Ackermann M Resiak B Buessler P Michaut B and Bleck W 2020 *Steel Res. Int.* **1900663** 1-9
- [24] Hamula J Porter D Kajjalainen A Somani M and Kömi J 2019 *Metals (Basel)* **9**(3) 350

AUTHOR BIOGRAPHY

Author: Ms. Thunyamon Nithimethakul

Degree: Master of Engineering

Date of Graduation: 30th July 2021

Date of Birth: 15th July 1996

Place of Birth: Bangkok, Thailand

Undergraduate and Graduate Education:

Master of Engineering in Automotive Engineering,
King Mongkut's Institute of Technology Ladkrabang, Bangkok, 2020
Bachelor's degree in Material Engineering,
Kasetsart University, Bangkok, 2017

Major: Automotive Engineering

Presentations and Publications:

- [1] T. Nithimethakul, P. Karin, N. Ohtake, P. Wila, T. Yodkaew, B. Vetayanugul, M. Morakotjinda and R. Tongstri, "Effect of molybdenum on the microstructure and mechanical behavior of the sintered Fe-Mo-Mn-Si-C composite", 2020, The 11th International Conference on Mechanical Engineering (ICoME 2020), 1-4 DECEMBER, Ubon Ratchathani, Thailand.